

<b>REPORT DOCUMENTATION PAGE</b>				Form Approved OMB No. 0704-0188	
Public reporting burden for this collection of information is estimated to average 1 hour per response, including the time for reviewing instructions, searching existing data sources, gathering and maintaining the data needed, and completing and reviewing the collection of information. Send comments regarding this burden estimate or any other aspect of this collection of information, including suggestions for reducing the burden, to Department of Defense, Washington Headquarters Services, Directorate for Information Operations and Reports (0704-0188), 1215 Jefferson Davis Highway, Suite 1204, Arlington, VA 22202-4302. Respondents should be aware that notwithstanding any other provision of law, no person shall be subject to any penalty for failing to comply with a collection of information if it does not display a currently valid OMB control number. <b>PLEASE DO NOT RETURN YOUR FORM TO THE ABOVE ADDRESS.</b>					
<b>1. REPORT DATE (DD-MM-YYYY)</b> 01-12-2005		<b>2. REPORT TYPE</b> Final Report		<b>3. DATES COVERED (From – To)</b> 15-May-01 - 22-Mar-06	
<b>4. TITLE AND SUBTITLE</b>  Supersonic Flow Control by Magnetic Field			<b>5a. CONTRACT NUMBER</b> ISTC Registration No: 2009p		
			<b>5b. GRANT NUMBER</b>		
			<b>5c. PROGRAM ELEMENT NUMBER</b>		
<b>6. AUTHOR(S)</b>  Dr. Sergei Bobashev			<b>5d. PROJECT NUMBER</b>		
			<b>5d. TASK NUMBER</b>		
			<b>5e. WORK UNIT NUMBER</b>		
<b>7. PERFORMING ORGANIZATION NAME(S) AND ADDRESS(ES)</b> Ioffe Physico-Technical Institute of Russian Academy of Sciences 26, Polytekhnicheskaya St. Petersburg 194021 Russia				<b>8. PERFORMING ORGANIZATION REPORT NUMBER</b>  N/A	
<b>9. SPONSORING/MONITORING AGENCY NAME(S) AND ADDRESS(ES)</b>  EOARD PSC 821 BOX 14 FPO 09421-0014				<b>10. SPONSOR/MONITOR'S ACRONYM(S)</b>	
				<b>11. SPONSOR/MONITOR'S REPORT NUMBER(S)</b> ISTC 00-7050	
<b>12. DISTRIBUTION/AVAILABILITY STATEMENT</b>  Approved for public release; distribution is unlimited.					
<b>13. SUPPLEMENTARY NOTES</b>					
<b>14. ABSTRACT</b>  This report results from a contract tasking Ioffe Physico-Technical Institute of Russian Academy of Sciences as follows: The project proposes thorough experimental and theoretical investigations of the effects of magnetic and electric fields on performance of magnetohydrodynamic (MHD) control over supersonic flows in supersonic intakes. Experimental and numerical investigations focus on the basic aspects of MHD interaction taking into account the specific characters of gas ionisation, thermodynamic and electrophysical properties of weakly-ionised plasma, molecular and turbulent transport, shock-waves dynamics, boundary layers on the intake walls, massive flow separation within the scram-jet flow pass. Recent results of experimental and theoretical investigations carried out by the laboratories involved revealed important aspects of MHD supersonic flow control. It was found that a global change of intake flow structure might be achieved with local ( in time and space ) MHD impact. Other aspect is supposed to be important is investigation of essentially unsteady processes induced by pulse-periodic MHD impact on flow structure in intake models. The MHD flows under study were found to be conducive to separation due to the MHD interaction which is supposed to be investigated as well. Thus in the course of the project new aspects of MHD interaction will be systematically studied: shock-wave-boundary layer interaction, flow separation, local MHD impact and pulse-periodic regime of intake operation.					
<b>15. SUBJECT TERMS</b> EOARD, Physics, Fluid Mechanics					
<b>16. SECURITY CLASSIFICATION OF:</b>			<b>17. LIMITATION OF ABSTRACT</b> UL	<b>18. NUMBER OF PAGES</b>	<b>19a. NAME OF RESPONSIBLE PERSON</b> SURYA SURAMPUDI
<b>a. REPORT</b> UNCLAS	<b>b. ABSTRACT</b> UNCLAS	<b>c. THIS PAGE</b> UNCLAS			<b>19b. TELEPHONE NUMBER</b> (Include area code) +44 (0)20 7514 4299

**ISTC PROJECT No.2009p**

# **SUPERSONIC FLOW CONTROL BY MAGNETIC FIELD**

## **Annual Technical Report #4**

**Project Manager**

Professor S.V.Bobashev

**September 2005  
Saint-Petersburg, Russia**

## NOMENCLATURE

$M$	is the Mach number of the flow
$S$	is the electrodes and gap's area
$h$	is a height of the interelectrode gap
$k$	is a load coefficient
$u$	is a flow velocity
$B$	is magnetic field induction
$\sigma$	is plasma conductivity
$\beta_e$	is the Hall parameter for the electrons
$\nu_i$	is ionization frequency
$I_{ind}$	is a induced current
$V$	is electrode voltage
$E$	is the electric field strenght
$\varphi$	is the electric field potential. the electric current
$n$	is the number density of the heavy particles (ions and atoms);
$n_e$	is the electron number density
$\alpha$	is the ionization degree
$T, T_e$	are the temperatures of heavy particles and electrons
$U$	is the the plasma velocity
$q_w$	is the body wall heat flux due to heavy particles
$(q_w)_e$	is the body wall heat flux due to electrons

1. MHD Interaction in air plasma .....	3
Introduction .....	3
1.1. Discharge in immobile gas .....	3
1.1.1 Formulation of the problem .....	3
1.1.2. Pin electrodes and test chamber. ....	4
1.1.3. Electrical schemes.....	4
1.1.4. Measurements results.....	5
1.2. MHD interaction in gas discharge air plasma.....	6
1.2.1. Organization of the experiment. ....	6
1.2.2. Flow parameters.....	7
1.2.3. Electrodes .....	8
1.2.4. Formation of ionizing pulses .....	9
1.2.5. Experiments in MHD channel .....	9
1.2.6. Conclusions.....	10
1.3. References .....	10
2. Experimental investigations of magnetic field–supersonic flow interaction at the Ioffe Institute Big Shock Tube (BST)	
.....	34
2.1 Introduction .....	34
2.2 Design of the model under study .....	35
2.3 Results of measurements .....	36
2.4 Conclusions .....	38
2.5References .....	39
3. NUMERICAL SIMULATION.....	46
3.1. Introduction .....	46
3.2. Mathematical model .....	46
Plasma equations. ....	47
Electric field potential equation. ....	49
Boundary conditions .....	49
3.3. Numerical method .....	50
Method for the solving electric field potential equation. ....	50
Method for the solving plasma dynamic equation. ....	51
3.4. The results of calculations. ....	51
3.5. Analysis of factors influencing on supersonic flow about “cone-cylinder” body under MHD impact.....	62
3.6. Spatial structure of flow about body accounting for rotation of electric discharge on the body front surface. ....	65
3.7 Conclusions .....	71
3.8 References .....	71

# 1. MHD Interaction in air plasma

## Introduction

Till now, the experimental study of the MHD-interaction in an diffuser has been made when using ionized Xe as a working body [1-4]. It resulted in a series of original and important data. Need in such modeling arises because of the shortcomings of the modern experimental methods in producing the air plasma having the parameters required for the MHD-experiments: in a rather large volume, plasma should be homogeneous in density and of higher ionization degree than in the ordinary gas discharge, i.e.,  $10^{-5} - 10^{-4}$ .

The purpose of this stage of our work is to produce the diffuse layers of a rather high conductivity and maintain the magneto-induced current in a supersonic MHD- channel using a sequence of impulse discharges at equal intervals.

A general obstacle in obtaining the uniform plasma volumes is the rise of the instabilities which result in transferring a glow discharge to the arc one. The various methods were advanced to suppress the instabilities which result in a significant increase in the lifetime of a uniform ignition of the discharge [5, 6].

For self-sustained discharges, an increase in the lifetime of the uniform discharge phase involves the electrode sectioning and incorporating a separate ballast resistance in each section or application of a plasma cathode provided with a creeping discharge. For the non-self-sustained discharges, the fundamental factor in obtaining the uniform ignition is to introduce a rather high concentration of the electrons into the gap from an external source.

In this work, both of these variants of discharge ignition in the ionizer, self-sustained and non-self-sustained discharges were used. It should be noted, that the requirements upon the degree of plasma uniformity in the investigations on plasma aerodynamics, as a rule, can be essentially less than those of laser technology.

This work consists from two stages. On the first stage [5, 6] investigations were made in immobile gas without magnetic field. In this stage the construction of pin electrode was developed, different types of discharges were tested, boundary conditions on pressure and voltage at which discharge are diffuse were found. On second stage [7, 8] pulse-periodic ionization of air flowing through lateral magnetic field were made and production of magneto-induced current were tested.

In experiment pulse-periodic process was modeled by sequence of ionizing signals supplying to three independent ionizers, placed on some distance one from other. We intend to use this very circumstance that the lifetime of ionized gas volume is essentially larger than that of a gas-discharge impulse. With impulse-periodical current, a layered flow arises with alternating conducting, more or less, layers which can be used as a working body in the MHD-channel.

We intend to use this very circumstance that the lifetime of ionized gas volume is essentially larger than that of a gas-discharge impulse. With impulse-periodical current, a layered flow arises with alternating conducting, more or less, layers which can be used as a working body in the MHD-channel.

## 1.1. Discharge in immobile gas

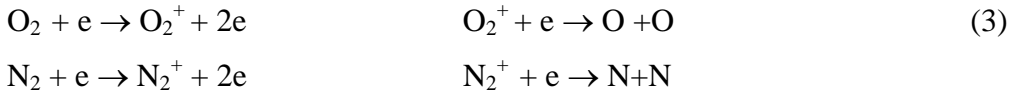
### 1.1.1 Formulation of the problem

The aims of test experiments were to achieve conditions at which discharge between electrodes uniform, to determine electron concentration and plasma conductivity, and to study plasma decay after switching-off of ionizing voltage with aim to determine characteristic time  $\tau_d$ , during which conductivity decrease up to value sufficient for MHD interaction.

To determine a of plasma decay for different types of discharges and for combined discharge with the aim of estimating possibility of a pulse-periodic ionization process.

A reliable estimation of the plasma parameters can be accomplished for an ideal situation of uniform plasma state in a uniform electric field at  $V < V_{br}$  where  $V_{br}$  is a breakdown voltage, when

using the Townsend calculation scheme [8]. Here, supposedly, ionization arises due to electron impact and ions recombine due to dissociative recombination



As the ionization and recombination rates for  $\text{O}_2$  and  $\text{N}_2$  are not too different from each other [9], then, the estimations are accomplished for the cumulative air particles.

The kinetic equation is as follows

$$\frac{dN_e}{dt} = \nu_i N_e - \beta N_e^2 \quad (4)$$

where  $\nu_i$  is ionization frequency to be determine via the Townsend ionization coefficients [9] and  $\beta$  are the dissociative recombination coefficients taken from [10].

$$\beta = 3 \cdot 10^{-3} T_e^{-3/2} \text{ cm}^3/\text{s} \quad (5)$$

Concerning the electron sticking with the  $\text{O}_2$  molecules, note that this process is of no importance in the pulsed discharges because of the small rate of this process of which values are given in [11].

An example for the conditions including  $E/p = 30 \text{ V}/(\text{cm} \cdot \text{Torr})$  and  $p=10 \text{ Torr}$  gives  $T_e = 18000\text{K}$ ,  $\nu_i = 5 \times 10^{-4} \text{ s}^{-1}$ ,  $\beta = 1.25 \times 10^{-9} \text{ cm}^3/\text{s}$ ; steady state electron density  $N_{\text{ect}} = 4 \times 10^{13} \text{ cm}^{-3}$  is obtain in a time of an order of  $2 \times 10^{-5} \text{ s}$ . Inherent recombination time  $t_r = 2 \cdot 10^{-5} \text{ s}$  and  $\sigma = 25 \text{ Sm/m}$ , pulse transfer frequency is,  $\nu_e = 3.9 \times 10^{10} \text{ s}^{-1}$ .

In this study, the general plasma parameters are determined via the experimental data.

#### 1.1.2. Pin electrodes and test chamber.

To ignite a diffuse discharge, in agreement with the recommendations in [9], the pin electrodes were involved. A pin electrode 0.5 mm wide and 1.5 mm in length is fabricated from silver-plated brass. Six electrodes inserted into an isolation plate make up a single section. Placement of the electrodes on this section is shown in Fig. 1.1.1. The electrode inserts are mounted in a test vacuum chamber representing a shock tube section fabricated from plexiglass of 50x50 mm cross-section. The electrodes project beyond the surface of the insert by 2 mm. In Fig. 1.1.2, a picture of the test section with the inserted electrodes is given. One can see that both the anode and cathode incorporate the pin electrodes. The chamber's design enables the various pressures of a working gas to be maintained.

#### 1.1.3. Electrical schemes

An electric schematic of the ionizer operation is shown in Fig. 1.1.3a. Primary winding of a transformer  $\text{Tr}_1$  is included in the anode circuit of a pulse thyatron. After thyatron start-up, a capacitor  $C_3$  circuiting a secondary winding is charged up to the breakdown voltage of a discharger-sharpener P. After breakdown of this discharger, the high-frequency oscillations arise in a contour  $C_3 L_3$  which are transferred via a transformer  $\text{Tr}_2$  on the electrodes of the ionizer. Their frequency not considering a mutual winding inductance is determined, in the first approximation, by the parameters of a capacitor  $C_3$  and inductance  $L_3$  as  $\omega = (L_3 C_3)^{-1/2}$  (at  $L_3 \ll L_2$ ).

Amplitude of the high-frequency oscillations in a contour depends on (1) magnitude of a high-voltage pulse coming from the thyatron scheme to the primary winding of  $\text{Tr}_1$ , (2) adjusting the ignition voltage of a discharger-sharpener P, (3) parameters of a transformer  $\text{Tr}_2$ . This amplitude can be varied within the wide limits depending on the experimental conditions. Duration of a high-frequency oscillation train is determined by both the pulse duration of the primary circuit  $\text{Tr}_1$  and Q-factor of a contour  $L_3 C_3$ , P.

As the thyatron, it is involved a pulsed hydrogen thyatron TGI-325/16 of home fabrication working at anode voltage up to 16 kV. Delay of the thyatron start-up of such a type relative to arrival time of a synchronous pulse is not greater than 0.5 mks. Amplitude of this synchronous pulse is about 100 V. To suppress interference from induced currents in cable sheath, this synchronous pulse feeds the thyatron grid via an isolating transformer (1:2) wounded on a ferrite ring (primary winding of 20 turns, the secondary one of 40 turns).

Fig.1.1.4 shows scheme of organization of combined discharge, which includes switching-on high-frequency and high-voltage discharges. The scheme of organization of high-voltage discharge similar to presented above (see fig.1.1.3).

Larger amount of energy for gas ionization in the ionizer sections comes from a pulse discharge of a capacitor  $C_1$  with time delay (relative to HF-pulse) control. A capacitor  $C_1$  is connected to the pin-electrodes via ballast resistances  $R_b$ . HF-pulse supplies the same electrodes via blocking capacitors  $C_s$  which accomplish two actions. First, they are the ballast impedances for HF-pulse; second, they separate a secondary winding  $Tr_2$  from a high voltage charging the capacitor  $C_1$ . Thyatron scheme for discharging  $C_1$  is similar to that for HF-pulse generation.

Fig.1.1.5 shows scheme of two-pulse high-voltage discharge.. It makes possible to supply the pin-electrodes with two high-voltage pulses with controlled time interval between them, which is maintained by a synchronization unit. To generate both pulses the identical thyatron schemes are applied, similar the above ones (see, Fig. 1.1.3a). Each pulse is supplied to the pin-electrodes via own group of the ballast resistances. Supply of three high-voltage pulses in a row is realized in the same manner.

#### 1.1.4. Measurements results

Discharge diagnosis was as follows. In the experiment, voltage  $V(t)$  on capacitor  $C_1$  was measured with the help of a potential divider. The current value can be determined by differentiation of this signal

$$I = C_1 \frac{dV}{dt} \quad (4)$$

The total resistance 
$$R = \frac{V}{I}, \quad (5)$$

$$R = R_{eff} + R_b \quad (6)$$

Where  $R_{eff}$  is effective resistance of the plasma gap and  $R_b$  is ballast resistance, determined as equivalent resistance of individual resistances connected in parallel. Voltage on the plasma gap

$$V_p = V \frac{R_{eff}}{R} \quad (7)$$

The average effective conductivity  $\langle \sigma_{eff} \rangle$  was determined as

$$\langle \sigma_{eff} \rangle = \frac{L}{R_{eff} S}, \quad (8)$$

where  $L = 5$  cm is the distance between electrodes,  $S = 2$  cm<sup>2</sup> is the discharge cross-section. The average electron concentration was determined as

$$\langle N_e \rangle = \frac{\langle j \rangle}{e v_d}, \quad (9)$$

where  $\langle j \rangle = \frac{I}{S}$  is the average current density,  $e$  is the electron charge,  $v_d$  is the electron drift velocity

determined from [8] using the values of  $E/p$ , where  $E = \frac{V_p}{L}$  is the electric field intensity.

All presented experimental results obtained at pressure  $p=15$  Torr. Preliminary investigations [5, 6] show that at pressure  $p \leq 15$  Torr the discharge are uniform. Figs.1.1.6, 1.1.7 and 1.1.8 shows photographs of luminosity in interelectrode gap at high-frequency, combined and high-voltage discharges, respectively. It is seen that luminosity in gas volume are relatively uniform, and there is an increase in luminosity in regions near electrodes. Ballast resistance connected to the anode, which is upper electrode in figure

For diagnosis of the HF discharge, it was affected by a relatively long discharge of capacitor  $C_1$  at relatively low voltages  $V \ll V_{br.}$ . Fig. 1.1.9 shows variations in voltage on the capacitor (a), and current value (b). The oscillogram of voltage demonstrates a HF discharge (with frequency of the order of 10 MHz and duration of about 2 mks). It can be seen that a fall of diagnostic voltage occurs after its completion.

Fig. 1.1.10a shows a decrease in electron concentration with time. At  $t=0$ ,  $\langle N_e \rangle = 5.6 \cdot 10^{18} \text{ m}^{-3}$ , at  $t = \tau_d$   $\langle N_e \rangle = 1.5 \cdot 10^{18} \text{ m}^{-3}$ .

Fig. 1.1.10b shows variation in values of the average effective conductivity with time obtained at different voltages on capacitor  $C_1$ . The fact that that all the curves  $\langle \sigma_{eff} \rangle(t)$  are close to each other indicates that the discharge of capacitor  $C_1$  serves only for diagnosis and at  $V \leq 2500 \text{ V}$  does not introduce extra ionization into the interelectrode gap.

Combined discharge are obtained by applying a high-voltage pulsed discharge with the voltage on capacitor  $C_1$  close to the breakdown voltage on HF discharge. Fig. 1.1.11a shows variations of voltage and of current with time. Fig. 1.1.11b shows the values of  $E/p$  and electron drift velocity  $v_d$ , for the different moments of time. Fig. 1.1.11c presents time dependence of the average effective conductivity and average electron concentration. In this case we can see extended plasma decay, which can be explained by the fact that there is a higher voltage on the electrodes, and simultaneously with plasma recombination there is a plasma ionization. In this case the conductivity change ??? than in the case of recombination for the time  $\tau_d$  (see Fig.1.1.10b). Fig.1.1.12 shows changes in current and electron concentration with time. Results shows that using such scheme allow us to make several ionizing pulses with time delay between them.

The results of experiments are given in Table 1.

$t$  is time of discharge,  $W$  is energy of discharge.

Table 1

Type of discharge	$\langle j \rangle$ , $\text{A/m}^2$	$\langle \sigma \rangle$ , $\text{Sm/m}$	$N_e$ , $\text{m}^{-3}$	$t$ , $\mu\text{s}$	$W = J^2 t / \sigma$ $\text{J/m}^3$
High-frequency	$10^4$	2	$0.2 \cdot 10^{19}$	2	25
Combined	$9 \cdot 10^4$	12	$3.5 \cdot 10^{19}$	2	$0.88 \cdot 10^3$
High-voltage	$2.5 \cdot 10^4$	4	$1.0 \cdot 10^{19}$	2	$3.1 \cdot 10^2$

## 1.2. MHD interaction in gas discharge air plasma.

### 1.2.1. Organization of the experiment.

A schematic of the setup is presented in Fig. 1.1.13. A supersonic airflow is arisen in the diaphragm shock tube with reflecting nozzle used earlier [12-15]. The gas-dynamic range includes the



shock tube and divergent nozzle, being a working chamber. A narrow slit separated from the nozzle with a thin diaphragm is displaced at the shock-tube end cup. The diaphragm being disrupted, a gas heated behind the reflected shock wave enters the nozzle and is accelerated into the divergent channel. Shock-tube diameter is 50 mm, low-pressure chamber length is 450 cm, high-pressure chamber length is 100 cm, linearly divergent nozzle width PHS 46 mm, opening half-angle of the nozzle is  $11^\circ$ , and nozzle's height in critical cross-section is 5.5 mm.

To obtain the volume ionization of air (nitrogen), three pairs of the ionizing pin-electrodes are located on the vertical sides of the working chamber as shown in Fig. 1.1.13. They are supplied with the equally spaced signals from the special system of the ionizing pulses. The system start-up is synchronized with the gas-dynamic processes via a piezoprobe situated in the gas tube. There are the sectioned electrodes for short-circuiting the magneto-induced current on the horizontal sides. The electrodes are mounted on a special removable insert.

Here, in Fig. 1.1.13, the directions of the main velocity vectors are shown: flow velocity ( $u$ ), magnetic induction ( $B$ ), magneto-induced ( $j_y$ ) and discharge ( $I_d$ ) currents.

A schematic of the pin-electrode connections via the separate ballast resistances  $R_b$  and a schematic of short-circuiting the magneto-induced current via a load resistance  $R_L$  are shown as view in section A-A.

Figure 1.1.14 shows the setup picture. One can see the low-pressure chamber of the shock tube, attachment flange with the working chamber, pair of textolite plates in which the Helmholtz coils are mounted; there is the working chamber between these plates, further, there is a shock absorber. This Figure shows also the working section close-up.

A scheme to produce the transverse quasi-stationary magnetic field up to 1.5 T is described in [1-4].

As shown in Table 1, the highest ionization is obtained at the combined discharge, however, this mode consumes the relatively large amounts of energy. So, the combined discharge is needed for the first pulse as the previous studies [5, 6] have shown that the uniform initial ionization is resulted. The following pulses occur in an ionized gas. The impulse high-voltage discharge can be only used for the pulses, which follow the first one as the gas is already ionized. In the initial experiments of which results are presented in this Report, only the high-voltage discharges are used at all the pulses.

Recombination rate in still air when the discharge is over has been determined in [6]. The overall data concerning the temporal decrease in plasma conductivity are shown in Fig. 1.1.15. Note, these results are obtained at the temperature of electrons  $T_e = 15000-12000K$  as the diagnostic quasi-stationary electric field supplied during the afterglow is  $E/p = 10^{-5} V/(cm \cdot Torr)$ .

Show a conditional distribution of conductivity along the channel when all three ionizers are supplied with three short ionizing pulses of  $\approx 1$  mks in duration with a given interval. They produce the regions of uniform ionization. Suppose, for simplicity, that these regions have the sharp boundaries coinciding with the boundaries of these ionizers, and they are not blurred in time. Conductivity of such regions when moving along the channel is decreased in time due to recombination. At the conditions nearest to the experiment, Fig. 1.1.16 shows a change in conductivity along the channel for different times. This Figure shows that arising the quasi-stationary flow of conductivity with the weak temporal changes is terminated by the time of the second pulse at such connection mode of the ionizers. Under other connection mode, the layered flows can arise. The preliminary experiments [5, 6] show that, in this case, a mean conductivity is about 2-4 Sm/m.

## 1.2.2. Flow parameters

The initial parameters of the low-pressure chamber of the shock tube are denoted by "1", those behind the shock wave – "2", those behind the reflected shock wave – "5", high-pressure chamber parameters – "4".

Figure 1.1.17 shows a x-t diagram to determine duration of a plug of shock-compressed gas downward the reflected shock wave at  $M_2=3.001$ ,  $\frac{p_4}{p_1}=650$ . A value of  $\frac{p_4}{p_1}$  should be increased

about 1.5 times during the experiment for obtaining the same Mach number of an incident shock wave. The experimental values of a working time turn out to be 2 times less than the calculated ones [16], thus, real outflow time is about 750 mks for our setup.

Figure 1.1.18 shows the relative values of decelerating temperatures and density downward the reflected shock wave  $M_5$  at the different Mach numbers of the incident shock wave  $M_2$ , as well as the ratios of air pressures onto the diaphragm with which is generated a flow of given  $M_2$ , all these values being calculated via the ideal shock-wave theory [16].

Figure 1.1.19 shows the relative values of the flow parameters in the linearly divergent channel calculated via the isentropic formula [17].

A working regime of the shock tube is selected from the following reasons: a hot plug length should be many times greater than length of a region of the MHD interaction, particle concentration in a working section  $N = 10^{23} \div 10^{24} \text{ m}^{-3}$ , under expansion in the nozzle, a gas temperature should be higher than that of condensation of the air components and virtual molecular admixtures, a temperature of air heated behind the reflected shock wave should not be higher than a temperature at which a relevant change in the air molecular composition proceeds. The experiment is carried out at working conditions of the shock tube as follows: Mach number of airflow in the shock tube  $M_2 = 3$ ,  $p_I = 34 \text{ torr}$ ,  $T_I = 300 \text{ K}$ .

When entering an interaction region  $X_{in} = 16.5 \text{ cm}$ , the flow Mach number  $M = 3.6$ ,  $T = 395 \text{ K}$ ,  $u = 1.41 \cdot 10^3 \text{ m/s}$ ,  $N = 5.34 \cdot 10^{23} \text{ m}^{-3}$ . A pressure reduced to the conditions of a gas discharge  $p_{dis}$  is determined as the pressure at a temperature 300K at the same particle concentration  $N$ . At the entrance into the interaction region  $p_{dis} = 15 \text{ Torr}$ . Working time for experimenting in the MHD interaction region is 500 mks. It is limited by an arrival of a flow reflected from the end cup of the working chamber in the interaction region. Kinetic energy of a flow entering the interaction region is

$$\frac{\rho u^2}{2} = 2.47 \cdot 10^4 \text{ J/m}^3. \text{ A parameter of MHD interaction } St = \frac{\sigma B^2 L}{\rho u} \text{ at a length of interaction region } L$$

$= 0.1 \text{ m}$ ,  $\sigma = 4 \text{ Sm/m}$ ,  $B = 1.5 \text{ T}$  and given gas-dynamic parameters has a value  $St = 0.024$ . According to [1, 4, and 18], at this value of  $St$ , the magnetic field can influence strongly the flow parameters. The

$$\text{Hall parameter } \beta = \beta_e = \frac{\omega_e}{\nu_e} = 4.5.$$

### 1.2.3. Electrodes

In this study, the pin-electrodes are fabricated differently as it is shown in Fig. 1.1.20. Here, an electrode of the first ionizer is shown. It consists from 70 pins introduced into a flow by 6 mm being unified in the sections of 10 each.

A resistance of interelectrode gap of a separate section is denoted by  $R_i$  with a connection to a ballast resistance  $R_{bi}$ . Essentially, these sections are the separated pins and their collection is a pin-electrode. An equivalent resistance including 7 sections and 7 ballast resistances, all the  $R_i$  being supposedly equal, can be presented as  $R_{eq} = R_{eq} = \frac{R_i + R_{bi}}{7}$ . Essentially,  $R_{eq}$  is a conventional notation of the ionizer.

An electrode for removal of the magneto-induced current is fabricated from a bulk of brass with several salients of 4 mm height. This is because of arising the near-electrode drop of a potential as high as 60 V being comparable with the magneto-induced EMF due to different near-electrode and near-wall effects as it is shown by the experiments [1-4] carried out with the smooth electrodes. So, for current circuiting, an additional external electric field is required. We decide that an application of the electrodes with sharp sides and extended beyond a boundary layer can decrease the near-electrode drop in a potential. Such electrodes are used as a cathode as an anode.

Control experiments we carried out with Xe. As it is known [1-4], a relevant recombination time of thermally ionized Xe in a shock tube when expanding into a nozzle is of several orders of magnitude higher than for air. A regime to be accomplished is such that conductivity at a working section is of order of 10 Sm/m as estimated. The experimental results show that, at an external voltage

of 30 V, electrode current turns out to be  $1 \div 2$  A as expected. Thus, a near-electrode drop is at least 2 times lower when using such electrodes and makes possible to record the magneto-induced current.

Location of the electrodes in MHD channel is pictured in Fig. 1.1.21. This shot is made when a forward insert with the ionizing electrodes-anodes is removed. The picture shows the divergent channel, the electrodes for current removal and ionizing electrodes-cathodes.

An electric field of the ionizing electrodes is directed along the magnetic strength lines to remove any effects on a discharge current of the magnetic field as we have not studied such effect till now. Further, the MHD electrodes to decrease an influence of a Hall current should be narrower with smaller spacings between each other and their displacement should be below the ionizing electrodes as well as between them. However, we locate the current-removing electrodes only between the ionizing electrodes being afraid of short-circuiting uncontrollably a gas-discharge and magneto-induced currents because of our primary attempt to accomplish a simultaneous work of both systems.

#### 1.2.4. Formation of ionizing pulses

For air ionization in a supersonic flow with a shock tube, two modes are used: first, a combined discharge, which uses the gains of a high-frequency (HF) high-voltage breakdown for preliminary gas ionization in an interelectrode gap of an ionization section (fig.1.1.4). Greater amount of energy is produced by a discharge of additional capacitance, which follows the high-frequency pulse with a controlled time delay. Second, a pulse-periodic discharge (fig.1.1.5) when a system of electrodes is supplied with the high-voltage pulses of several separate sources. Time between the pulses can be variable within wide limits.

It is the anode to be used experimentally as a pin-electrode with separate ballast resistances, but [9] recommends the cathode. However, in our experiment, uncontrollable arcing ground occurs in certain runs.

In Fig. 1.1.22, a flow-chart of ionizer connection with a voltage source is shown. All the ionizers are included in a single unit. A voltage comes from three high-voltage sources with controlled time intervals to this unit using a scheme of signal formation. In the experiment, as it is shown in Fig. 1.1.22, a voltage  $V$  is recorded on an equivalent resistance. In Fig. 1.1.23, a voltage oscillogram is shown of three pulses in a row in still air with 8 mks interval. In the experiment, the interval between pulses is varied. One can see that after a start-up, there is a time lag before the discharge beginning. Discharge duration is determined by a time of voltage decay on the ionizers, it is denoted as  $\Delta t$  in Fig. 1.1.23 and equals 1-3 mks, as a rule. Regretfully, we can not measure a current due to strong interferences influencing the Rogofsky coil.

Duration of light pulses is recorded with a PEMT directed at an angle to a region between 111 pair of ionizers. Figure 1.1.24 gives the emission oscillograms in a still gas from three discharges ignited with a shift from each other. One can see that afterglow duration is essentially greater than that of a current pulse.

It is difficult to record a discharge structure with such displacement of the ionizer. In Fig. 1.1.25, a side view of discharge picture is shown in a region of the 111 ionizer. The cathode is at the right and the anode is at the left. One can see that a glow in a volume between the electrodes is fairly uniform. Note a bright glow in a region of 9 anode pins. Distinct from the test experiment (Fig. 1.1.8), a glow in the cathode region is fairly uniform evidencing on a better disposition of the electrodes of ionizers.

#### 1.2.5. Experiments in MHD channel

A magneto-induced current  $I$  is measured experimentally, an electrode voltage  $V_{el}$ , resistance  $R_{el}$ , and a mean conductivity of interelectrode gap  $\langle \sigma \rangle$  are determined.

An equivalent flow-chart for each separate pair is shown in Fig. 1.1.26. It implies that the magneto-induced EMF  $\varepsilon$  falls on the inner resistance of the interelectrode gap and a load resistance  $R_L$

$$\begin{aligned}
\varepsilon &= IR_{el} + IR_L \\
I &= \frac{V_L}{R_L} \\
R_{el} &= \frac{\varepsilon - V_L}{I} \\
\langle \sigma \rangle &= \frac{h}{R_{el} S}
\end{aligned} \tag{6}$$

The experiment is performed at the conditions:  $B=1.3$  T. Calculated EMF of 1<sup>st</sup>, 2<sup>nd</sup>, and 3<sup>rd</sup> pair of electrodes equal 120 V, 140 V and 180 V, respectively. The voltages of the ionizing electrodes are 8 kV (I ionizer), 7 kV (II and III ionizers). Ionizing pulses comes with 10 mks interval.

Measurements of EMF was made at  $R_L \gg R_{el}$ ,  $R_L=1$  Ohm. Fig.1.1.27 shows oscillogram of voltage on the 2nd pair of electrodes. It is seen that voltage decrease with time, and maximum value 1.5 times lower than calculated EMF. This fact is due to there are a large role of leakage current and large interelectrode resistance due to large near-electrode voltage drop at low current. We will use calculated values of EMF, i.e. the role of factors noted above decrease with increasing current.

Typical oscillograms of magneto-induced current at  $R_L = 10$  Ohm are shown in fig 1.1.28. The highest current is recorded on the first pair of electrodes  $I=0.1$  A. Via the formulas (6)  $R_{el}=1.19$  kOhm,  $\langle \sigma \rangle = 0.07$  Sm/m. It can be seen that the obtained value of a mean conductivity is approximately 50 time lower that expected. Firstly, the Hall effect resulted in a voltage drop because of non-ideality of the electrode sectioning. At given geometry of the electrode system and taken value of Hall parameter ( $\beta_e = 4.5$ ), a mean conductivity should be  $\sim 5$  times lower, according to [18]. The edge effects result also in a decrease in a mean conductivity, being of importance in this case of a short channel when its length is comparable-sized with its height. Also, it of importance a near-electrode voltage drop resulting in several times conductivity decrease [18]. Thus, obtained value of a mean conductivity is in reliable limits. Its smallness is related with the fact that, when fabricating the channel, not all known requirements to the channel construction are fulfilled as the general task is to demonstrate a possibility to rise the magneto-induced current in air (nitrogen) discharge plasma.

It should be noted, that carrying out this experiment is proved to be very complicated due to mutually influence of ionizers work and MHD effects. We have managed to make a run of effective experiments. But it is need further searches for successful solutions of separate problems for reliable mutual work of ionizers and current collector electrodes.

### 1.2.6. Conclusions

A setup is created included the MHD system with a system of gas-discharge units.

The operation of gas discharge devices when ionizing pulse duration is less then recombination time in order was achieved. In this case delay between ionizing pulses and air plasma flight time between ionizes was set compared with recombination time.

Generation of the electric current is accomplished when air discharge plasma moves in the transverse magnetic field.

An experience and experimental backlog are maintained for a purpose to create a setup needed to control a supersonic airflow with MHD method.

### 1.3. References

1. S.V.Bobashev, A.V.Erofeev, T.A.Lapushkina, S.A.Poniaev, R.V.Vasil'eva, D.M. Van Wie, "Effect of MHD-Interaction in Various Parts of Diffuser on Inlet Shocks: Experiment", AIAA

- Paper 2002-5183, 11th AIAA/AAAF International Conference Space Planes and Hypersonic Systems and Technologies, 29 September - 4 October 2002, Orleans, France
2. S.V.Bobashev, A.V.Erofeev, T.A.Lapushkina, S.A.Poniaev, R.V.Vasil'eva, D.M.Van Wie. Non-Stationary Aspects Of Electric And Magnetic Fields Action On Shocks In Diffuser. - AIAA Paper 2002-2164, 33rd AIAA Plasmadynamics and Lasers Conference and 14th International Conference on MHD Power Generation and High Temperature Technologies Maui, Hawaii, USA, May 20-23, 2002. .
  3. S.V.Bobashev, A.V.Erofeev, T.A.Lapushkina, S.A.Poniaev, R.V.Vasil'eva, D.M. Van Wie, "Experiments On MHD Control Of Attached Shocks In Diffuser", AIAA Paper 2003-0169, 41st Aerospace Meeting and Exhibit. 6-9 January 2003, Reno, Nevada
  4. S.V. Bobashev, A.V. Erofeev, T.A. Lapushkina, S.A. Poniaev, R.V. Vasil'eva, D.M. Van Wie. Characteristics of the MHD Diffuser Under Different Commutations of Current. - AIAA Paper 2005-1334, 43rd AIAA Aerospace Sciences Meeting and Exhibit, Reno, Nevada, Jan.10-13, 2005
  5. Supersonic Flow Control by Magnetic Field, Technical Report No.15, ISTC project No.2009p, December 2004.
  6. Supersonic Flow Control by Magnetic Field, Technical Report No.16, ISTC project No.2009p, March 2005.
  7. Supersonic Flow Control by Magnetic Field, Technical Report No.17, ISTC project No.2009p, July 2005.
  8. Supersonic Flow Control by Magnetic Field, Technical Report No.18, ISTC project No.2009p, October 2005.
  9. Yu.P.Raizer "Physics of the gas discharge" Nauka, Moscow, 1987, p.592, (in Russian).
  10. Shao-Ch. Lin, J.Derek Teare, Phys. Fluids. V.6, N3, 1963, pp.355-375
  11. N.L.Alexandrov et al. Plasma Physics. V.17. N12, 1991, pp. 1446-1452, (in Russian).
  12. CRDF contrac "Investigation and perspectives of Gas Flow Control by Magnetic Field", Technical Report N1, 1999
  13. CRDF contract "Investigation and perspectives of Gas Flow Control by Magnetic Field", Technical Report N2, 1999
  14. CRDF contract "Investigation and perspectives of Gas Flow Control by Magnetic Field", Technical Report N3, 2000
  15. CRDF contract "Investigation and perspectives of Gas Flow Control by Magnetic Field", Technical Report N4 2000
  16. Shock tubes (ed. by Kh. A. Rahmattulin and S.S. Semenov), Izdatelstvo Inostrannoy Literatury, Moscow, 1962.
  17. L. G. Loitsyanskiy, Mechanics of Liquids and Gases, Begell House, New York, 1995. 984 pp.
  18. L.A.Vulis, A.L.Genkin, B.A.Fomenko. Theory and Calculation of Magnetogasdynamic Flows in the Channels (in Russian). Atomizdat, Moscow, 384 p., 1971

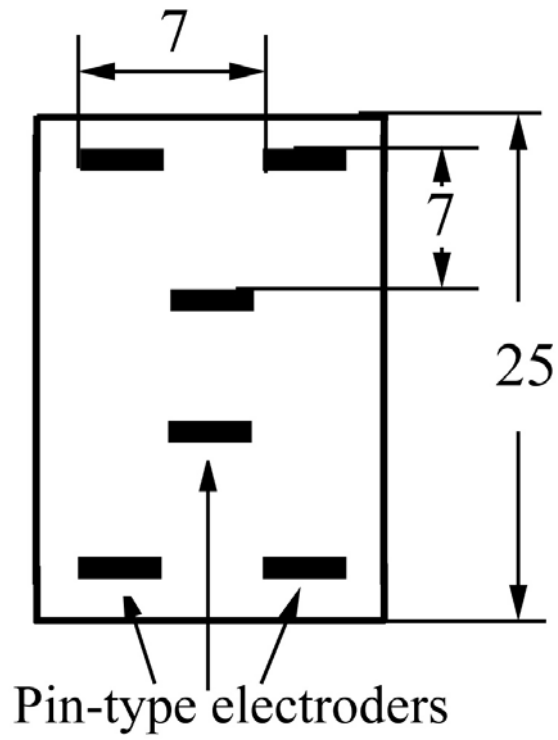


**Fig.1.1.1.** Placement of the pin electrodes on the electrode unit. Dimensions are in mm.

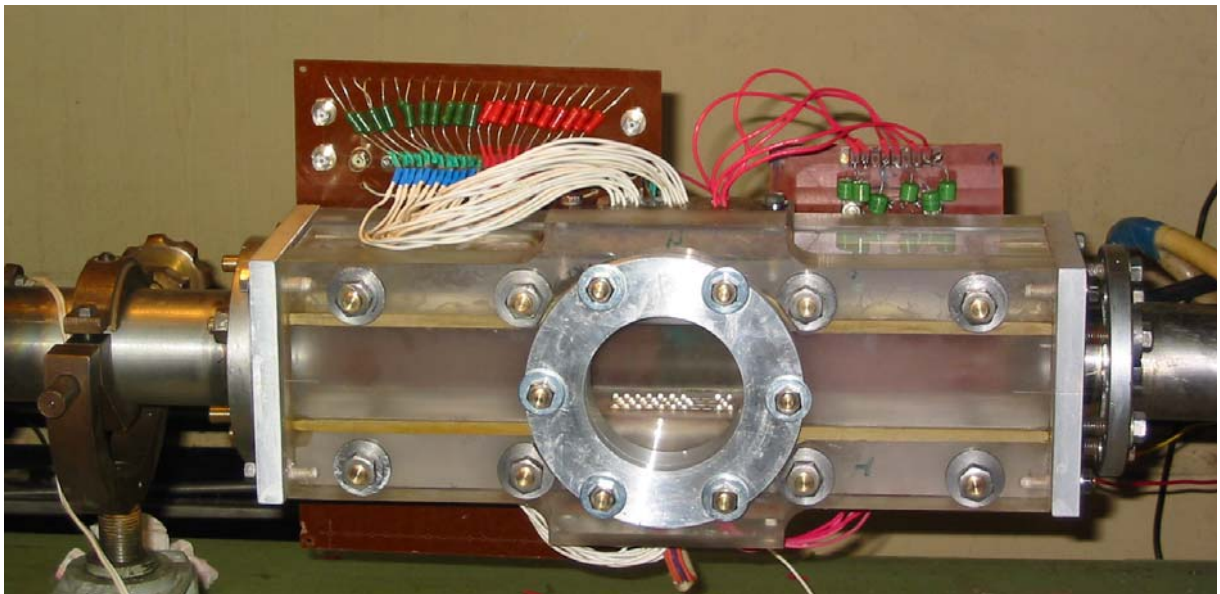


**Fig.1.1.2.** Picture of the test section.

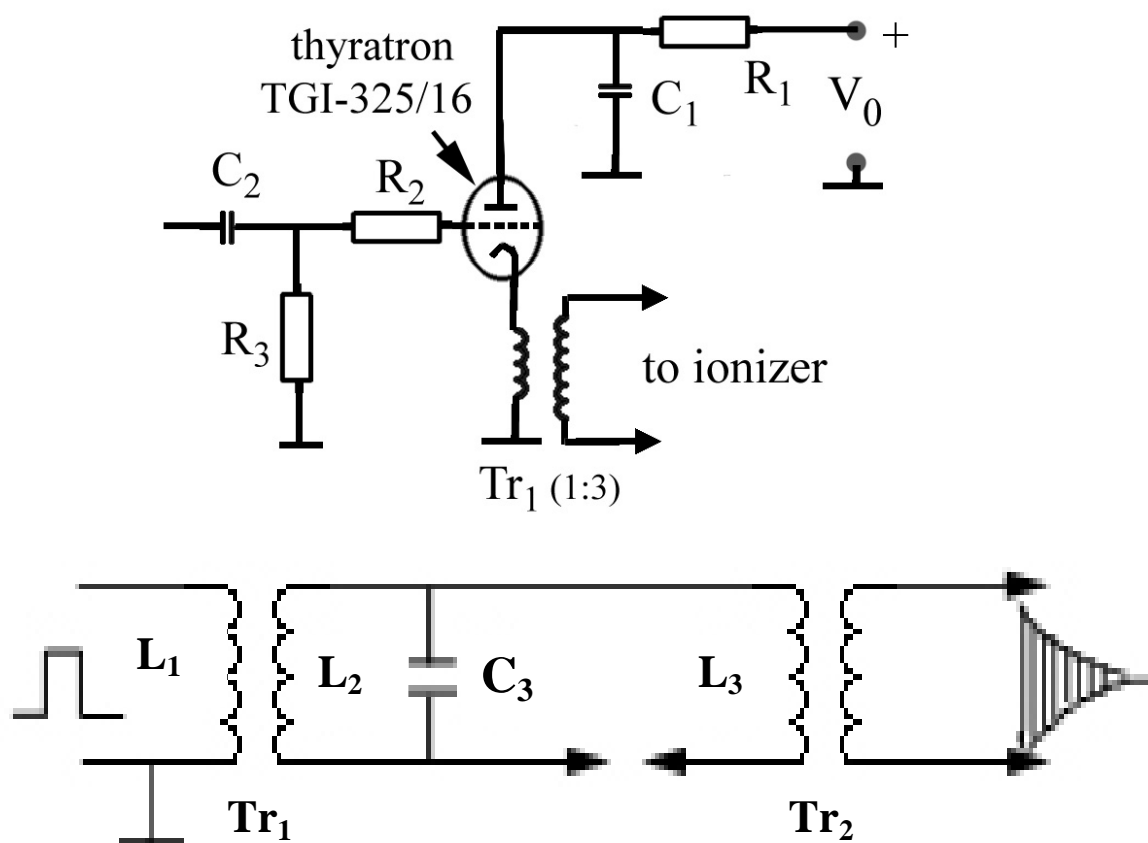


**Fig. 1.1.3.** a) Thyatron scheme for ionizer, b) Scheme to form a high-frequency pulse.

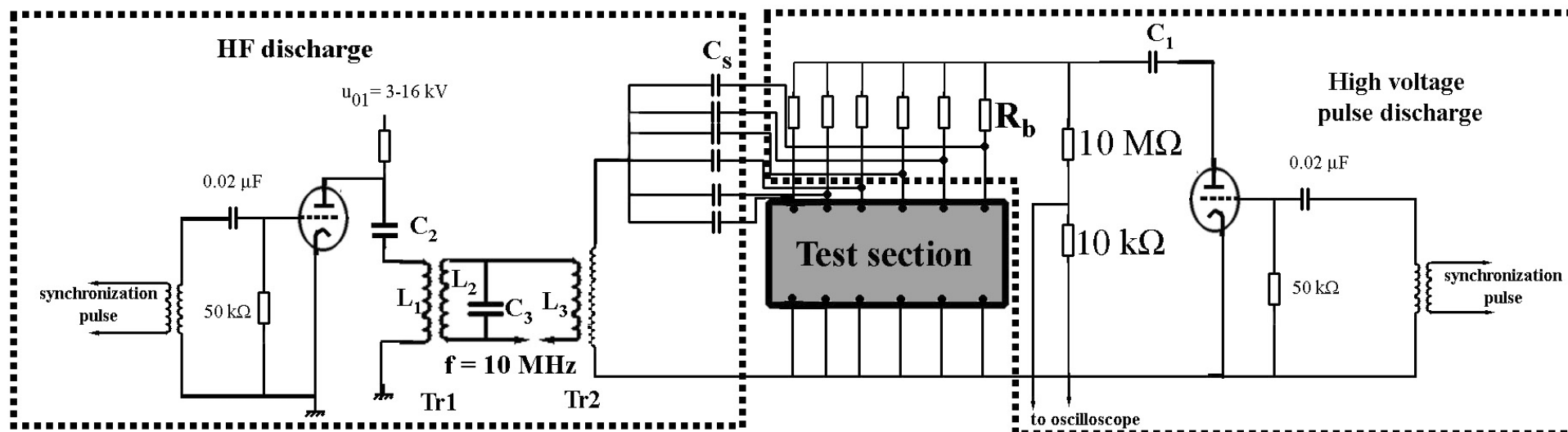


Fig.1.1.4. Electrical scheme of combined discharge formation.

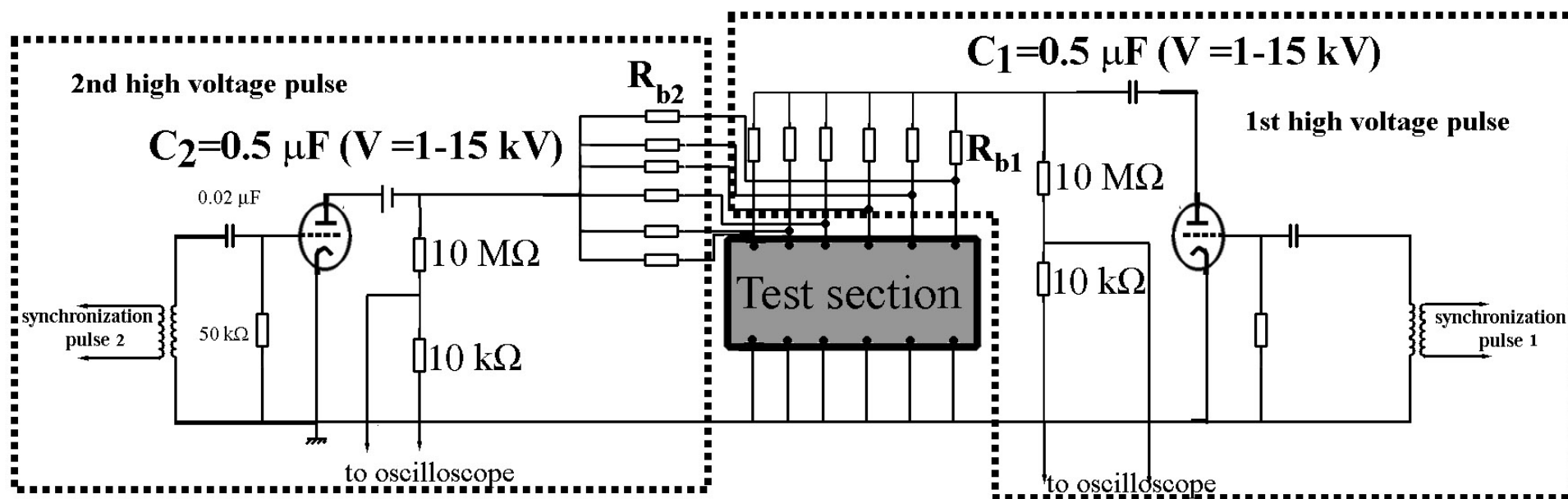


Fig.1.1.5. Electrical scheme of two high-voltage pulses formation





**Fig.1.1.6** Photograph of HF discharge



**Fig.1.1.7** Photograph of combined discharge



**Fig.1.1.8.** Photograph of luminosity in one-pulse high-voltage discharge

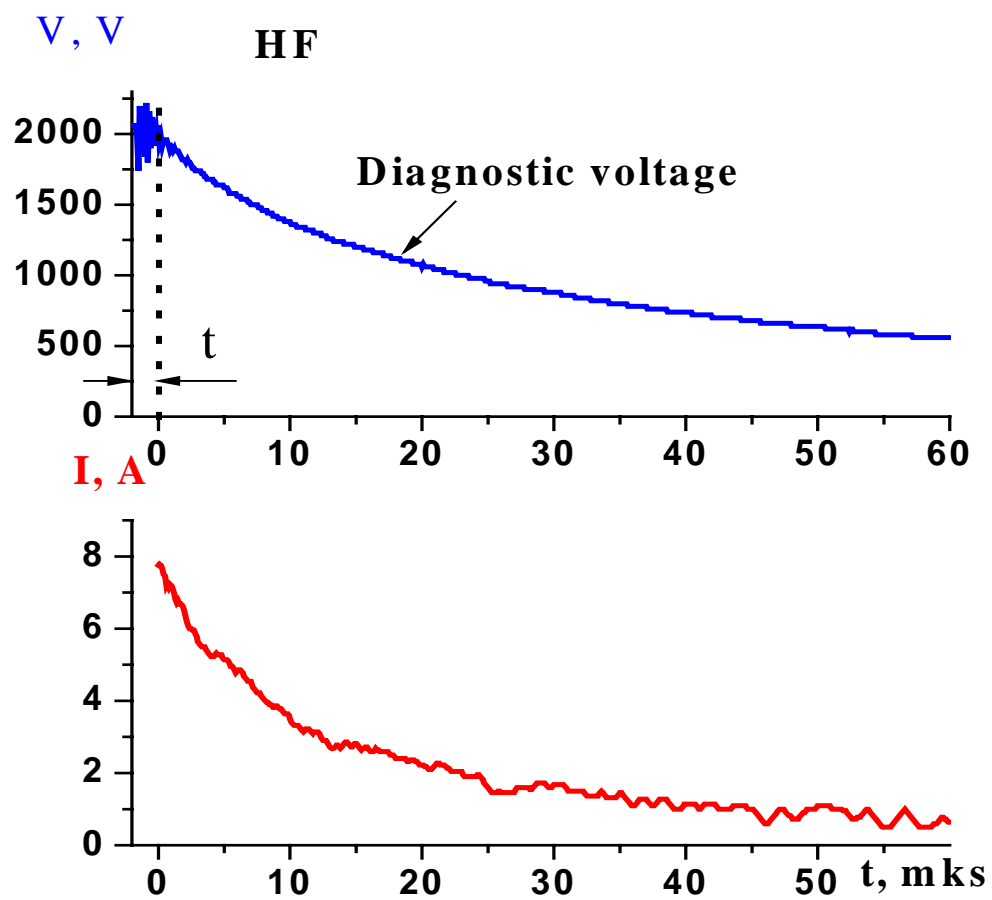


**Fig.1.1.9.** Diffuse HF discharge Change in voltage (a), current (b).  $t$  is time of discharge

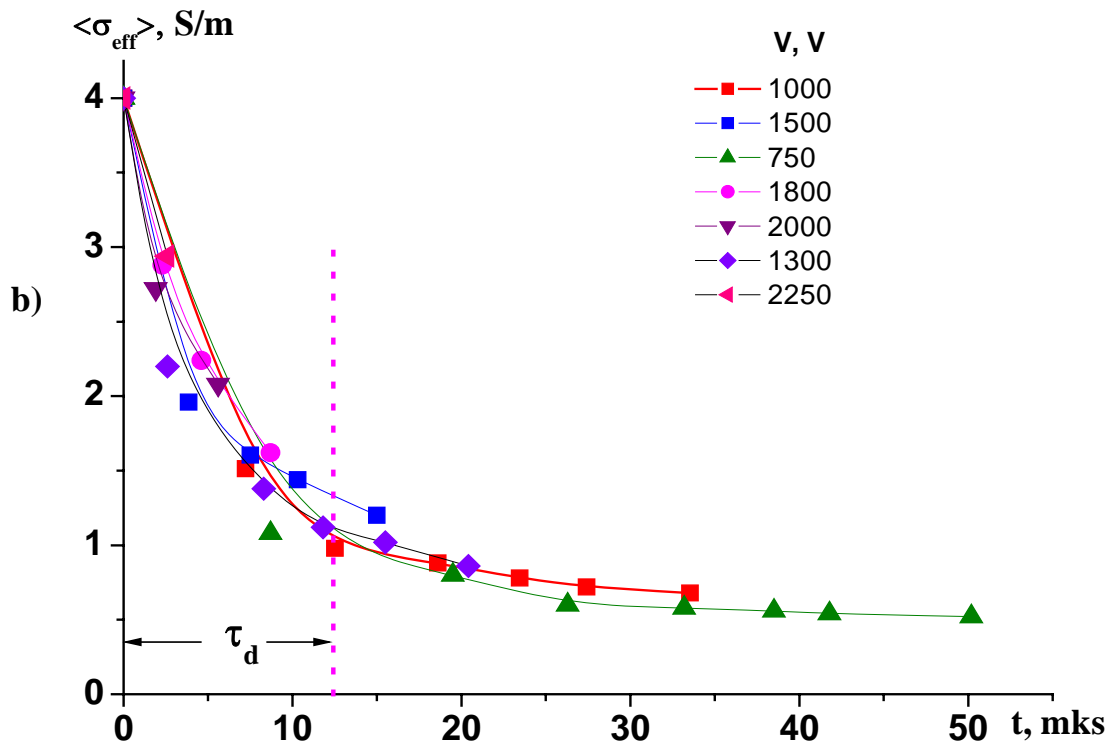
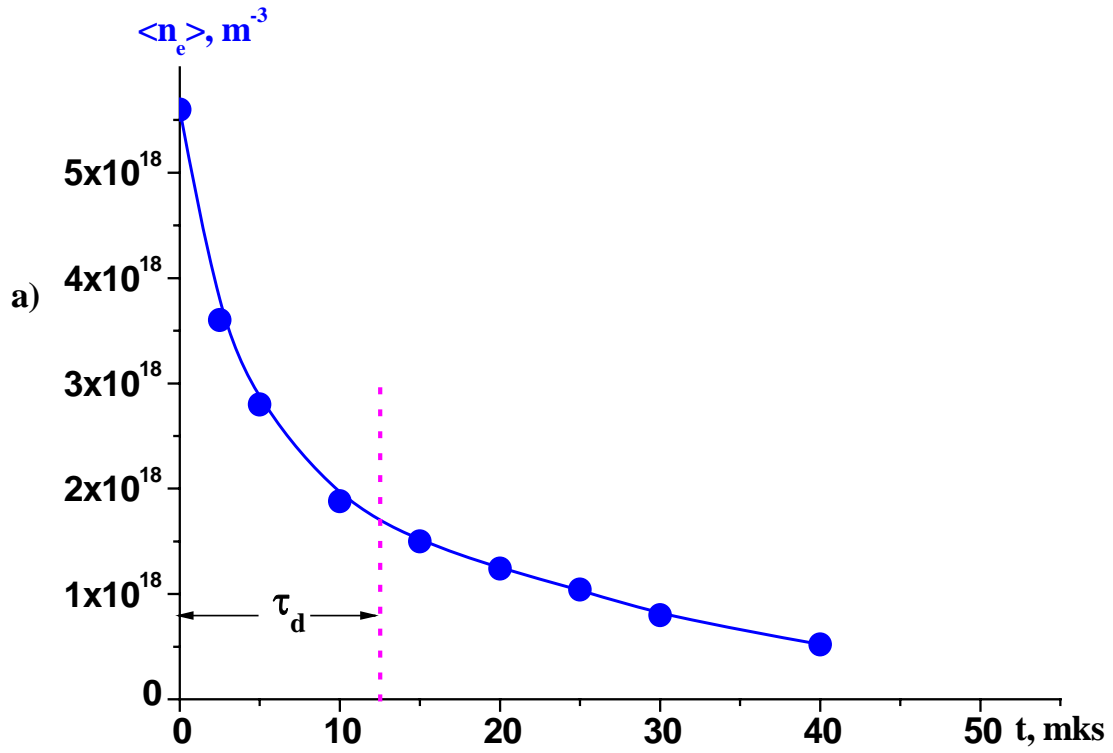


**Fig.1.1.10.** Plasma decay after HF discharge: a) electron concentration at  $V = 2000$  V; b). conductivity at various voltage on the capacitor  $C_1$

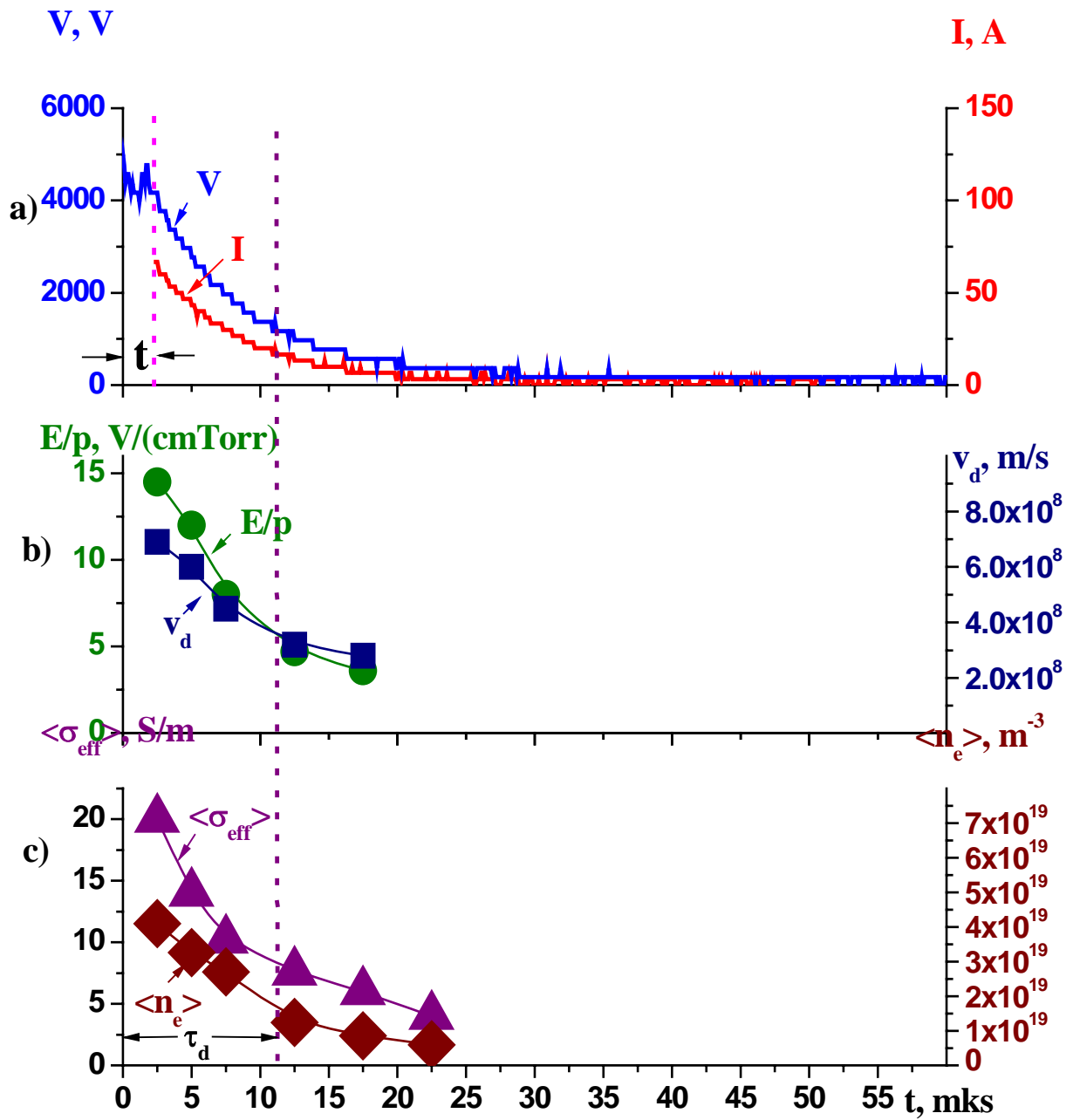


**Fig.1.1.11.** Combined discharge: a) voltage  $V$  and current  $I$ ; b) Ratio of electroc field intensity to pressure ( $E/p$ ) and electron drift velocity  $v_d$  c) average effective conductivity  $\langle \sigma_{eff} \rangle$  and electron concentration  $n_e$ .

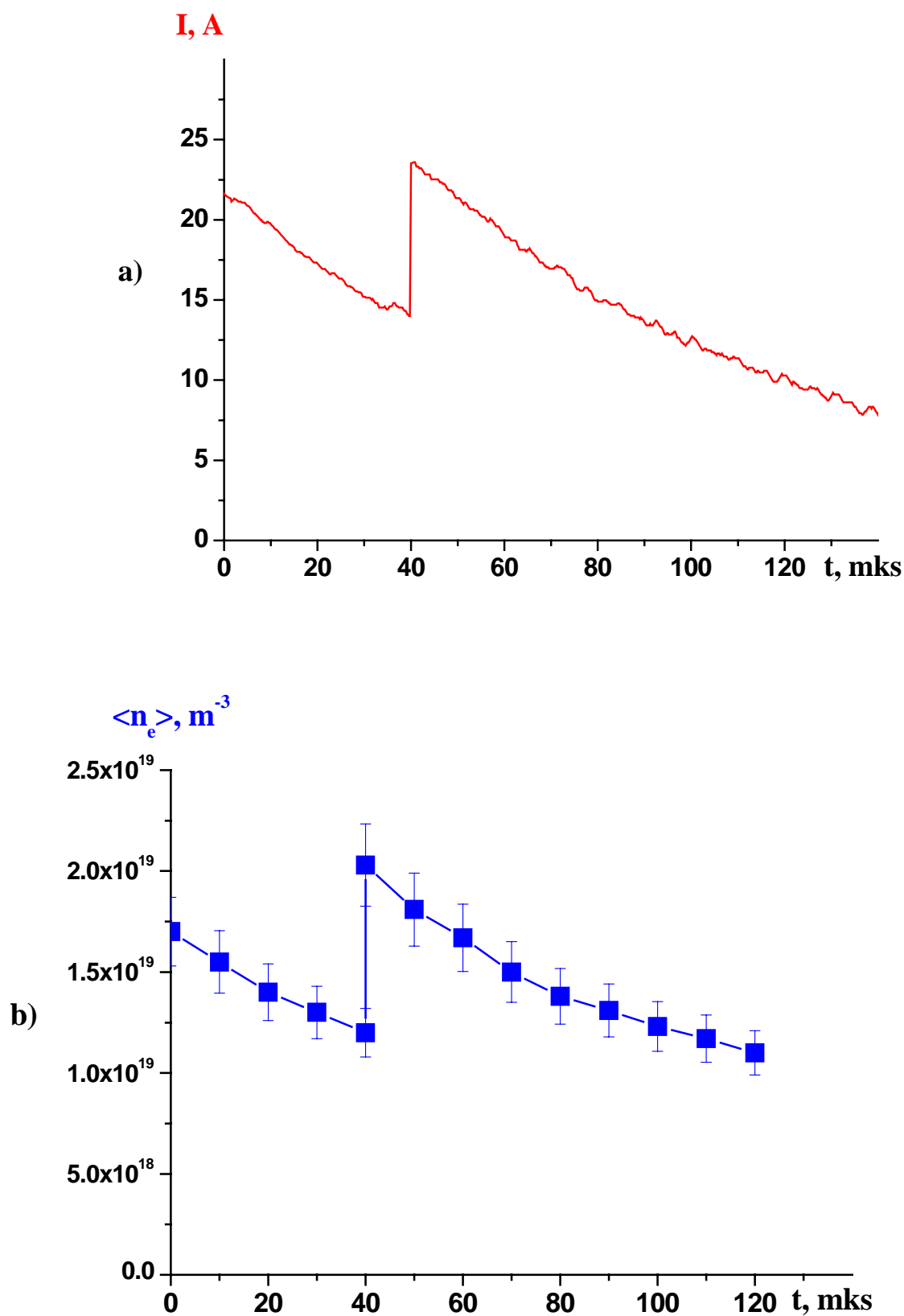


**Fig. 1.1.12.** Two pulse discharge. a) Total current with time; b) Electron concentration with time



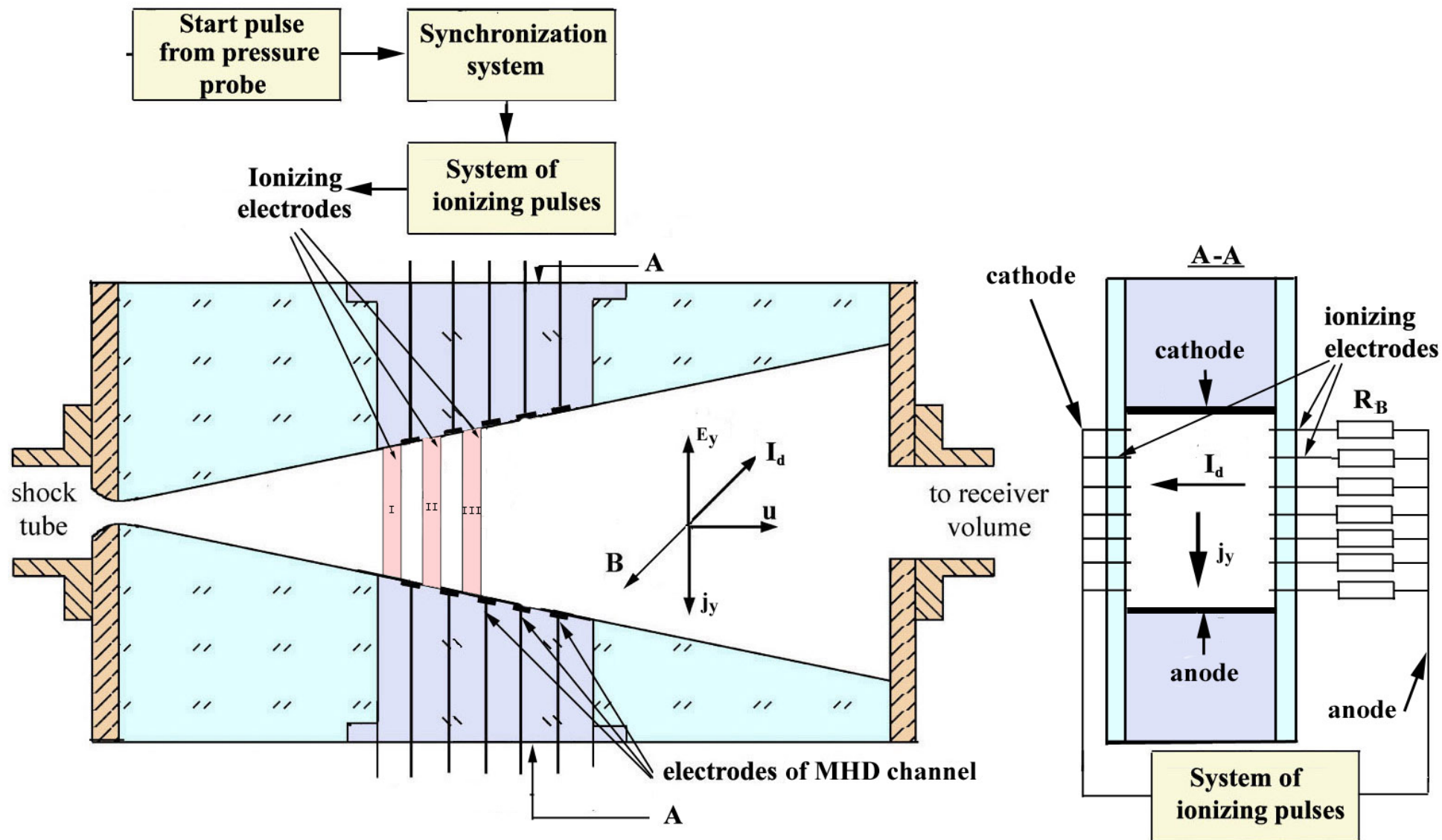


Fig.1.1.13. Scheme of working chamber and directions of main vectors.

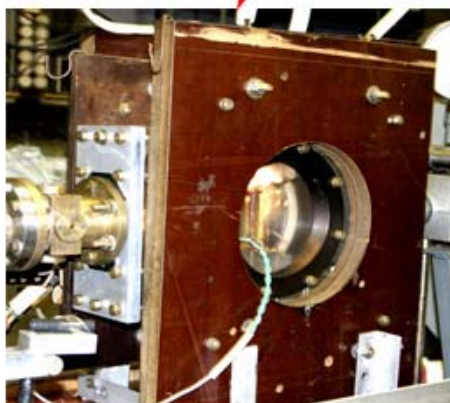
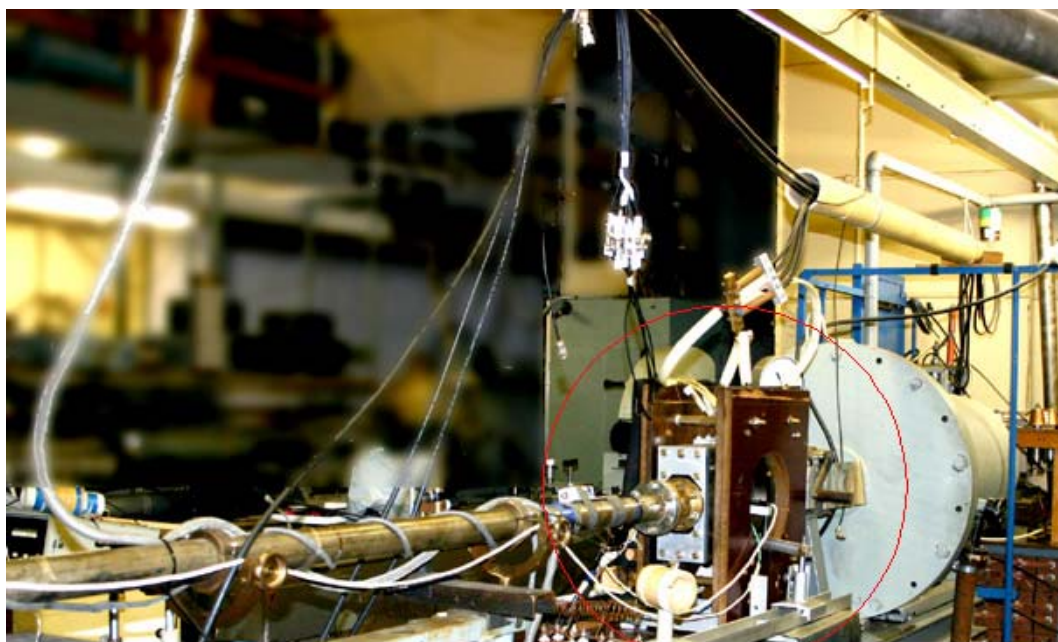


Fig.1.1.14. Photograph of working chamber.



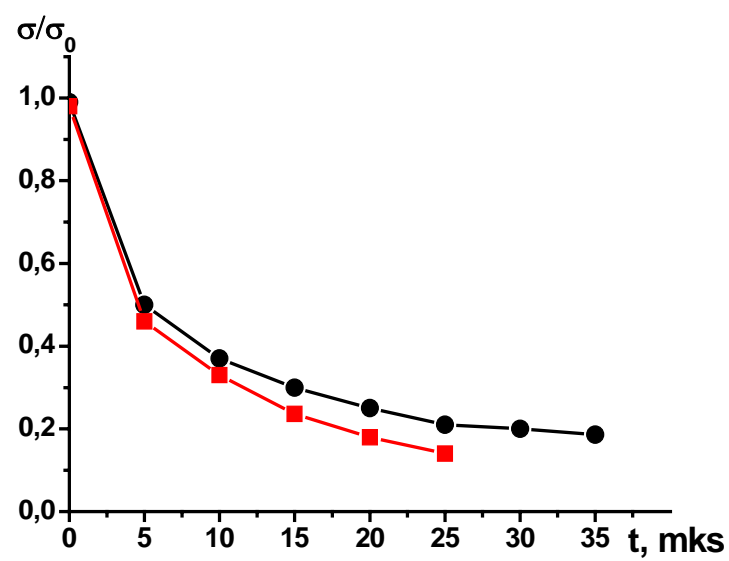


Fig.1.1.15. Conductivity decrease vs time at plasma decay in non-moving gas.  
Circles -  $\sigma_0 = 4 \text{ Sm/m}$ , squares -  $\sigma_0 = 20 \text{ Sm/m}$ .

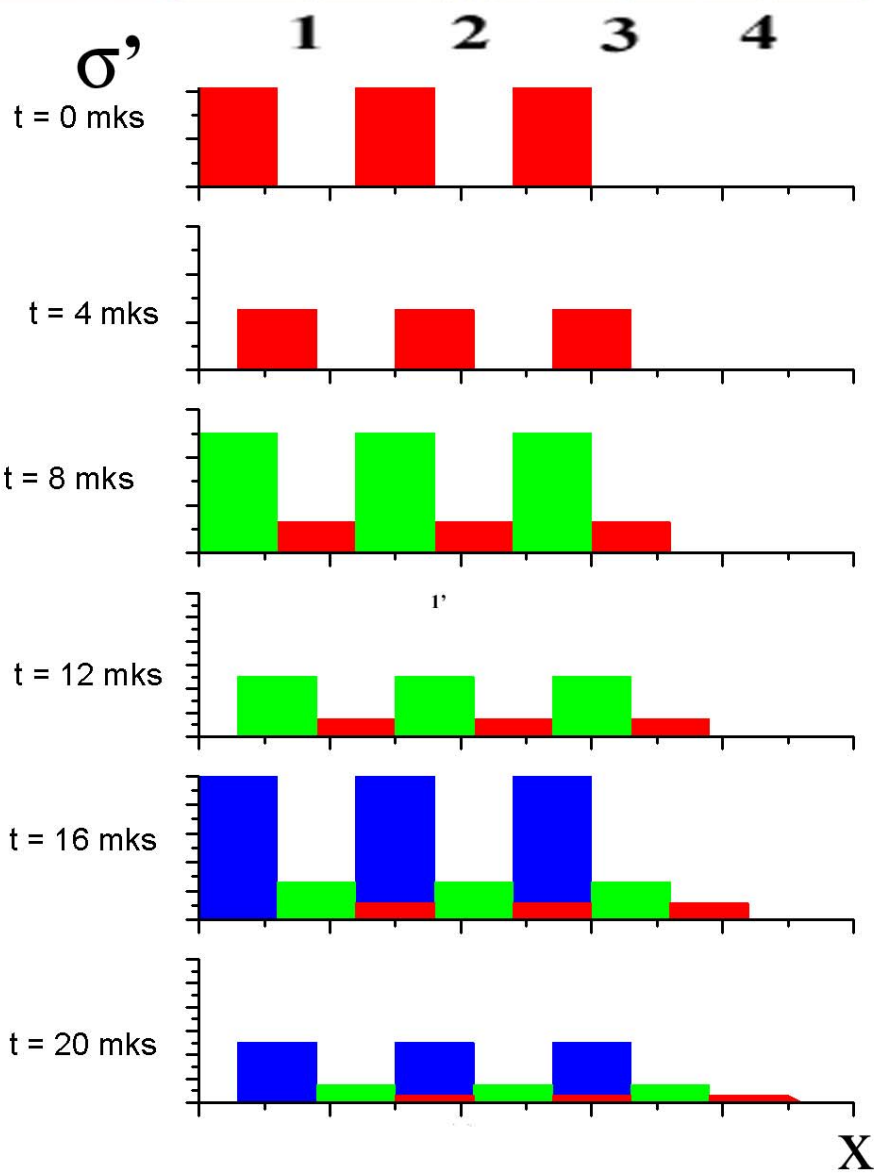
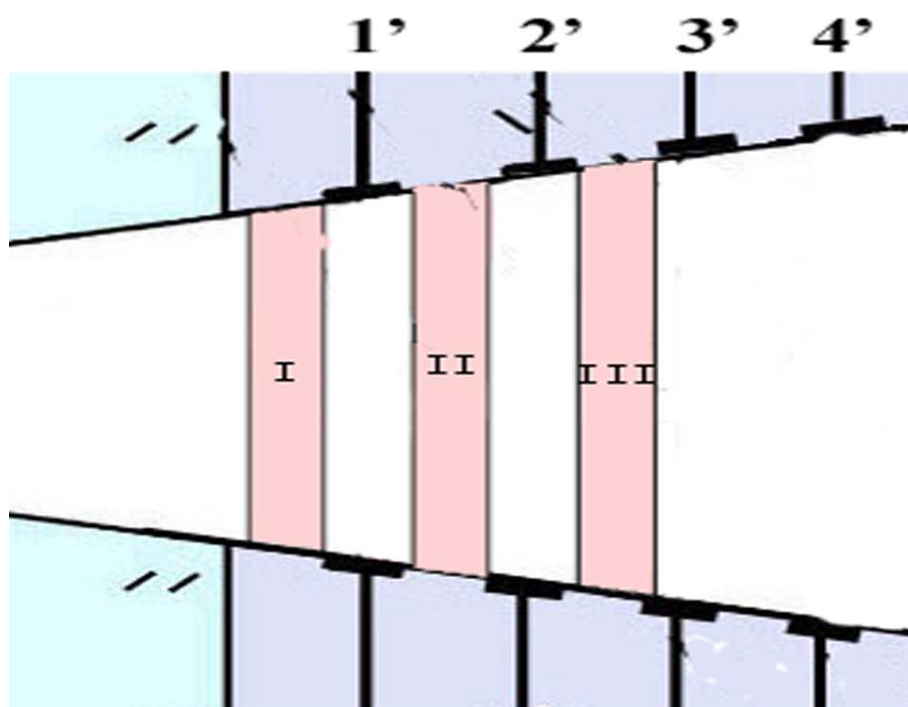


Fig.1.1.16. Scheme of ionizing pulses.

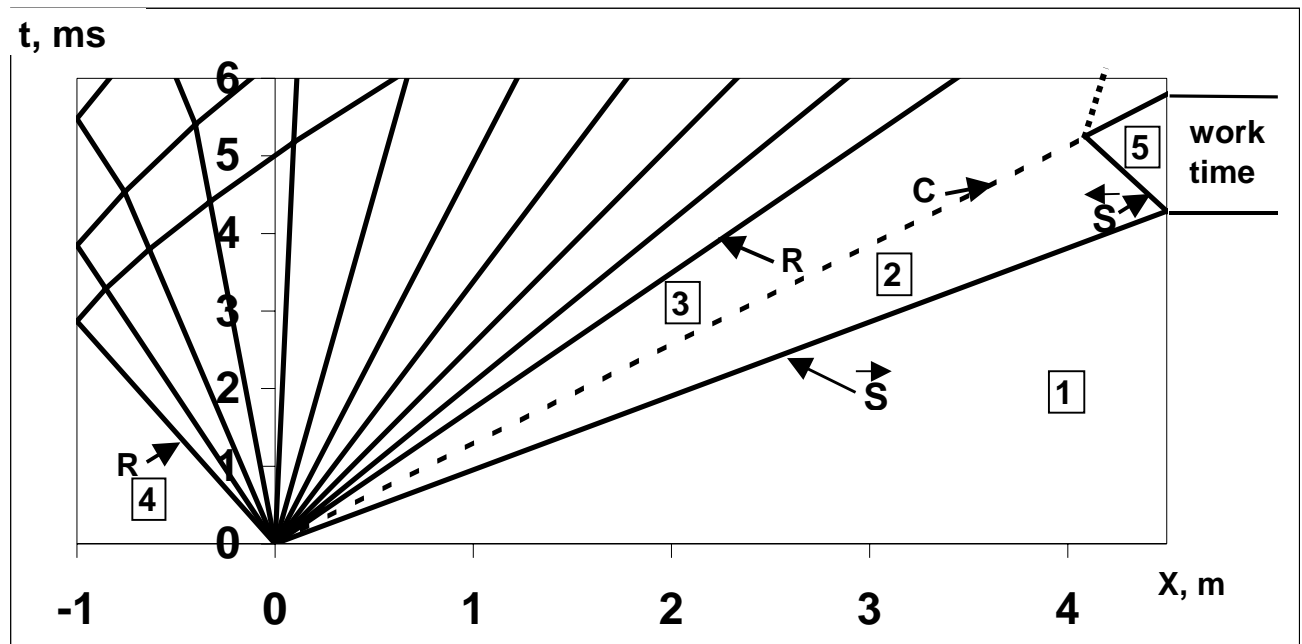


Fig.1.1.17. Determination of working time of shock tube with the help of  $x-t$  diagram.

Air-air,  $p_4/p_1=650$ ,  $M=3.001$ .

S is incident shock wave, S is reflected shock wave, C is contact surface, and R is rarefaction wave.

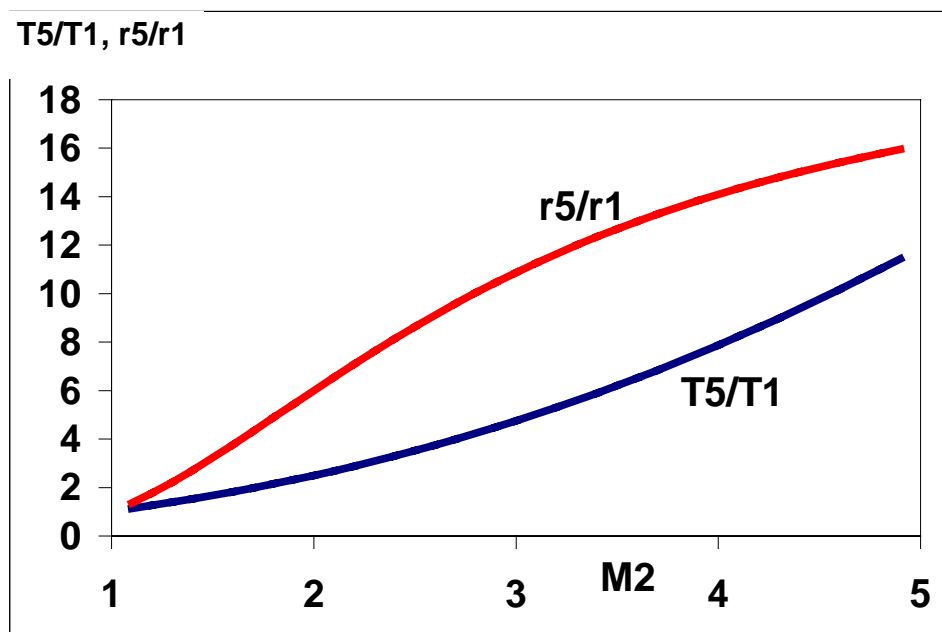


Fig.1.1.18. Relative values of stagnation temperature and density vs different values of incident shock wave Mach number  $M_2$

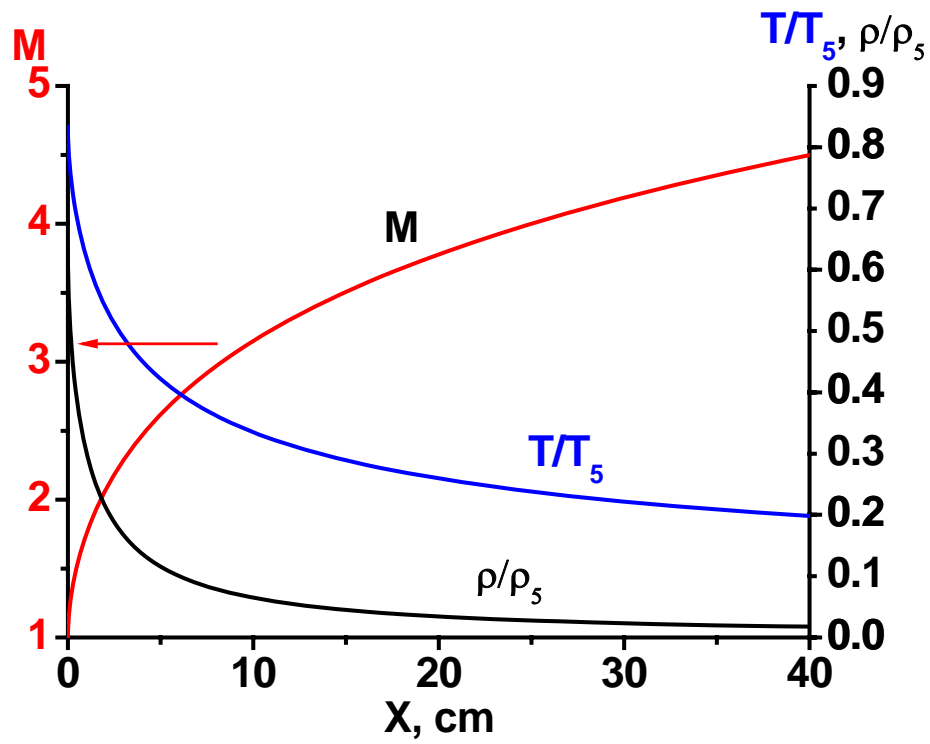


Fig. 1.1.19. Distribution of Mach number, and relative values of density and temperature along channel axis.

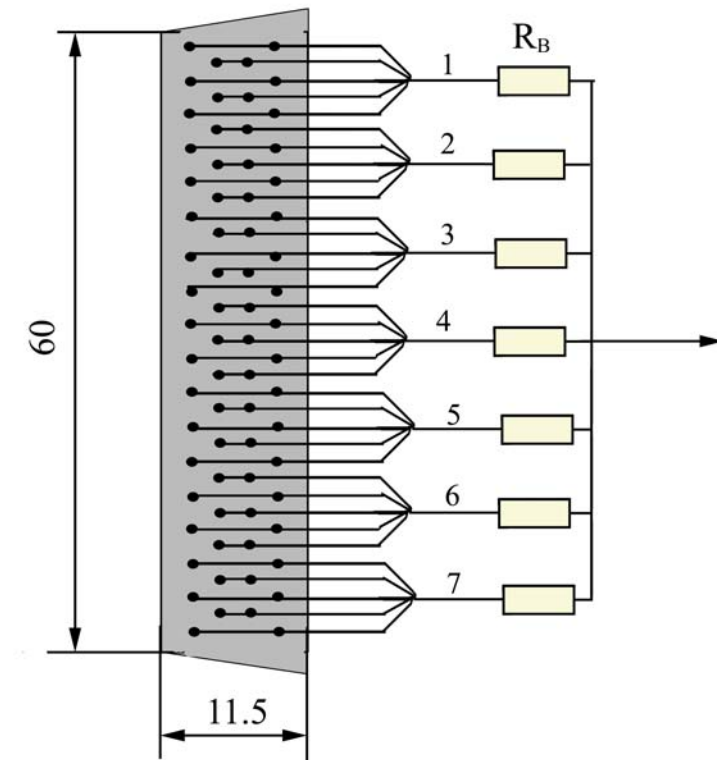


Fig.1.1.20. Formation of pin electrodes from the separate sticks (digits are number of pins) and connection it with ballast resistances.

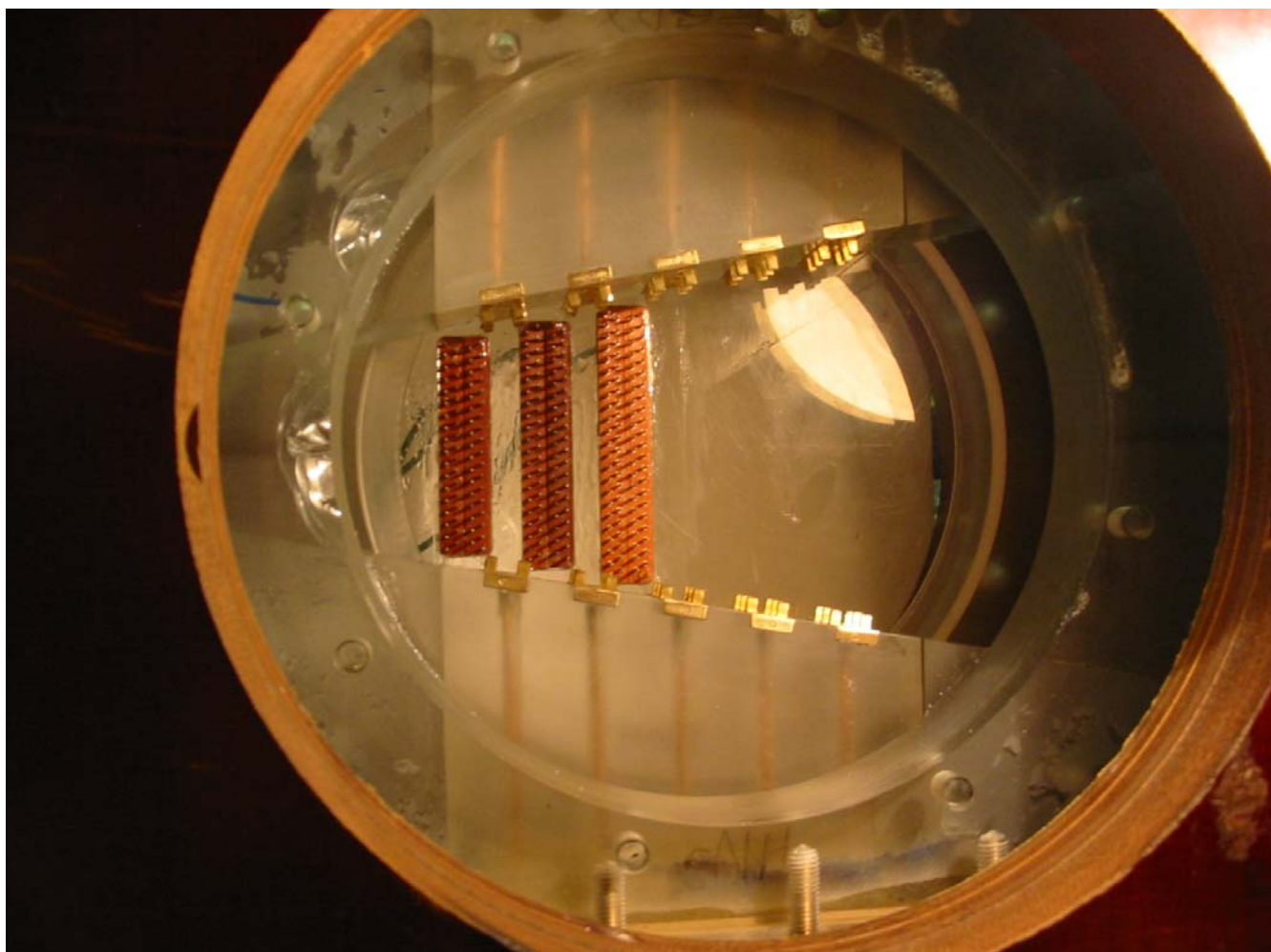


Fig. 1.1.21. Photo of lateral side of working chamber with ionizing electrodes and MHD channel electrodes.

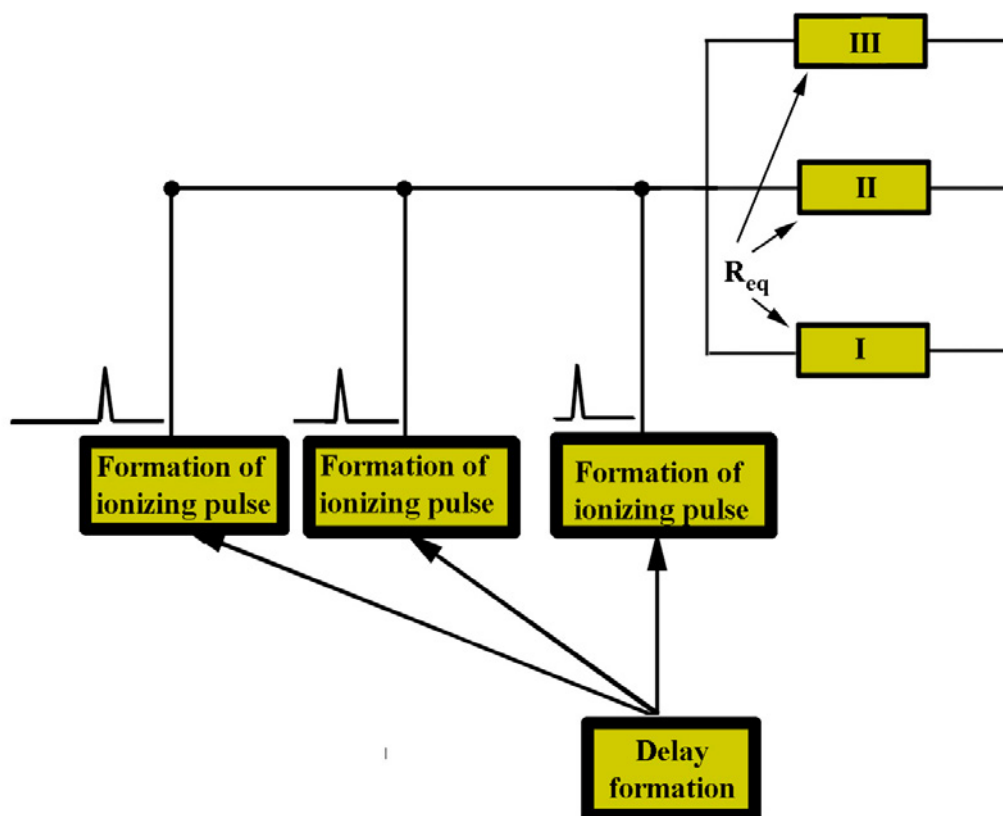


Fig.1.1.22. Scheme of ionizers connection

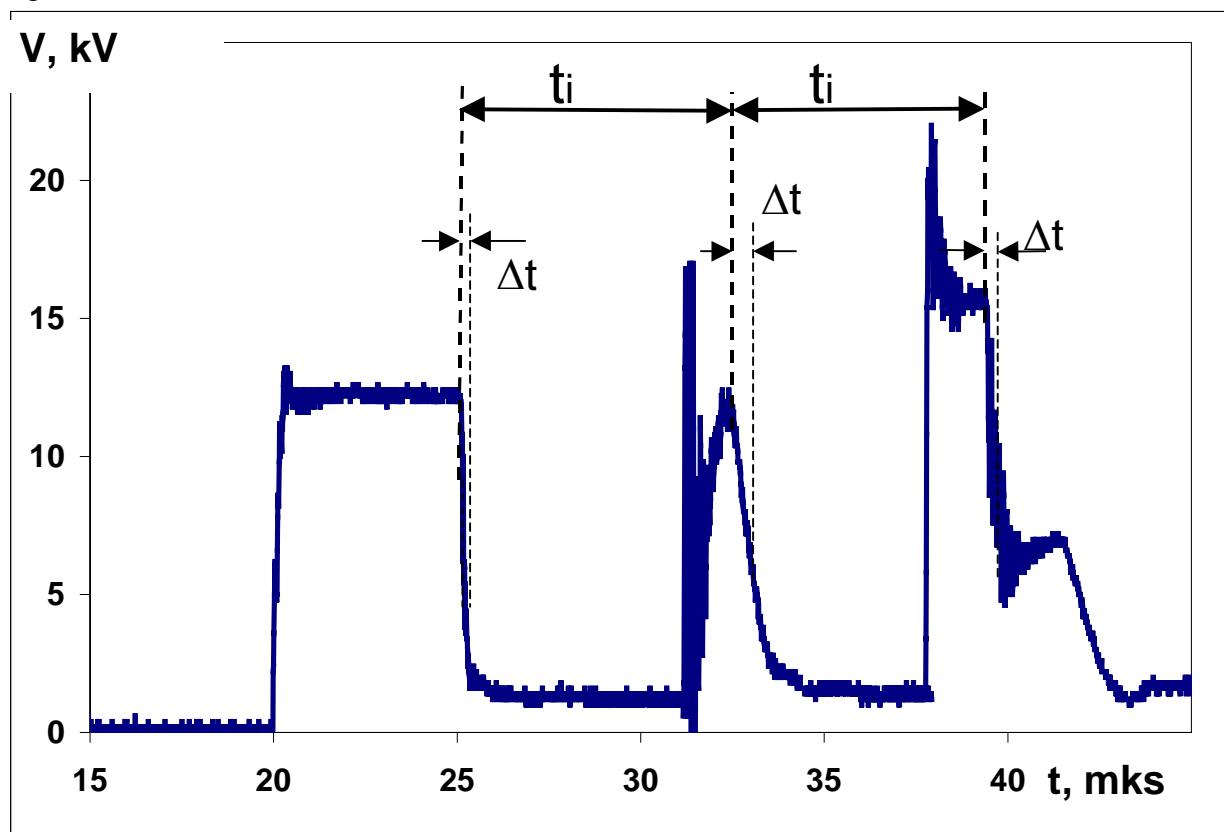


Fig.1.1.23. Oscillogram of voltage of three discharges in non-moving gas. Time delay between discharges is 8 mks.

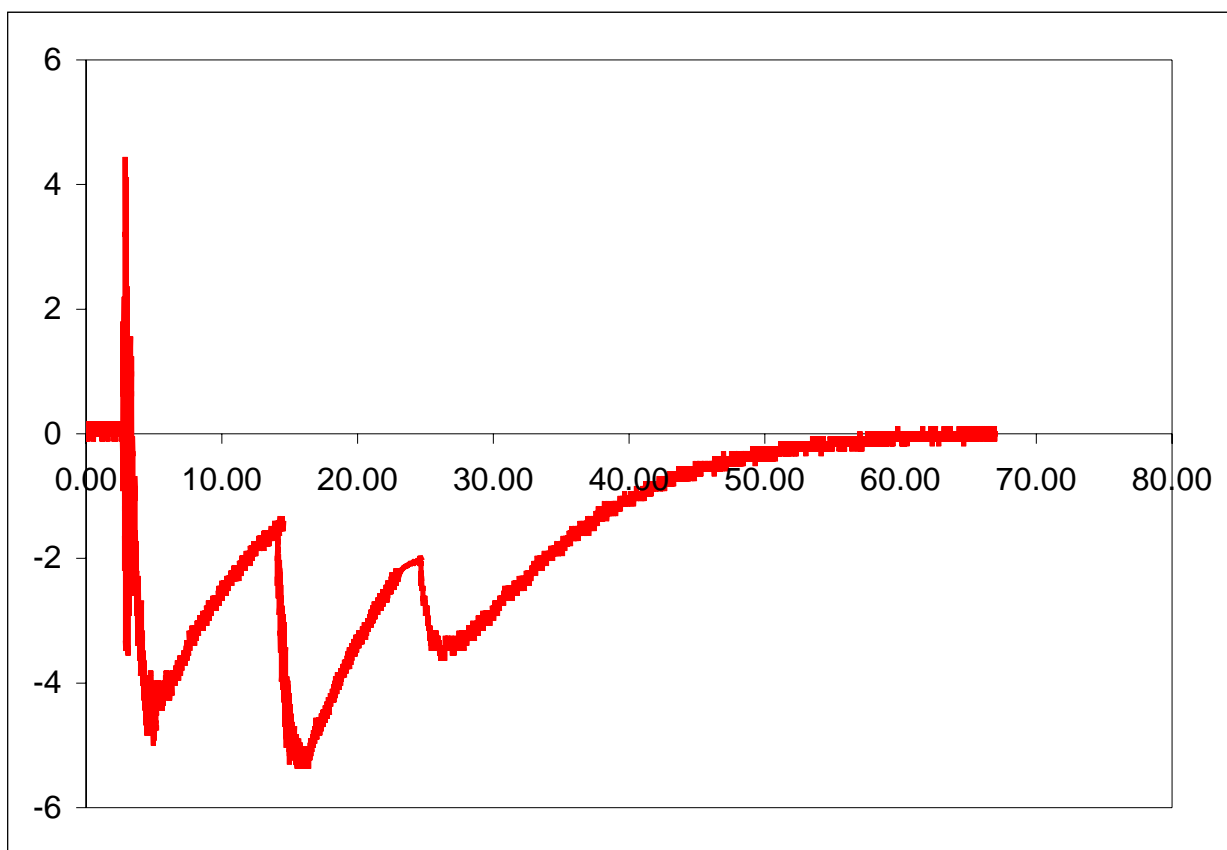


Fig.1.1.24. Oscillogram of luminosity of three discharges in non-moving gas started with time delay.



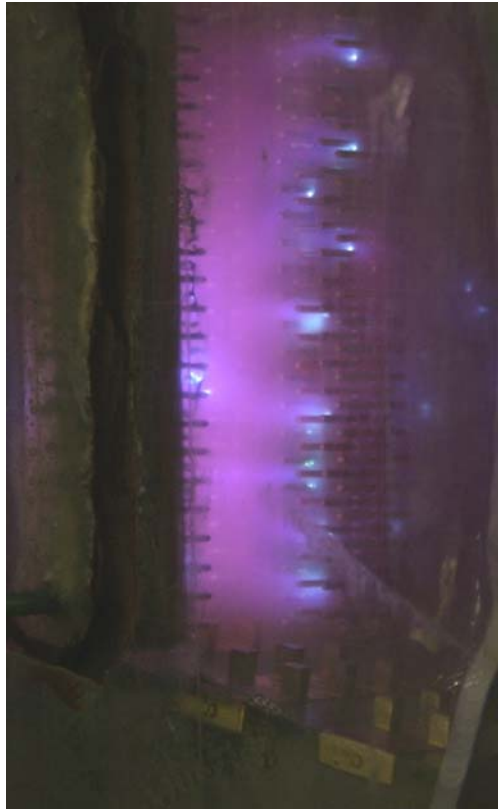


Fig.1.1.25. Photo of the discharge

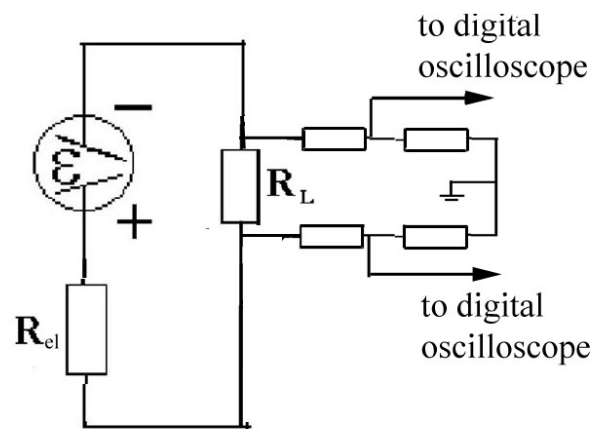


Fig.1.1.26. Equivalent scheme

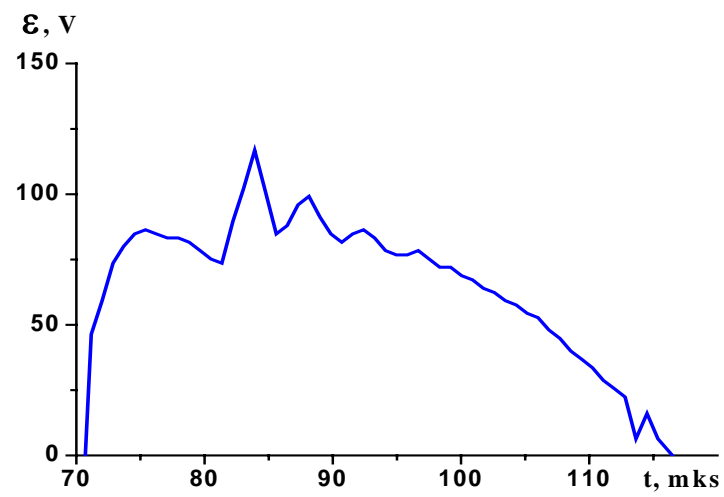
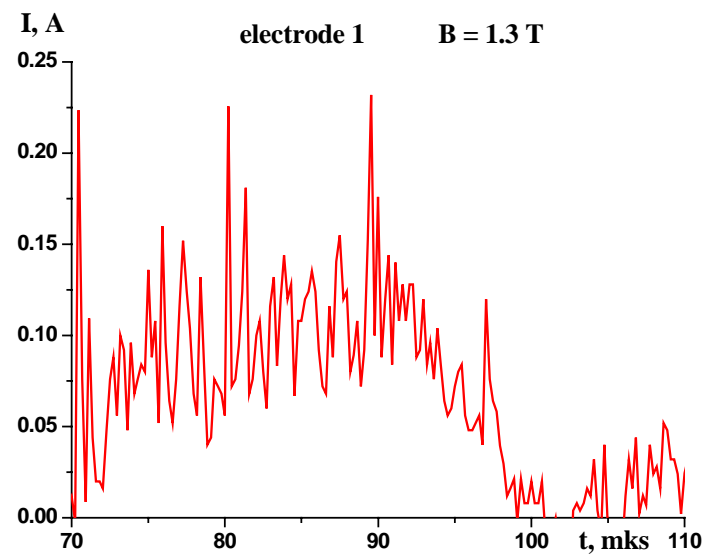


Fig.1.1.27. Oscillogram of EMF



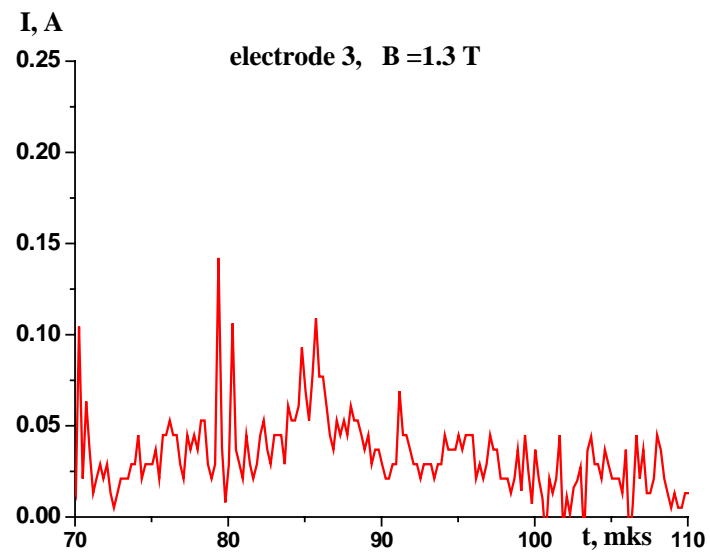
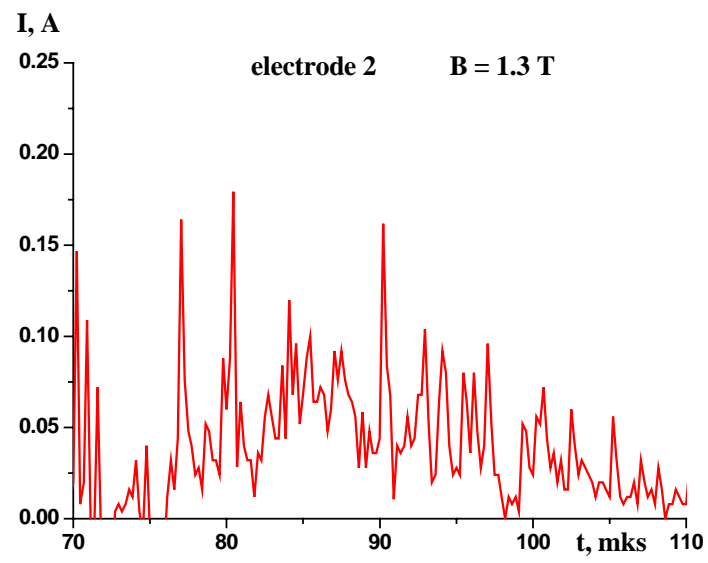


Fig.1.1.28. Oscillogram of magneto-induced current

## **2. Experimental investigations of magnetic field–supersonic flow interaction at the Ioffe Institute Big Shock Tube (BST)**

### **2.1 Introduction**

Our investigations during the last three or four years have shown that the experimental equipment developed on the basis of the BST is a convenient and comparatively simple tool for studying interaction between a supersonic flow of weakly ionized plasma and magnetic field [1, 2].

At the initial stage, the investigations were carried out with the use of a test section of a rectangular cross section housing a supersonic nozzle. A plane supersonic flow about a flat plate at an angle of  $15^\circ$  was considered. At the lateral edges of the plate, electrodes are located that are connected to a voltage source providing an electric current through the plasma directed normally to the flow velocity vector.

An external magnetic field is established by two axially located coils through that a current pulse with a strength of  $\sim 30$  kA and duration of  $\sim 4$  ms passes in the course of discharge of a capacitor bank with a store of energy up to 0.4 MJ. The test section is located in between the coils. Interaction between the external magnetic field and the current through the plasma flow causes magnetohydrodynamic (MHD) impact on the supersonic flow that manifests itself, in particular, in changing the shock wave configuration of the flow pattern. The direction of the electromagnetic force (Lorentz Force) may either coincide with the direction of the flow velocity vector or be oppositely directed. To change the Lorentz force direction it is necessary to alter the directions of either the current through the plasma or the magnetic induction vector.

At the plate there are also heat flux sensors recording variations of the heat flux to the plate under the MHD interaction.

An important factor of the MHD interaction is the conductance of the gas medium. The rate of ionization recombination of molecular gases is considerably higher than in inert gases. The employment of an inert gas as a working medium considerably facilitates carrying out experimental investigations inasmuch as, in this case, one can dispense with a special device (ionizer) for maintaining the necessary conductance. Therefore, as a working medium we used xenon. The gas conductance in the interaction region is provided by the residual ionization of the xenon preliminary heated by the reflected shock wave up to a temperature of  $\sim 9000$  K and then accelerated (expanded) in the nozzle.

The experimental investigations carried out allows us to find the following:

1. the effective MHD interaction is realized at a comparatively low magnetic induction of  $\sim 1$  T and a current through the plasma of an order of 1 kA
2. the region of MHD interaction is formed under the influence of the current passing through the plasma and practically independent of the initial ionization.

To prove the aforesaid in point 2 we realized an effective MHD interaction in a supersonic flow of molecular gas nitrogen [3] where the initial ionization is absent. The electric and magnetic parameters at that we studied MHD interaction in nitrogen turned out to be close to those in experiments with the xenon flow.

Experiments aimed at the MHD control of a supersonic flow of xenon and nitrogen convincingly showed advantages of the local MHD impact in the experimental modeling. However, the ways of implementation of the MHD interaction realized at the experimental complex modeled an internal flow. It is of interest to implement an MHD influence on an external flow about a body. The

simplest way to do this consists in employing a body of revolution with a magnetic system inside it.

As a base for a new design of the model to be studied we chose a body of revolution consisting of a sharp cone coupled with a cylinder. In the cylindrical section there is a coaxial coil serving as a source of pulsed magnetic field

Initially, the investigations were carried out in a flow of weakly ionized xenon plasma flowing about the model under study. The model was located inside the test section at the outlet nozzle cross section. The discharge of the capacitor bank through the coil provided the electric current pulse of the duration  $\sim 200 \mu\text{s}$  and with the amplitude 100 kA. It was supposed that under the action of the pulsed magnetic field near the body surface in the xenon plasma an electric current might arise. The interaction between the current and magnetic field, in our opinion, had to generate changes in the flow field which would reflect on the shock wave structure of the flow about the body.

In the experiments, we succeeded in establishing the magnetic field with the induction 2 T near the body surface. The further increase of the magnetic induction was interfered with the mechanical distraction of the magnetic coil and the model itself under the action of the electromagnetic force. The conductance of the supersonic plasma flow amounted to  $\sim 1000 \text{ S/m}$ . According to our estimates at such magnitudes of the magnetic field induction and plasma conductance the effective Start number does not exceed 0.01. The parameters established in the experiment turned out to be insufficient for realization of a noticeable interaction of the xenon plasma flow with the magnetic field.

In spite of the negative result of these experiments, in our opinion, application of such an approach may turn out more successful when studying an impact of a pulsed magnetic field on a plasma flow inside a channel. In this case, the magnetic induction can be considerably increased by increasing the electric current to achieve the Stuart numbers necessary for the effective interaction. The mechanical strength of the coil can be enhanced by strengthening its outside.

## 2.2 Design of the model under study

In the experiments carried out earlier the electromagnetic force was directed either downstream or upstream, thus this made it possible either to accelerate the flow or to decelerate it.

With regard to the model geometry and the place of location of the magnetic coil it is technically difficult to impact on the flow by the electromagnetic force in the same way as before. Therefore, we proposed and realized another mechanism of the influence on the supersonic gas flow consisting in changing the parameters of the supersonic flow due to heating the gas. The heating performed by an electric current passed through the gas causes local variations of the gasdynamic parameters including the shock wave structure. Interaction of this current with the magnetic field of the coil leads to emergence of the electromagnetic force that will displace the region of local heating about the body surface.

Figure 2.1 shows the schematic of such a device. The object under study is a body of revolution consisting from a sharp cone coupled with a cylinder. Inside the cylindrical part of the model there is a magnetic coil (1). The coil is wound onto a magnetic core (2) of the cylindrical shape 26 mm in diameter. The cone opening is  $60^\circ$ . Along the core axis a brass electrode (3) of 6 mm in diameter with the conical fore end is located. The space between the magnetic core and the central electrode is

filled in with epoxy (5). The magnetic core is manufactured from a special steel with low residual magnetization (narrow hysteresis loop) and plays the role of a magnetic circuit.

The region of interaction of the discharge plasma with the magnetic field is located between the outer conical surfaces of the central (3) and ring (4) electrodes. The ring electrode being a part of the magnetic core is connected to one of the coils ends, and the second coil end is connected to an external voltage source. Another pole of the voltage source is connected to the central electrode (3). The electric diagram of the circuit is shown in Fig. 2.2.

As a source of the pulsed voltage we use a circuit with the distributed parameters consisting of 14 *LC* cells. Before the experiment this circuit is charged up to the necessary voltage by a source of direct current. A high-voltage transformer with a low inductance is connected in series into the discharge circuit. The transformer forms a short ( $\sim 1 \mu\text{s}$ ) triggering pulse of a high voltage (about 30 kV). This pulse initiates an electric breakdown through the discharge gap between the central and ring electrodes and provides the discharge of the *LC* circuit. The current with the strength  $\sim 10^3 \text{ A}$  arisen in the discharge gap is affected by the magnetic field established by the inductor (*I*) which causes azimuthal rotation of the discharge channel around the body.

Figure 2.3 shows the appearance of the body of revolution with the inductor. The cylinder diameter is 28 mm, total length is 62 mm, cone opening is  $60^\circ$ . The magnetic coil consists of 20 turns of a wire of 1 mm in diameter.

## 2.3 Results of measurements

The first measurements were conducted with no supersonic flow. The air pressure in the test section was maintained at a level up to 0.1 atm which approximately corresponded to the pressure in the supersonic flow at the outlet nozzle cross section. In these experiments, the total over time plasma radiation from the region near the body and Schlieren patterns of the flow corresponding to various time instants beginning from the discharge onset were recorded.

To evaluate the rotation speed of the discharge plasma around the body we employed a photo recorder operating in the waiting regime (photo scanner). The image of the conical surface of the model was focused onto a film with the help of a rotating reflecting prism and was displaced over the film at a preset velocity. The image size along the scanning direction was bound with the help of a special slit diaphragm of 2 mm in width. In this way the spatial-time scanning of the illumination of the body surface section chosen was performed.

The discharge in the gas occurred during approximately 1 ms, the electric current flew from the central electrode to the ring one. The current pulse shape is shown in Fig. 2.4. In Fig. 2.4 it is seen that the rise time of the current is about  $300 \mu\text{s}$  after the initiation. An analysis of the Schlieren patterns shows that approximately in the same time the distribution of perturbations near the body loses the asymmetry distinctly expressed at the initial stages of the discharge.

Figure 2.5 displays the total over time pattern of the gas radiation from the body vicinity. It is seen that the radiation region is practically symmetric relative to the body and partially propagates over the cylindrical body surface. Near the conical surface, the radiation is more intensive, which, probably, is associated with a higher current concentration in this region. The frequency of plasma rotation around the body increases with decreasing the gas pressure.

The second series of the experiments was carried out when the model was located in a supersonic nitrogen flow. Nitrogen in the shock tube was heated by the reflected shock wave up to the temperature  $\sim 1800$  K. The constancy of the gas parameters behind the reflected shock wave was retained during 2 ms. The object under study was located inside the test section downstream from the outlet nozzle cross section. The mainstream flow parameters amounted to: the gas pressure 50 mbar, density  $0.04 \text{ kg/m}^3$  temperature 440 K, gas velocity 1600 m/s, Mach number 4.

In the experiments, the current strength varied by changing the voltage of the external source, the current amplitude reached 1500 A. The current direction remained the same as in the previous experiments – from the central electrode to the ring one. The initiation of the discharge of *LC* circuit through the inductor located inside the object under study was performed after the steady-state flow through the nozzle was formed.

Figure 2.6 shows Schlieren patterns of the supersonic nitrogen flow about the body of revolution with no MHD effects and with the presence of them. In Fig. 2.6a there is a pattern of the steady-state flow about the body with no MHD interaction. The last three patterns corresponding to various time instants from the onset the current through the gas convincingly evidence the strong impact by the revolving discharge on the wave flow structure. The flow pattern becomes asymmetric and changes as the discharge region displays about the conical body surface. In the photos a comparatively narrow discharge region near the body surface is well seen. Between the boundary of the discharge region and the shock wave front there is a region of less hot gas. The flow above the cylindrical surface is featured by the presence of strong turbulent inhomogeneities which manifests themselves specially brightly in photos corresponding to the late phase of the process.

The frequency of rotation of the body in these experiments amounted to approximately 30 kHz. It was found that this magnitude is practically independent of the current strength and magnetic induction of the field.

An interesting result was obtained when changing direction of the electric current through the plasma: the central electrode was connected to the negative pole of the voltage source and the ring electrode – to the positive one. In this case, the current through the plasma and vector of magnetic induction invert their directions, while the direction of rotation of the discharge is retained. The frequency of rotation of the discharge in this case decreased practically by a factor equal to 2 and amounted to 14 kHz.

Figure 2.7 shows  $x-t$  scanning obtained at different directions of the electric current through the plasma: the upper one corresponds to the current direction coinciding with the flow velocity vector, the lower one – to the opposite direction. To time scanning there corresponds the horizontal axis, the direction of the vertical axis coincides with the cone generatrix from the vertex of the cone to its base. The scanning speed in both experiments is the same.

Attention is drawn to considerable change not only in the illumination spot repetition frequency but in their internal structure.

A reason for such an effect, probably consists in the structure of electric discharge through a gas. On the one hand, formation of cathode spots at the cold electrode surface (cathode) promotes concentration of the electric lines of force near the spot. Because the electromagnetic strength is proportional to the density of electric current, in the case of connection the negative pole of the voltage source to the ring electrode (cathode), the velocity of rotation of the discharge plasma around the body is higher than at the opposite connection.

On the other hand, due to nonuniformity of the potential distribution in a linear gas discharge where the potential gradient near the cathode is larger than near the anode, it is possible to suppose that the heat release in the discharge region is also larger near the cathode.

The aforesaid is confirmed by the result of the following experiments. The heat flux was measured in quiescent air at a pressure of 50 mbar and at different directions of the current through the discharge plasma. The measurements were carried out by gradient heat flux sensors [6-7] located at the cylindrical part of the model (see Fig. 2.8). Figure 2.9 shows signals produced by the sensor located closer to the conical surface of the model at two opposite directions of the current through the discharge plasma. Remind that the current direction was altered by changing of connection of the external voltage source to the electrodes. Curve 1 in the plot corresponds to connection of the negative terminal of the voltage source to the ring electrode, and curve 2 – the positive one. In the plot it is seen that the heat flux is appreciably larger when the ring electrode play the role of cathode.

When the model is placed into a supersonic nitrogen flow, the heat flux distribution over the model surface changes. In Fig. 2.10 there are signals of the heat flux located at the middle of the cylindrical part of the model at the opposite directions of the current passage. Attention is drawn to a considerable increase of the heat flux as compared with a quiescent gas (see Fig. 2.9) and emergence of heat flux pulsation. When the ring electrode plays the role of anode, the pulsation is more distinct and its frequency corresponds to the frequency measured with the help of the photo scanner. The average magnitudes of the heat flux to the model surface at the opposite current directions differ less from each other than in a quiescent gas, which probably can be explained by the drift of the discharge plasma by the supersonic flow toward the heat flux sensor. However, when the ring electrode plays the role of anode, the heat fluxes remain noticeably less.

An analysis of the Schlieren patterns in the case when the ring electrode is cathode shows that there are no noticeable changes in the shock wave structure of the flow about the model. The position and shape of the attached bow shock wave near the conical surface remain practically the same as in Fig. 2.6.

Note that in spite of nonstationary character of the process, pulsation of the heat flux is relatively small as compared with its average magnitude. Probably, this is explained by that the discharge is not localized but occupies some gas volume. Rotation of this volume in the azimuthal direction provides a distribution of the gasdynamic parameters, and, in particular the heat flux, close to steady-state one. Thus, the facility designed can be employed for modeling thermal processes in supersonic flows about bodies. Such an approach to modeling thermal processes in molecular gases in a shock tube seems very promising because reaching high parameters of a supersonic plasma flow of a needed duration by means of heating a working molecular gas by shock wave compression is associated with considerable difficulties.

## 2.4 Conclusions

1. An original MHD facility for ionization of a supersonic gas flow about a body of revolution is designed and successfully tested. The principle of operation of the facility is based on displacement by a magnetic field of a strong thermal inhomogeneity about the surface of a body of revolution in the azimuthal direction

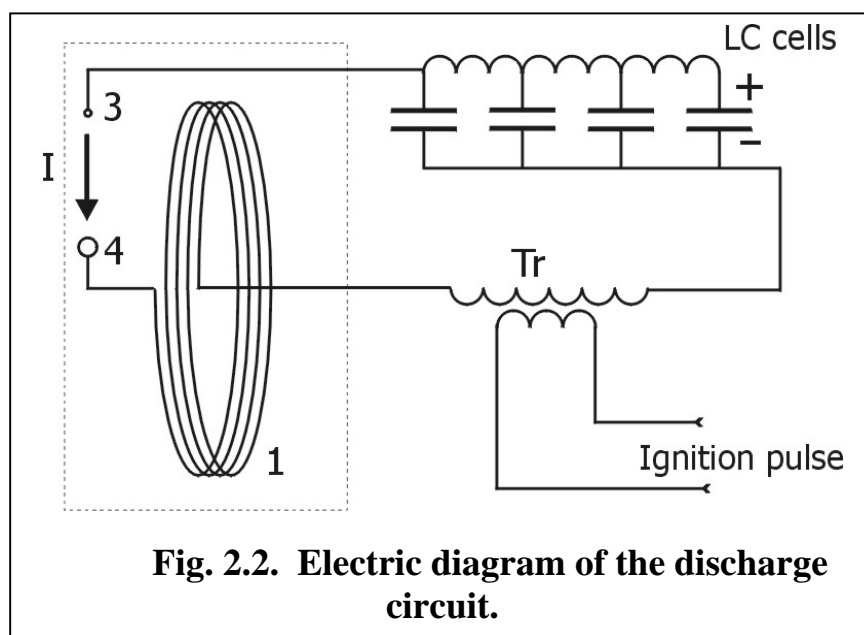
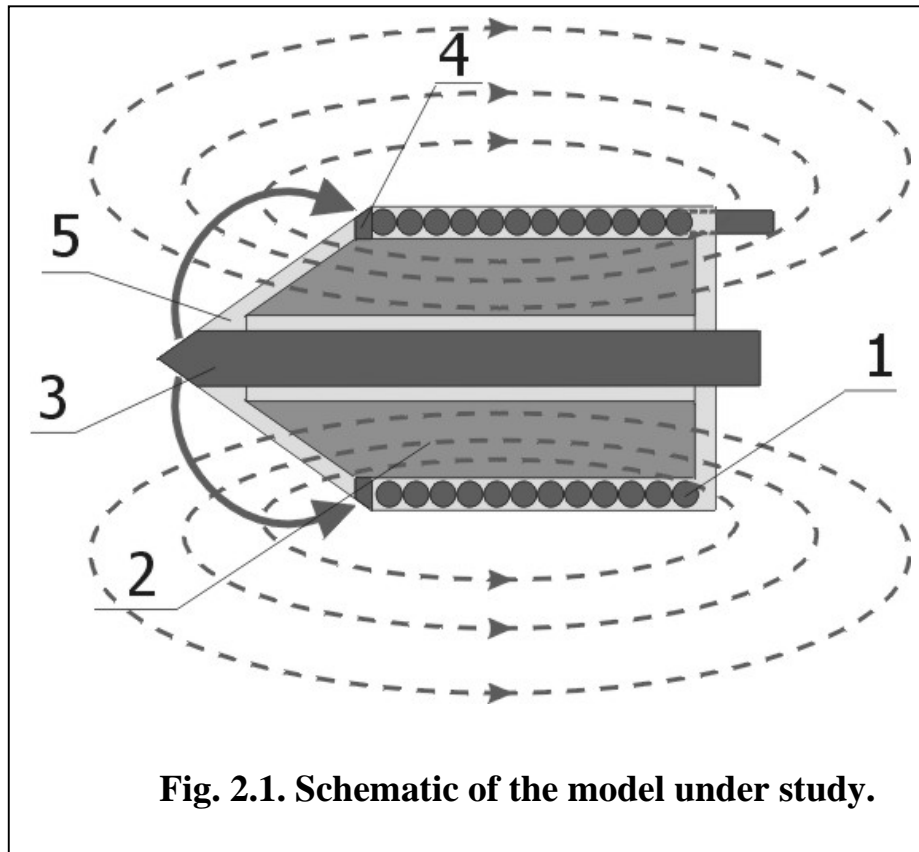


The facility allows one to realize an effective impact on the shock wave flow structure and its gasdynamic parameters.

2. Technical implementation of the approach proposed for MHD control of a supersonic flow allows one to considerably extend possibilities of the experimental equipment existing at the Ioffe Institute and, in particular, in studying of thermal processes about bodies of revolution in supersonic flows of molecular gases.
3. The simplicity of the approach proposed admits various modifications of the facility construction and allows one to readily change interrelation between the thermal and force impacts onto the body surface by varying the discharge current strength, induction and geometry of the magnetic field.

## 2.5References

1. Bobashev S.V., Mende N.P., Sakharov V.A., and Van Wie D. M. MHD Control of the Separation Phenomenon in a Supersonic Xenon Plasma Flow. I. 41st Aerospace Meeting and Exhibit. Reno, Nevada, Jan. 6 – 9, 2003,. AIAA 2003-168.
2. Bobashev S., Mende N., Sakharov V., Van Wie D., “MHD Control of the Separation Phenomenon in a Supersonic Xenon Plasma Flow II”. 42nd AIAA Aerospace Sciences Meeting and Exhibit, Reno, Nevada, Jan. 5-8, 2004, AIAA-2004-515.
3. Bobashev S.V., Mende N.P., Sakharov V.A., and Van Wie D.M.. Magnetic Field Control of a Supersonic Nitrogen Flow. Tech. Phys. Lett., **30**, (8), 635 (2004).
4. Mitiakov V.Y., Sapozhnikov S.Z., Chumakov Y.S. et al. // 5th World Conference on Experimental Heat Transfer. Fluid Mechanics and Thermodynamics. Thessaloniki, Greece, 2001. P. 111-116.
5. Sapozhnikov S.Z., Mitiakov V.Y., Mitiakov A.V. 3rd European Thermal Science Conference. Heidelberg, Germany, 2000. P. 687-690.
6. Sapozhnikov S.Z., Mitiakov V.Yu., Mitiakov A.V., Petrov R.L., and Grigor'ev V.V., Bobashev S.V., Mende N.P., and Sakharov V.A. Heat flux measurement at the inner surface of a shock tube. Tech. Phys. Lett., **30**, (1), 76 (2004).



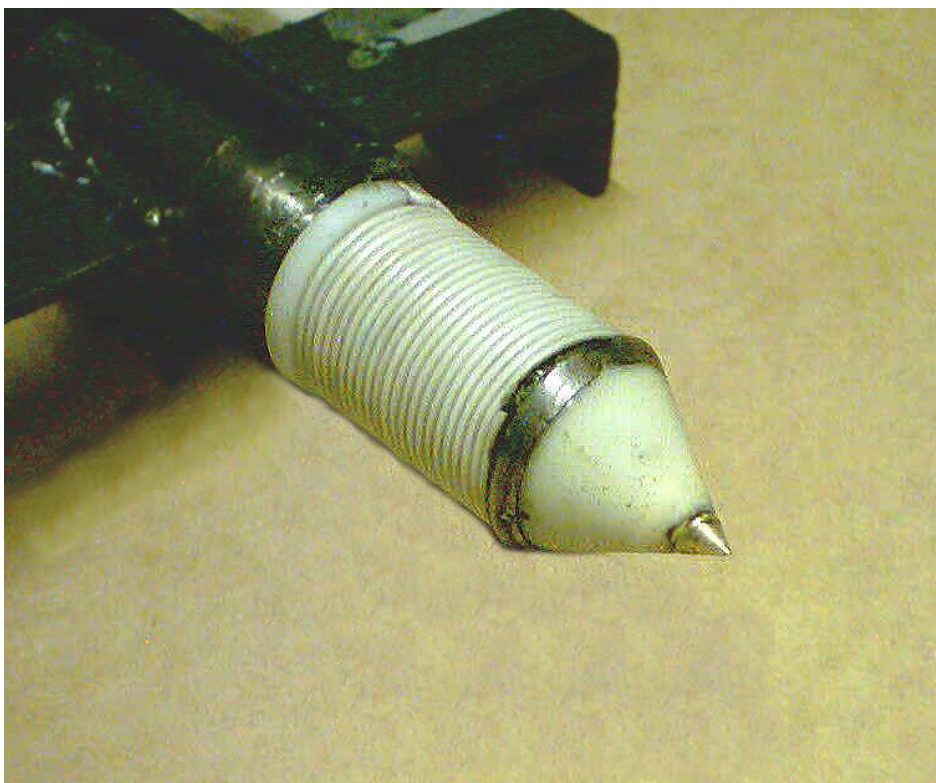


Fig. 2.3. Appearance of the model under study.

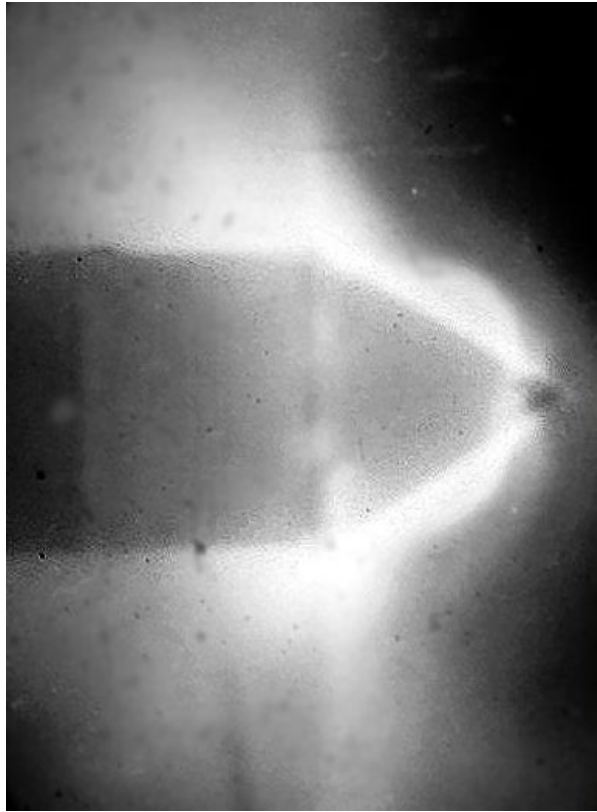


Fig. 2.4. A pattern of total over time plasma radiation from the region near the body in quiescent air.

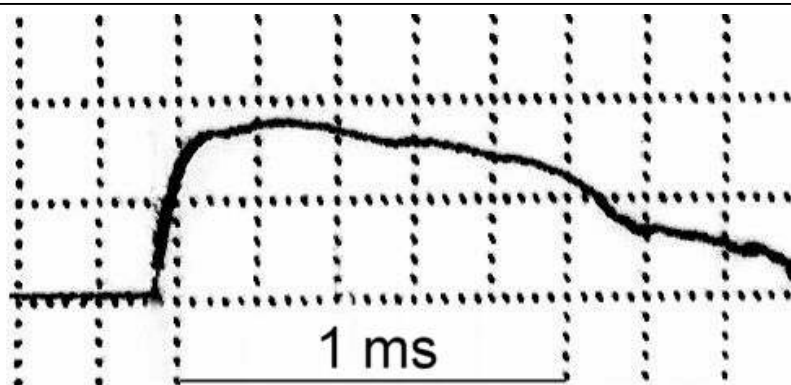


Fig. 2.5. A typical current pulse.

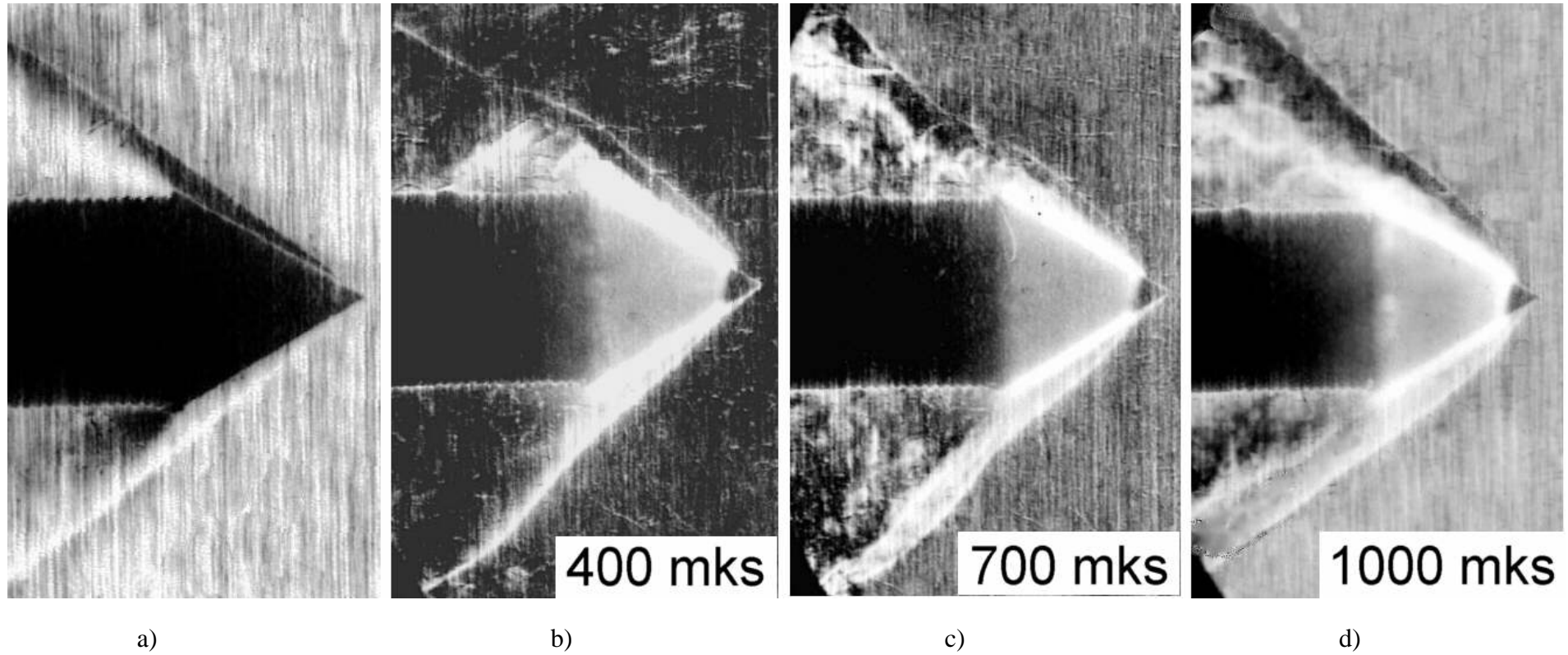
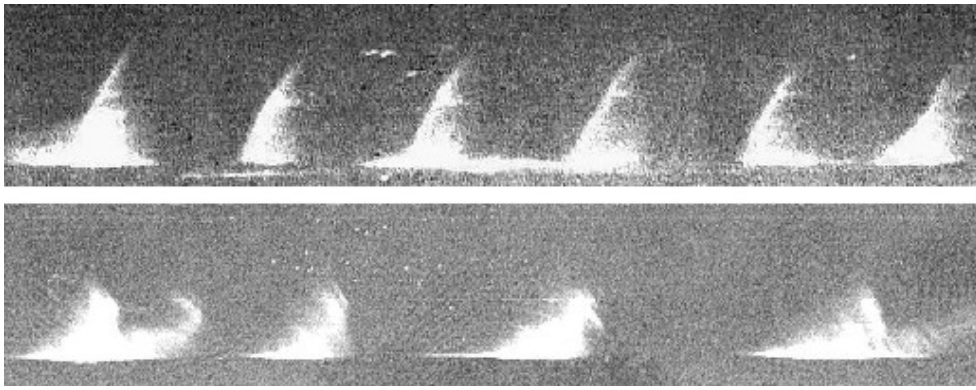


Fig.2.6. Schlieren patterns of a supersonic nitrogen flow ( $M = 4$ )

a) – without MHD interaction, b),c),d).- withc MHD interaction at various time instants from the discharge onset.



**Fig.2.7. Time scannings of the plasma radiation from a region near the conical body surface in supersonic nitrogen flow about the body at the opposite directions of the current through the discharge gap: above – the current is directed**



**Fig. 2.8. View of the model with the heat flux sensors.**



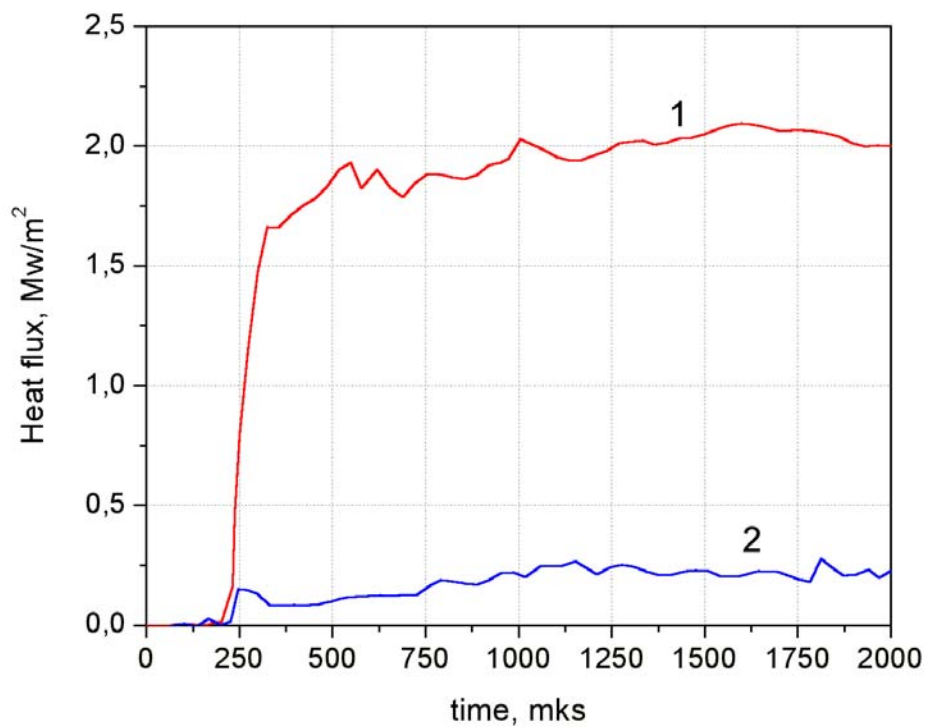


Fig.2.9. Heat flux toward the body surface from a discharge in quiescent air: 1- the ring electrode is connected to the negative terminal of the external voltage source, 2 - the ring electrode is connected to the positive terminal of the source.

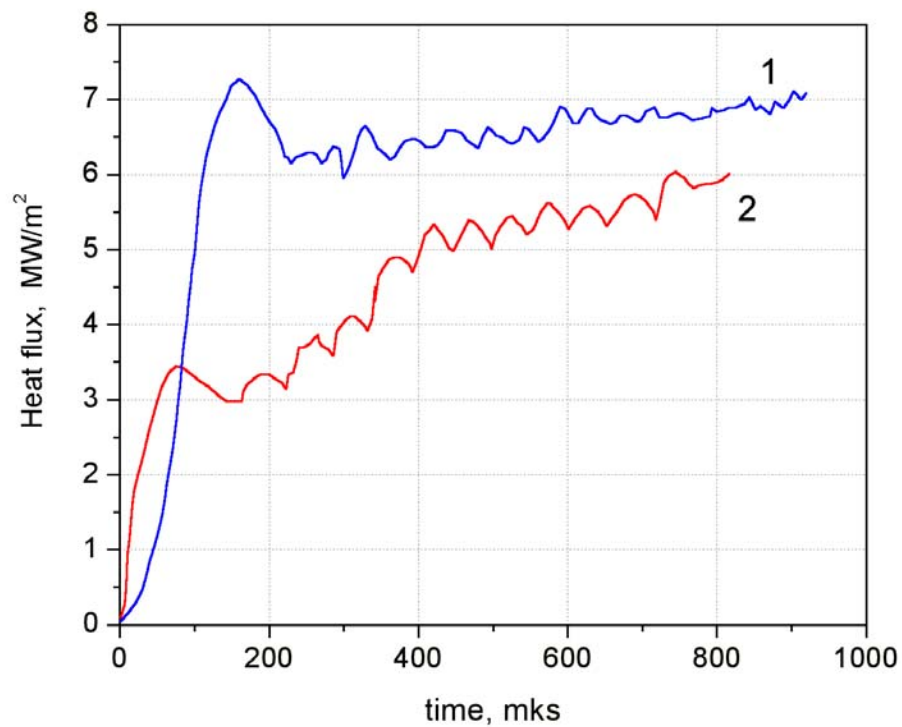


Fig. 2.10. Heat flux toward the body surface from a discharge in a supersonic nitrogen flow: 1- the ring electrode is connected to the negative terminal of the external voltage source, 2 - the ring electrode is connected to the positive terminal of the source.

### 3. NUMERICAL SIMULATION

The idea of the MHD flow control for improving aerodynamic characteristics of super- and hypersonic vehicles, in particular, for reduction of the drag and the wall heat flux is a result of successful investigations on the MHD control of internal plasma flows in ducts modeling supersonic intakes.

During the reporting year in the framework of the Project numerical investigations have been carried out of weakly ionized plasma flows about bodies in applied magnetic field. According to the Project Tasks simulation algorithms have been developed, supersonic plasma flow structure was investigated, and an attempt was made to estimate the feasibility of the MHD external flow control.

The Report contains the algorithm descriptions, results of the investigations, and the analysis of the main factors influencing on the flow structure.

#### 3.1. Introduction

In the framework of the project experimental and numerical investigations of supersonic lowtemperature lowionized xenon plasma flows about a body of revolution in the magnetic field were carried out.

The experimental setup is based on the Big Shock Tube (BST) of the Ioffe Institute. It consists of the supersonic nozzle attached to the shock tube and the body of revolution installed in the nozzle outlet (Fig. 3.1).

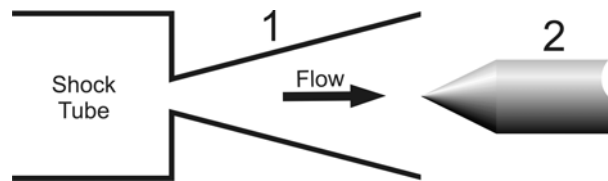


**Fig. 3.1.** The scheme of the experimental setup.  
1 - the nozzle, 2 - the body of revolution.

Xenon is characterized by greater recombination time in comparison with air, which allows us to separate the problems of gas ionization and MHD interaction. Preliminary ionized in the shock tube plasma is accelerating in the supersonic nozzle. The geometry of the nozzle provides the Mach number of the flow about  $M \sim 4.5$  when it meets the body. Magnetic field is generated by the magnetic inductor built in the body.

This part of the report is devoted to the numerical simulation of the flow under study. It contains the description of the mathematical model and numerical algorithm. The results of calculations of the flow for various magnetic field and electric current configurations are presented. The effects of viscosity and heat conductivity are analysed, as well as the influence of MHD interaction on the shock wave structure and heat fluxes to the body surface.

#### 3.2. Mathematical model

In our calculations we will use cylindrical frame of axes  $(z, r, \epsilon)$  instead of planar one  $(x, y, z)$ . The scheme of axes system is shown in Fig. 1, here,  $z$ -axis is coincided with body symmetry axis.



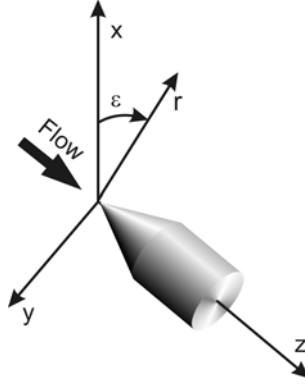


**Fig.3.2.** The scheme of the cylindrical frame of references used in the mathematical model.

The body of revolution interacts with uniform supersonic plasma flow. The incidence of the body is equal to zero so, the flow under study is axisymmetric. This means that  $\partial f / \partial \varepsilon = 0$  for any given function  $f$ .

#### *Plasma equations.*

Xenon plasma is supposed to consist of atoms (a), positive ions (i), and electrons (e). The analysis is conducted assuming plasma quasi-neutrality and two-temperature model. The magneto-gas dynamic interaction is taken into account within the framework of the MHD approach and neglecting the induced magnetic field. Validity of these assumptions follows from inequalities [1]:

$$l_D \ll L, \quad V_0 \ll c, \quad \tau_g = L/V_0 \gg \omega_p^{-1}, \quad \text{Re}_m \ll 1$$

which certainly hold for the flows under study. Here,  $l_D$  is the Debye length,  $L$  is the flow length scale,  $V_0$  is the flow velocity scale,  $c$  is the light speed,  $\omega_p$  is the plasma frequency,  $\text{Re}_m$  is the magnetic Reynolds number.

With above assumptions, non-equilibrium three-component and two-temperature plasma flows subjected to an applied magnetic field are governed by the following equations:

#### *total continuity equation*

$$\frac{\partial \rho}{\partial t} + \frac{1}{r} \frac{\partial (r \rho V_r)}{\partial r} + \frac{\partial \rho V_z}{\partial z} = 0$$

#### *continuity equation for the electrons*

$$\frac{\partial n_e}{\partial t} + \frac{1}{r} \frac{\partial (r n_e V_r)}{\partial r} + \frac{\partial n_e V_z}{\partial z} = \frac{1}{r} \frac{\partial}{\partial r} \left[ r \frac{\mu}{Sc} \frac{\partial}{\partial r} \left( \frac{n_e}{\rho} \right) \right] + \frac{\partial}{\partial z} \left[ \frac{\mu}{Sc} \frac{\partial}{\partial z} \left( \frac{n_e}{\rho} \right) \right] + n_e$$

#### *axial projections of total momentum balance equations*

$$\frac{\partial \rho V_r}{\partial t} + \frac{1}{r} \frac{\partial [r(\rho V_r^2 + p)]}{\partial r} + \frac{\partial \rho V_r V_z}{\partial z} - \frac{1}{r} \rho V_\varepsilon^2 - \frac{1}{r} p = \frac{1}{\text{Re}} \frac{1}{r} \frac{\partial}{\partial r} \left[ r \mu \left( \frac{4}{3} \frac{\partial V_r}{\partial r} - \frac{2}{3} \frac{\partial V_z}{\partial z} - \frac{2}{3} \frac{1}{r} V_r \right) \right] +$$

$$\frac{1}{\text{Re}} \frac{\partial}{\partial z} \left[ \mu \left( \frac{\partial V_r}{\partial z} + \frac{\partial V_z}{\partial r} \right) \right] - \frac{2\mu}{\text{Re}} \frac{1}{r^2} V_r + j_\varepsilon B_z - j_z B_\varepsilon$$

$$\frac{\partial \rho V_z}{\partial t} + \frac{1}{r} \frac{\partial \rho V_z V_r}{\partial r} + \frac{\partial (\rho V_z^2 + p)}{\partial z} = \frac{1}{\text{Re}} \frac{1}{r} \frac{\partial}{\partial r} \left[ r \mu \left( \frac{\partial V_r}{\partial z} + \frac{\partial V_z}{\partial r} \right) \right] +$$

$$\frac{1}{\text{Re}} \frac{\partial}{\partial z} \left[ \mu \left( -\frac{2}{3} \frac{\partial V_r}{\partial r} + \frac{4}{3} \frac{\partial V_z}{\partial z} - \frac{2}{3} \frac{1}{r} V_r \right) \right] + j_r B_\varepsilon - j_\varepsilon B_r$$

$$\frac{\partial \rho V_\varepsilon}{\partial t} + \frac{1}{r} \frac{\partial \rho V_\varepsilon V_r}{\partial r} + \frac{\partial \rho V_\varepsilon V_z}{\partial z} + \frac{1}{r} \rho V_\varepsilon V_r = \frac{1}{\text{Re}} \frac{1}{r} \frac{\partial}{\partial r} \left[ r \mu \left( \frac{\partial V_\varepsilon}{\partial r} - \frac{1}{r} V_\varepsilon \right) \right] + \frac{1}{\text{Re}} \frac{\partial}{\partial z} \left[ \mu \frac{\partial V_\varepsilon}{\partial z} \right] +$$

$$\frac{1}{\text{Re}} \frac{1}{r} \mu \left[ \frac{\partial V_\varepsilon}{\partial r} - \frac{1}{r} V_\varepsilon \right] + j_z B_r - j_r B_z$$

*total energy balance equation*

$$\frac{\partial E}{\partial t} + \frac{1}{r} \frac{\partial [r V_r (E + p)]}{\partial r} + \frac{\partial [r V_z (E + p)]}{\partial z} =$$

$$\frac{1}{\text{Re}} \frac{1}{r} \frac{\partial}{\partial r} \left\{ r \mu \left[ V_r \left( \frac{4}{3} \frac{\partial V_r}{\partial r} - \frac{2}{3} \frac{\partial V_z}{\partial z} - \frac{2}{3} \frac{1}{r} V_r \right) + V_z \left( \frac{\partial V_r}{\partial z} + \frac{\partial V_z}{\partial r} \right) + V_\varepsilon \left( \frac{\partial V_\varepsilon}{\partial r} - \frac{1}{r} V_\varepsilon \right) \right] \right\} +$$

$$\frac{1}{\text{Re}} \frac{\partial}{\partial z} \left\{ \mu \left[ V_r \left( \frac{\partial V_r}{\partial z} + \frac{\partial V_z}{\partial r} \right) + V_z \left( -\frac{2}{3} \frac{\partial V_r}{\partial r} + \frac{4}{3} \frac{\partial V_z}{\partial z} - \frac{2}{3} \frac{1}{r} V_r \right) + V_\varepsilon \frac{\partial V_\varepsilon}{\partial z} \right] \right\} +$$

$$\frac{1}{\text{Re}} \frac{1}{r} \mu \left[ -2 \frac{1}{r} V_r^2 + V_\varepsilon \left( \frac{\partial V_\varepsilon}{\partial r} - \frac{1}{r} V_\varepsilon \right) \right] - \nabla \bar{q} - \nabla \bar{q}_e + \vec{j} \cdot \vec{E} - \dot{n}_e \varepsilon_{ion}$$

*energy balance equation for the electrons*

$$\frac{\partial}{\partial t} \left( \frac{3}{2} p_e \right) + \frac{1}{r} \frac{\partial}{\partial r} \left( r V_r \frac{5}{2} p_e \right) + \frac{\partial}{\partial z} \left( V_z \frac{5}{2} p_e \right) = -\nabla \bar{q}_e + \vec{j} \cdot (\vec{E} + \vec{V} \times \vec{B}) + \vec{V} \cdot \nabla p_e - \dot{n}_e \varepsilon_{ion} +$$

$$3 \frac{m_e}{m} k n_e (v_{ei} + v_{ea}) (T - T_e)$$

where  $r$ ,  $z$ ,  $\varepsilon$  are the radial, longitudinal and angular coordinates respectively or mean the radial, longitudinal and angular vector components when been used as a subscript;  $t$  is the time;  $p = p_a + p_i + p_e$  is the plasma pressure;  $p_\alpha$  ( $\alpha = a, i, e$ ) is the partial pressure of  $\alpha$ -component;  $\rho = \rho_a + \rho_i + \rho_e$  is density;  $n_\alpha$  is the number density of  $\alpha$ -component ( $\alpha = a, i, e$ );  $\vec{V}$  ( $V_r, V_z, V_\varepsilon$ ) is the plasma velocity;  $T, T_e$  are the temperatures of heavy particles (ions and atoms) and electrons;  $m, m_e$  are the mass of heavy particle and electron;  $k$  is the Boltzmann constant;  $\dot{n}_e$  is the number rate of electron production per unit volume;  $v_{ea}, v_{ei}$  are the collision frequencies for electrons with ions and atoms;  $\varepsilon_{ion}$  is the ionization energy per atom;  $\mu$  is the gas viscosity;  $\text{Sc}$  is the Schmidt number;  $\text{Re}$  is the Reynolds number;  $\vec{B}$  ( $B_r, B_z, B_\varepsilon$ ) is the magnetic field induction;  $\vec{E}$  ( $E_r, E_z, E_\varepsilon$ ) is the electric field strength;  $\vec{j}$  ( $j_r, j_z, j_\varepsilon$ ) is the electric current;  $E$  is the gas total energy per unit volume;  $\bar{q}_e, \bar{q}$  are the heat fluxes due to the electrons and the heavy particles:

$$E = \frac{3}{2} p + \frac{\rho V^2}{2} \qquad \bar{q} = \lambda \nabla T = \mu \nabla T / \text{Re Pr}$$

where  $\lambda$  is the heat conductivity,  $\text{Pr}$  is the Prandtl number. The heat flux due to the electrons is evaluated following elementary theory in which [1]:

$$\bar{q}_e = -\lambda_{\parallel} \cdot (\nabla_{\parallel} T_e) - \lambda_{\perp} \cdot (\nabla_{\perp} T_e) - \lambda_H \cdot \bar{b} \times (\nabla T_e) + \psi_{\parallel}(\bar{j}_{\parallel}) + \psi_{\perp}(\bar{j}_{\perp}) + \psi_H(\bar{b} \times \bar{j})$$

$$\lambda_{\parallel} = \frac{n_e k^2 T_e}{m_e (\nu_{ei} + \nu_{ea})} \quad \lambda_{\perp} = \frac{\lambda_{\parallel}}{1 + \beta_e} \quad \lambda_H = \frac{\lambda_{\parallel} \beta_e}{1 + \beta_e}$$

$$\psi_{\parallel} = \frac{7}{2} \frac{k T_e}{e} \quad \psi_{\perp} = \frac{\psi_{\parallel}}{1 + \beta_e} \quad \psi_H = \frac{\psi_{\parallel} \beta_e}{1 + \beta_e}$$

where  $\bar{b} = \bar{B}/|\bar{B}|$  is the unit vector of magnetic induction,  $\beta_e$  is the Hall parameter for electrons, indices  $\parallel, \perp, H$  correspond to parallel, perpendicular and Hall components of vector.

The electron production rate  $n_e$  is calculated following the theory of non-equilibrium ionization in a low-temperature rare gas plasma developed by Biberman et al. [2]. The main processes which determine the charged particle concentrations within the range of conditions considered are ionization by electron impact and three-particle recombination. The recombination rate constant for xenon plasma calculated following the above theory was presented in our previous report [3] as function of the electron temperature. We use the recombination rate constants from these graphs. The ionization rate constant is found through the equilibrium constant [1]. The expressions of the collision frequencies for electrons with heavy particles  $\nu_{ea}, \nu_{ei}$  can be found in [1,3,4].

*Electric field potential equation.*

Electric current density is found from the generalized Ohm's law:

$$\bar{j} = \sigma_{\parallel} \bar{E}'' + \sigma_{\perp} \bar{E}_{\perp}'' + \sigma_H \bar{b} \times \bar{E}'' = \bar{\sigma} \cdot \{E_r'', E_z'', E_{\varepsilon}''\}^T$$

$$\bar{E}'' = \bar{E} + \bar{V} \times \bar{B} + \frac{\nabla p_e}{en_e}$$

where  $E''$  is total force affecting the electron,  $\sigma$  is the tensor of conductivity

$$\bar{\sigma} = \begin{bmatrix} \sigma_{rr} & \sigma_{rz} & \sigma_{r\varepsilon} \\ \sigma_{zr} & \sigma_{zz} & \sigma_{z\varepsilon} \\ \sigma_{\varepsilon r} & \sigma_{\varepsilon z} & \sigma_{\varepsilon\varepsilon} \end{bmatrix} = \sigma_{\perp} \cdot \begin{bmatrix} 1 & 0 & 0 \\ 0 & 1 & 0 \\ 0 & 0 & 1 \end{bmatrix} + \sigma_H \cdot \begin{bmatrix} 0 & b_{\varepsilon} & -b_z \\ -b_{\varepsilon} & 0 & b_r \\ b_z & -b_r & 0 \end{bmatrix} + (\sigma_{\parallel} - \sigma_{\perp}) \cdot \begin{bmatrix} b_r^2 & b_r b_z & b_r b_{\varepsilon} \\ b_z b_r & b_z^2 & b_z b_{\varepsilon} \\ b_{\varepsilon} b_r & b_{\varepsilon} b_z & b_{\varepsilon}^2 \end{bmatrix},$$

$$\sigma_{\parallel} = \frac{n_e e^2}{m_e (\nu_{ei} + \nu_{ea})} \quad \sigma_{\perp} = \frac{\sigma_{\parallel}}{1 + \beta_e} \quad \sigma_H = \frac{\sigma_{\parallel} \beta_e}{1 + \beta_e}$$

$e$  is the electron charge.

Assuming the magnetic field to be stationary the Faraday law has a form  $\nabla \times \bar{E} = 0$ , which implies  $\bar{E} = -\nabla \phi$ , where  $\phi$  is the electric field potential. The flow is axisymmetric which means that  $\partial \phi / \partial \varepsilon = 0$  and, consequently,  $E_{\varepsilon} = 0$ . The equation for the electric field potential  $\phi$  arises from the relation  $\nabla \bar{j} = 0$  and uses the expression of electric current  $\bar{j}$  from the generalized Ohm's law, which gives:

$$\nabla \bar{j} = \nabla \cdot \left\{ \bar{\sigma} \left( -\nabla \phi + \bar{V} \times \bar{B} + \frac{\nabla p_e}{en_e} \right) \right\} = 0,$$

*Boundary conditions.*

In the inflow boundary all plasma parameters are prescribed. On the body walls, the non slip conditions are imposed. As it was shown in the BST experiments [5], the temperature of the walls is constant during the BST operation time, so, heat fluxes on the body surface are calculated assuming the constant wall temperature. On the outflow boundary where the flow is supersonic boundary

conditions of type  $\partial f / \partial n = 0$  are used where  $n$  is normal to the boundary vector. For potential equation the electric current impermeability boundary conditions are used in all boundaries.

### 3.3. Numerical method

For the solution of the above equations we used the finite volume methods. It means that the equations are integrated via the computational mesh cells volume after this volumetric integrals from the vectors divergence is substituted by integrals via cell surface according to the Gauss-Ostrogradskii theorem. These methods are conservative and allow “shock-capturing” calculations.

The solution is looking in the nodes of structured computational mesh formed by the intersection of two sets of mesh lines, so, the number of computational cell is defined by two indices  $(i,j)$  correspond to the mesh lines numbers.

*Method for the solving electric field potential equation.*

For the solution of the above equations we used the finite volume methods. It means that the equations are integrated via the computational mesh cells volume after this volumetric integrals from the vectors divergence is substituted by integrals via cell surface according to the Gauss-Ostrogradskii theorem. These methods are conservative and allow “shock-capturing” calculations.

The solution is looking in the nodes of structured computational mesh formed by the intersection of two sets of mesh lines, so, the number of computational cell is defined by two indices  $(i,j)$  correspond to the mesh lines numbers.

The integral form of the potential equation is the following:

$$\int_{V_{i,j}} \nabla \vec{j} \cdot d\vec{V} = \int_{S_{i,j}} (\vec{j} \cdot \vec{N}) dS = \int_{S_{i,j}} \vec{N} \cdot \left[ \vec{\sigma} \left( -\nabla \varphi + \vec{V} \times \vec{B} + \frac{\nabla p_e}{en_e} \right) \right] dS$$

where  $S$  is the cell surface,  $V$  is the cell volume;  $\vec{N}(N_r, N_z)$  is the unit vector normal to the cell boundary.

For determination of integrand on the cell boundaries the linear approximation in the triangle elements was used [6]. Fig. 3.3. shows the scheme of this approximation. In the figure point  $(i,j)$ ,  $(i+1,j)$ ,  $(i,j+1)$ ,  $(i+1,j+1)$  are the mesh nodes, points  $(i+1/2,j)$ ,  $(i,j+1/2)$  are the centers of the corresponding mesh lines segments connecting neighbouring mesh nodes. For example, on the  $(i+1/2,j)-(i+1/2,j+1/2)$  segment any function or its derivatives are found via the approximation inside  $[(i,j),(i+1/2,j),(i,j+1/2)]$  triangle.

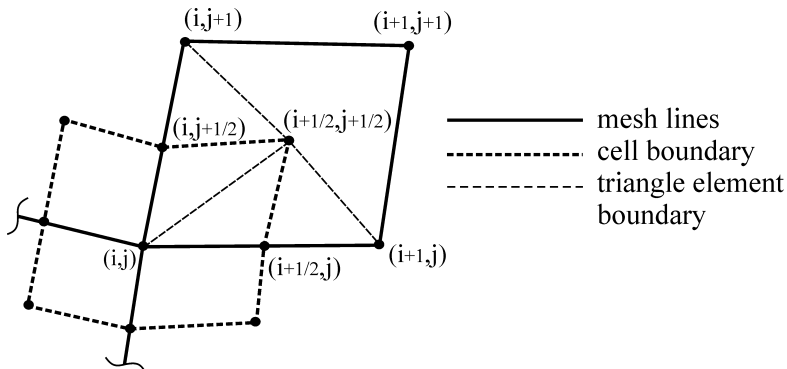


**Fig. 3.3.** Computational cell scheme. The cell volume and triangle elements used for the approximation are shown.

Discretisation of the integral form of the potential equation on the computational mesh gives the system of algebraic equations for the potential magnitudes in the mesh nodes with block-threediagonal matrix of the coefficients. This system is solved by the block Thomas algorithm.

### Method for the solving plasma dynamic equation.

The vector form of the plasma equations is the following:

$$\frac{\partial U}{\partial t} + \frac{1}{r} \frac{\partial r F_r}{\partial r} + \frac{\partial F_z}{\partial z} + \frac{1}{r} F' = \frac{1}{r} \frac{\partial r G_r}{\partial r} + \frac{\partial G_z}{\partial z} + \frac{1}{r} G' + Q_m + Q_n$$

where  $U$  is the vector-column of flow parameters;  $F_r$ ,  $F_z$ ,  $F'$  are the vector-columns of convective flows, vector-columns  $G_r$ ,  $G_z$ ,  $G'$  contain viscous and diffusive flows and heat conductivity, vector-column  $Q_m$  contains electro-magnetic terms of the equations,  $Q_n$  contains the terms concerned with non-equilibrium kinetic processes of ionization and electron-heavy particle exchange.

Assuming gas dynamic variables to be constant within a computational cell and making use of the integral formulae of vectorial analysis, one can write out finite-volume notation of plasma equation for a computational cell:

$$\left( \frac{dU}{dt} \right)_{i,j} = \frac{1}{Vol_{i,j}} \left\{ \int_{S_{i,j}} r(-F_r N_r - F_z N_z + G_r N_r + G_z N_z) \cdot dS + F'_{i,j} V_{i,j} + G'_{i,j} V_{i,j} \right\} + (Q_m)_{i,j} + (Q_n)_{i,j}$$

where  $Vol_{i,j} = \int_{V_{i,j}} r \cdot dV$ .

With known expression inside the braces and known  $(Q_m)_{i,j}$  this equation represents the set of ordinary differential equations which is solved by the implicit two-layer method.

For evaluation of the convective flows  $F_r$ ,  $F_z$ , the Godunov-type high resolution TVD scheme was applied [7,8,9]. In this scheme, flows on the edge between the cells are found from the solution of the Riemann problem between the magnitudes of gasdynamics functions approximated from the cell centers:

$$\begin{aligned} F_{i+1/2,j} &= Riemman(U_{i+1/2,j}^L, U_{i+1/2,j}^R) \\ U_{i+1/2,j}^L &= U_{i,j} + 1/2 \cdot l_{i+1/2,j} \cdot (\partial U / \partial i)_{i,j} \\ U_{i+1/2,j}^R &= U_{i+1,j} - 1/2 \cdot l_{i+1/2,j} \cdot (\partial U / \partial i)_{i+1,j} \end{aligned}$$

where  $l_{i+1/2,j}$  is the length of the segment connecting  $(i,j)$  and  $(i+1,j)$  nodes (see Fig. 3.3).

The special limiter function is used when the gasdynamics function gradients are calculated, which provides the monotonicity in the regions of non-smooth functions behavior.

$$\left( \frac{\partial U}{\partial i} \right)_{i,j} = limiter \left( \frac{U_{i,j} - U_{i-1,j}}{l_{i-1/2,j}}, \frac{U_{i+1,j} - U_{i,j}}{l_{i+1/2,j}} \right)$$

Integrals from  $G_r$ ,  $G_z$ , vectors are approximated in the same manner as the terms in the potential equation. Vector  $Q_m$  is evaluated after the solution of the electric potential equation.

The above computational procedure is second-order accurate with respect to both spatial coordinates in the flow regions with smooth function behavior.

### 3.4. The results of calculations.

Configuration of the flow domain allows us to separate the computations into two stages. First, the flow field is calculated inside the nozzle. After this, on the second stage, the calculations are made for the flow about the body.

In Fig. 3.4. the distribution of the Mach number in the nozzle of the experimental setup is presented. The calculation gives the following flow parameters in the nozzle outlet:

$$n = 4.34 \times 10^{23} \text{ 1/m}^3, \quad \alpha = 4.157 \times 10^{-4}, \quad T = 1729 \text{ K},$$

$$T_e = 3637 \text{ K}, \quad V_z = 1966 \text{ m/s}, \quad M = 4.6.$$

where  $M$  is Mach number of the flow. These values are used as inflow boundary conditions on the second stage of calculations.

Fig. 3.5 demonstrates the comparison of calculated and experimental shadowgraphs of the flow about the body without MHD interaction. The body of revolution represents the cone with  $30^\circ$  half angle put together with the cylinder. The Reynolds number of the flow is  $Re \sim 10^4$ . The attached to the cone shock wave is well seen in the figure. Fig. 3.6 shows the distribution of the ionization degree, heavy particle and electron temperatures.

In Fig. 3.7. the variation of the heavy particle and electron temperatures is shown when plasma is coming through the shock wave. It is seen that the electron temperature jump in the shock wave is smaller than the jump of heavy particle temperature. Due to intensive electrons heat conductivity, the heating of electrons gas take place in the front of the shock wave. These facts are confirmed by the theoretical investigations [10]. In Fig. 3.7. the region 2 means the shock wave and region 1 means the area of electrons heating in front of the shock. When approaching the shock wave, the considerable separation of electrons and heavy particle temperatures occurs. The electron temperature jump in the shock wave is  $\Delta T_e = (T_e)_1 / (T_e)_0 \sim 1.72$ , the heavy particle temperature jump is  $\Delta T = T_1 / T_0 \sim 3.32$ , where index 0 indicate the parameters before and index 1 indicates the parameters after the shock wave. Due to increasing of the density and temperature after the shock wave the intensive heat exchange between heavy and electron components takes place. In Fig. 3.7. this region is denoted by 3.

In Fig. 3.8. the typical profiles of the flow velocity ( $U$ ), heavy particle and electron temperatures ( $T$ ,  $T_e$ ) and plasma electric conductivity ( $\sigma$ ) are presented. In the calculations the body wall was considered to have a lower temperature than the flow temperature, as a result, the low conductivity layer is attached to the wall.

Magnetic field is generated by the set of turns inside the body. Three configurations of magnetic coils were considered. In the first configuration, the coil is situated after the cone its diameter is the same as the diameter of the cylindrical part of the body (Fig. 3.9.1). In the second configuration, the turns of the coil are located along the lateral face of the cone (Fig. 3.9.2). In third case, the coil has a small diameter and is positioned near the cone nose (Fig. 3.9.3). The distributions of magnetic field induction are shown in Fig. 3.9. Additionally to the magnetic field in the case of the first configuration of the magnetic coil, the external electric field was applied (configuration 4). In this case, electric current flows through the electrodes on the lateral face of the body. First electrode is situated near the point of cone and cylinder coupling, the second is situated in the nose of the cone (Fig. 3.10)

The presence of the magnetic field leads to appearance of the electric current. It results in heating of the electron component due to Joule heat release and modification of the flow velocity due to ponderomotive forces, azimuthal components of the electric current and flow velocity also appear. Additional flow structure modification is caused by the heat transfer from "hot" electrons to heavy particle.

A set of calculations of inviscid flows was carried out for investigation of the MHD interaction influence on the shock wave structure. Figs. 3.11-3.13 shows the distributions of the flow parameters for considered magnetic coils configurations. The electric current through the coil turns is equal to 1 kA.

It is seen that the increase of electron temperature take place in the vicinity of the magnetic coil turns, especially, downstream from the coil. Shifting of the coil position allows to displace the electron heating area to the region upstream from the shock wave. The considerable influence of the magnetic field on shock wave structure is not visible.

The flow with both external magnetic and electric fields is illustrated by Figs. 3.14-3.15. In this case MHD interaction has the most considerable influence on the flow. On the shadowgraph of the flow the variation of the shock position is visible. Moreover, in this calculation the maximal values of azimuthal projections of the plasma velocity and electric current were obtained.

The shadowgraphs of the viscous flows in the magnetic field are presented in Figs. 3.16.-3.17. The position of the magnetic coil corresponds to the first configuration (Fig. 3.9.1.). In the case from the

Fig. 3.18 the electric current through the electrodes was switched on (configuration 4). Analysing this pictures, the conclusion can be made that MHD interaction leads to the slight thickening of the boundary layer. This fact can be explain by the heating of the flow.

The distributions of the body surface heat fluxes due to heavy particle  $q_w$  and electrons  $(q_w)_e$  are illustrated by Figs. 3.18. - 3.19. The primary wall heat flux is generated on the lateral surface of the cone its maximum locates on the cone nose. On the cylindrical part of the body the heat flux is generated by the plasma crossed through the rarefaction waves fan, so, its magnitude is much smaller. The general contribution to the heat fluxes is made by heavy component.

The comparisons of the various flow regimes in Figs. 3.18. - 3.19. show that after switching on of the magnetic field heat flux varies mainly due to electron component, the heat flux due to heavy particles varies when the electric current is switched on.

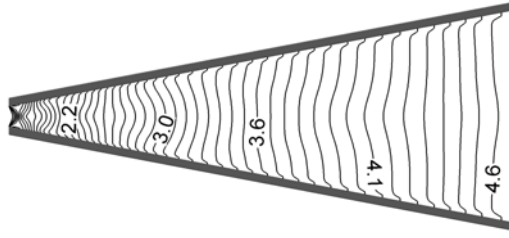


**Fig. 3.4.** Mach number distribution in the nozzle of the experimental setup.

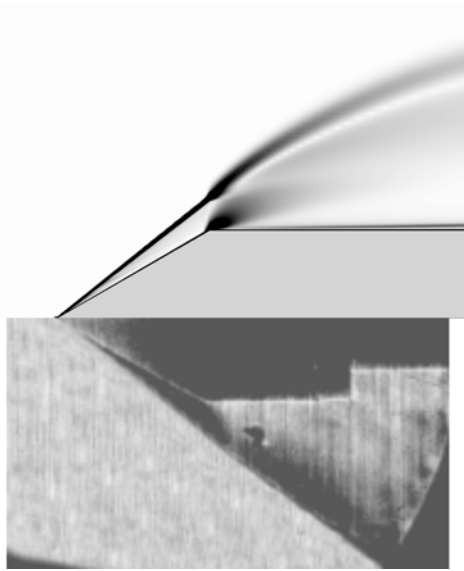


**Fig. 3.5.** The comparison of the calculated (top) and experimental (bottom) shadowgraphs of the flow about the body without MHD interaction.

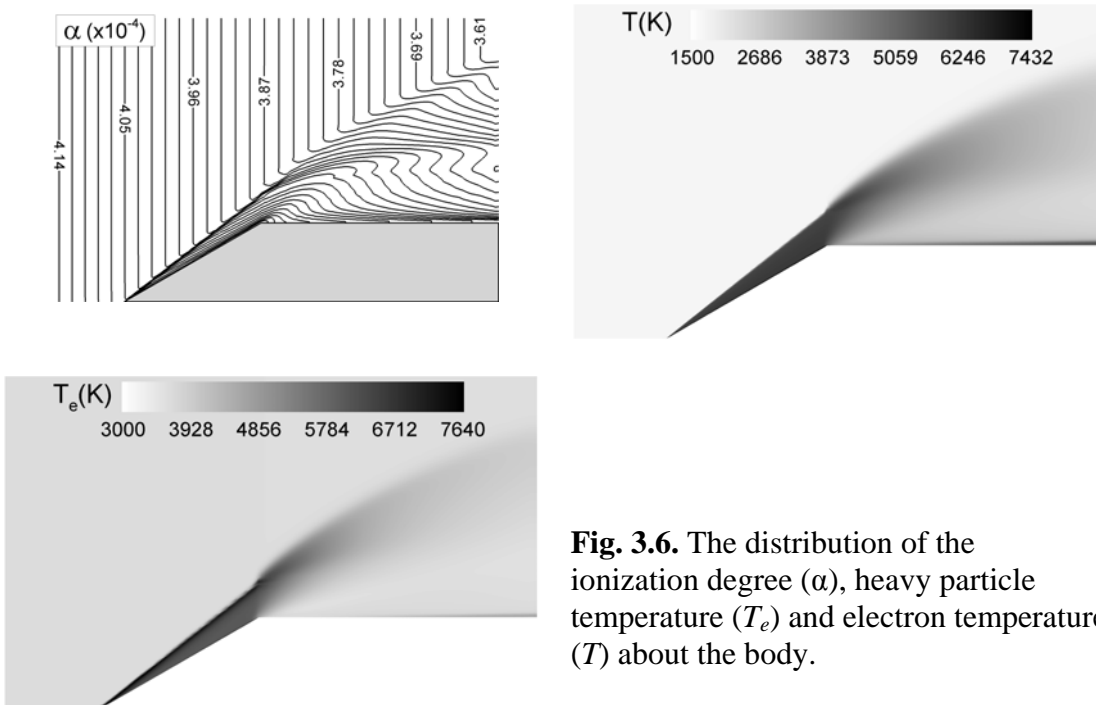


**Fig. 3.6.** The distribution of the ionization degree ( $\alpha$ ), heavy particle temperature ( $T_e$ ) and electron temperature ( $T$ ) about the body.



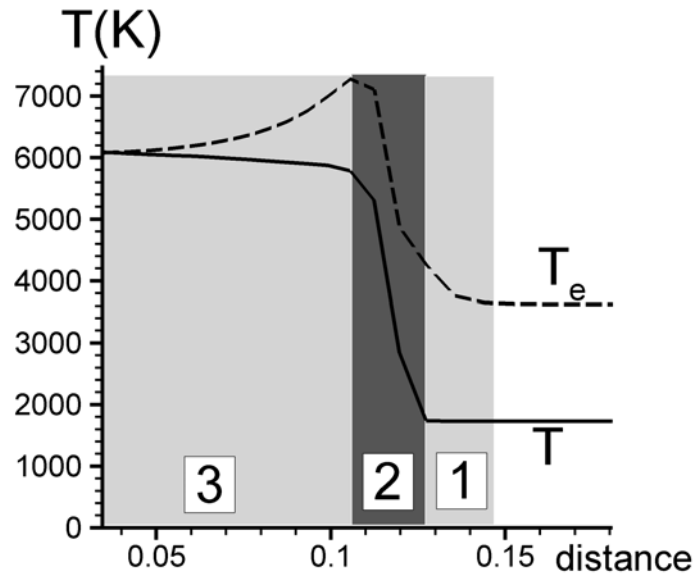


**Fig. 3.7.** Variation of the electron and heavy particle temperatures while coming through the shock wave. 1 is the region of electrons heating in front of the shock due to electrons heatconducitivity; 2 is shock wave; 3 – is the region of electron temperature relaxation.

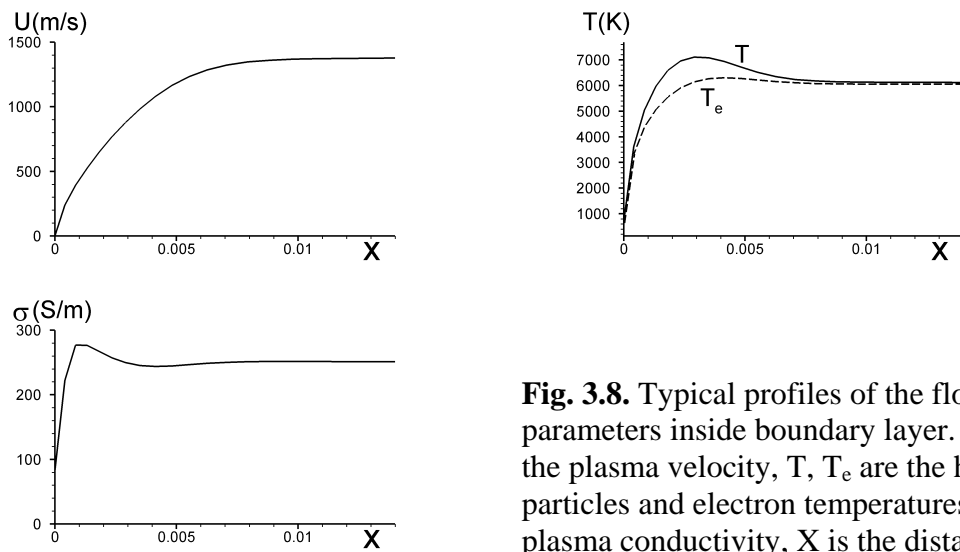


**Fig. 3.8.** Typical profiles of the flow parameters inside boundary layer.  $U$  is the plasma velocity,  $T$ ,  $T_e$  are the heavy particles and electron temperatures,  $\sigma$  is plasma conductivity,  $X$  is the distance from the wall..

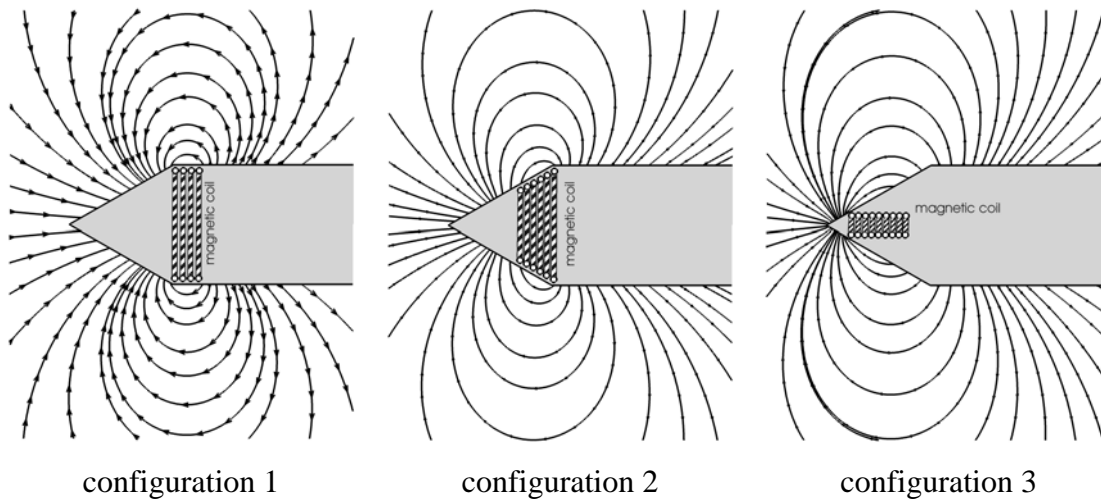


**Fig. 3.9.** Configurations of the magnetic coils and corresponding magnetic field streamlines.

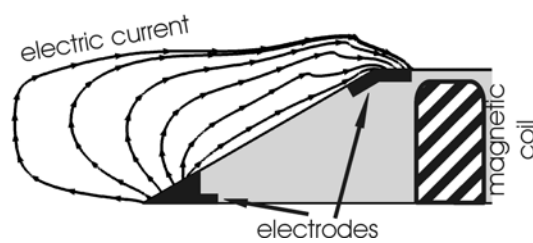


**Fig. 3.10.** The electrode system of the body

### Configuration 1

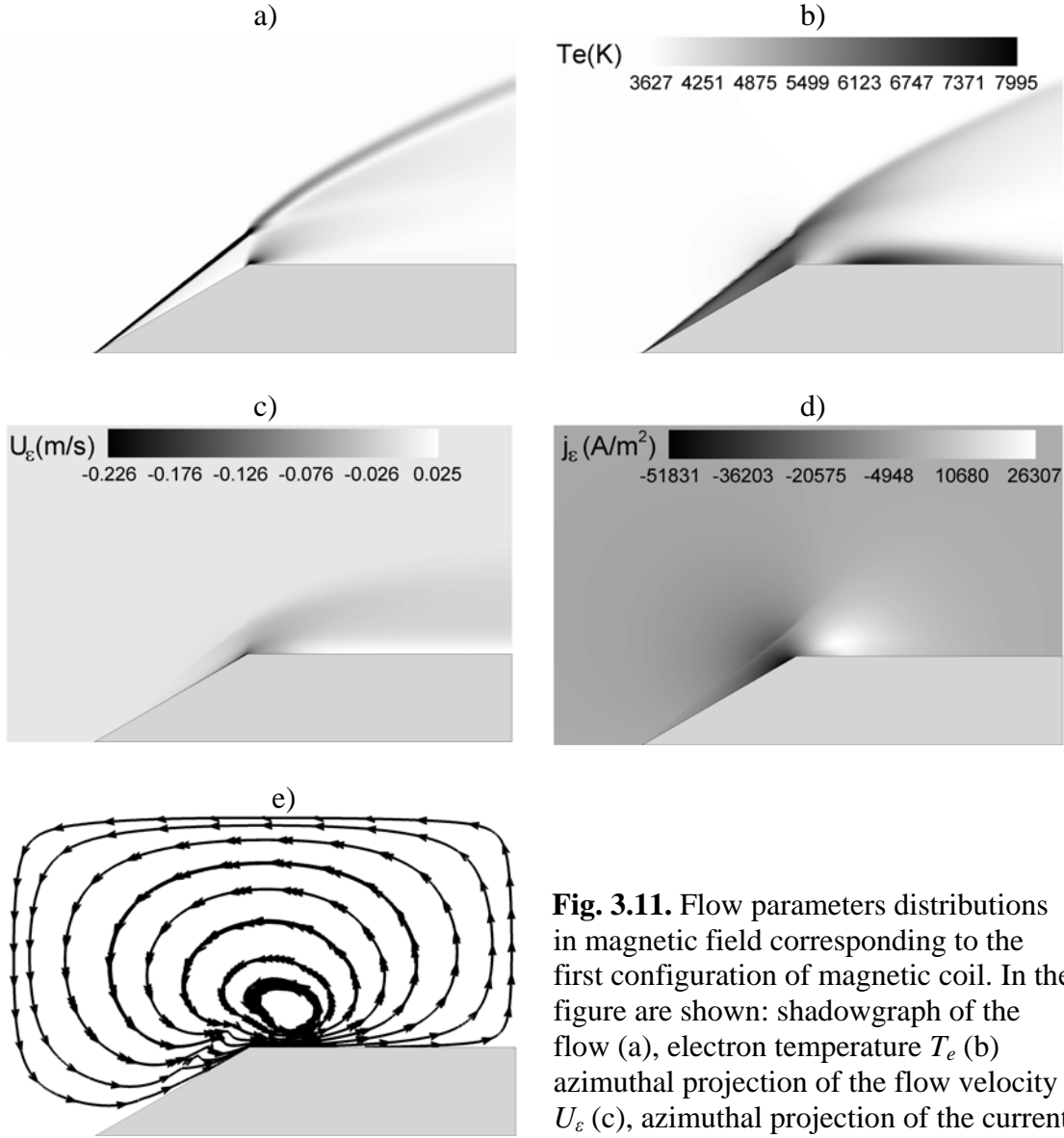


**Fig. 3.11.** Flow parameters distributions in magnetic field corresponding to the first configuration of magnetic coil. In the figure are shown: shadowgraph of the flow (a), electron temperature  $T_e$  (b) azimuthal projection of the flow velocity  $U_e$  (c), azimuthal projection of the current  $j_e$  (d) and electric current streamlines (e).

## Configuration 2

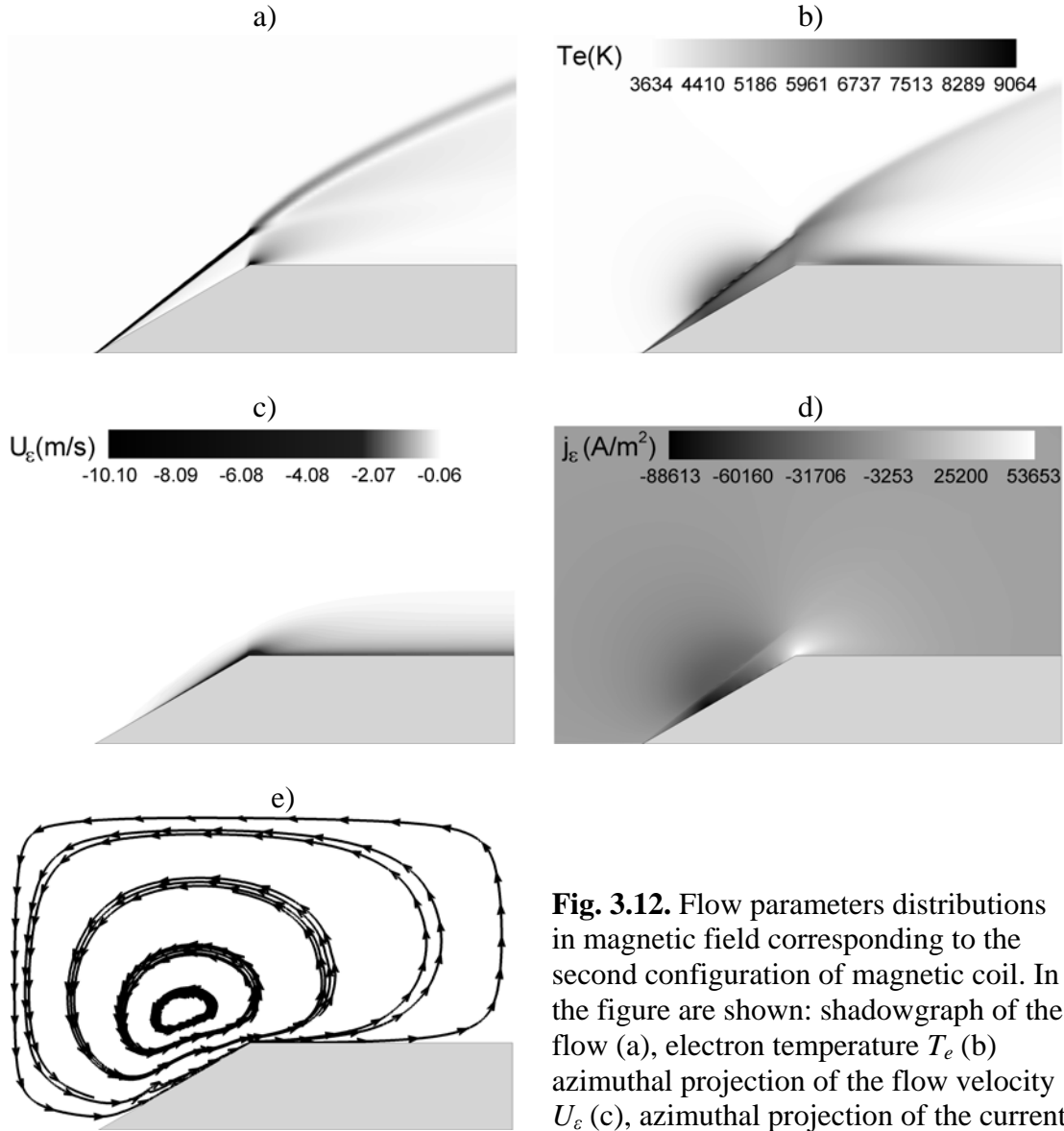


**Fig. 3.12.** Flow parameters distributions in magnetic field corresponding to the second configuration of magnetic coil. In the figure are shown: shadowgraph of the flow (a), electron temperature  $T_e$  (b) azimuthal projection of the flow velocity  $U_e$  (c), azimuthal projection of the current  $j_\epsilon$  (d) and electric current streamlines (e).

### Configuration 3

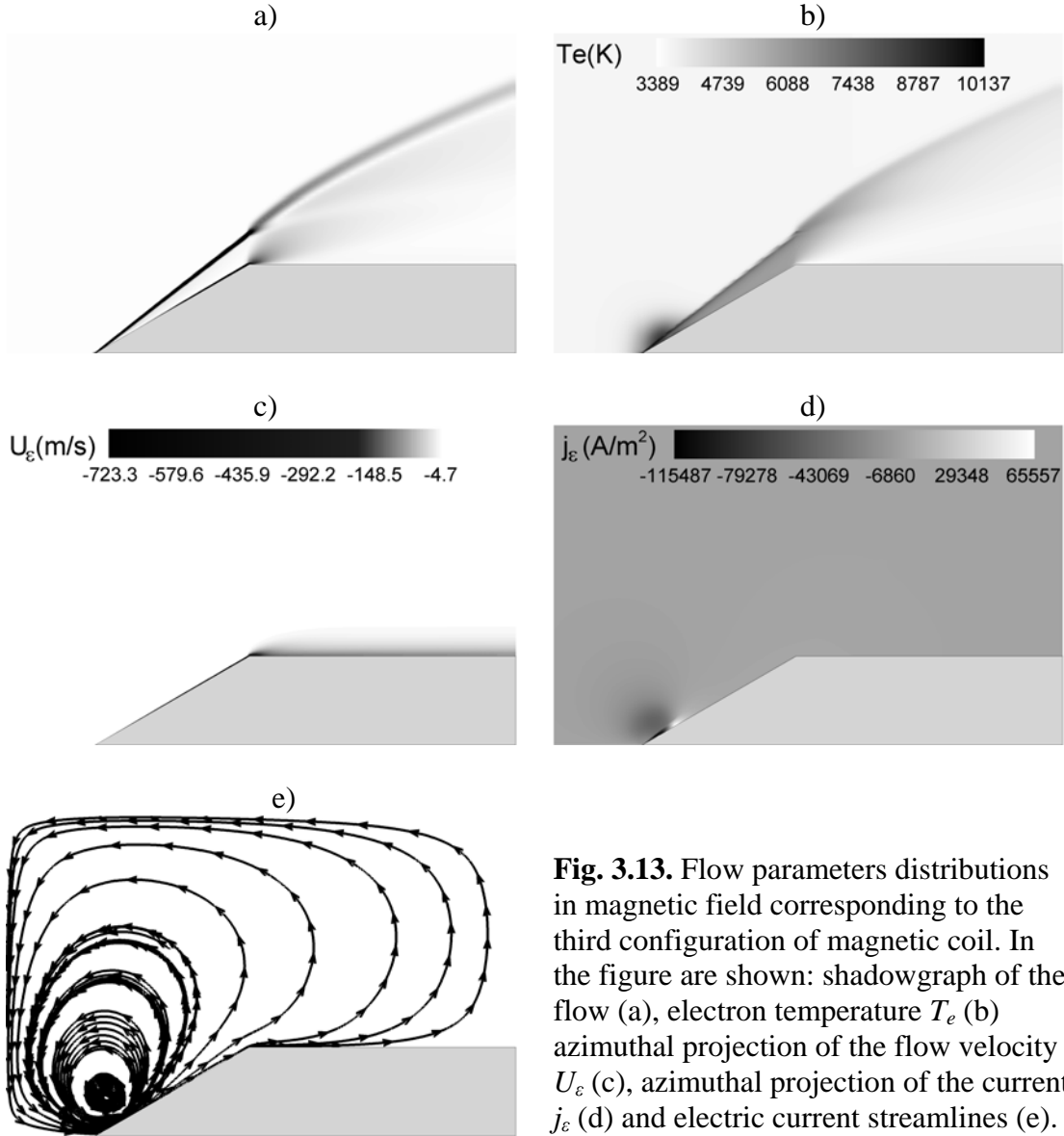


**Fig. 3.13.** Flow parameters distributions in magnetic field corresponding to the third configuration of magnetic coil. In the figure are shown: shadowgraph of the flow (a), electron temperature  $T_e$  (b) azimuthal projection of the flow velocity  $U_\epsilon$  (c), azimuthal projection of the current  $j_\epsilon$  (d) and electric current streamlines (e).

### Configuration 4

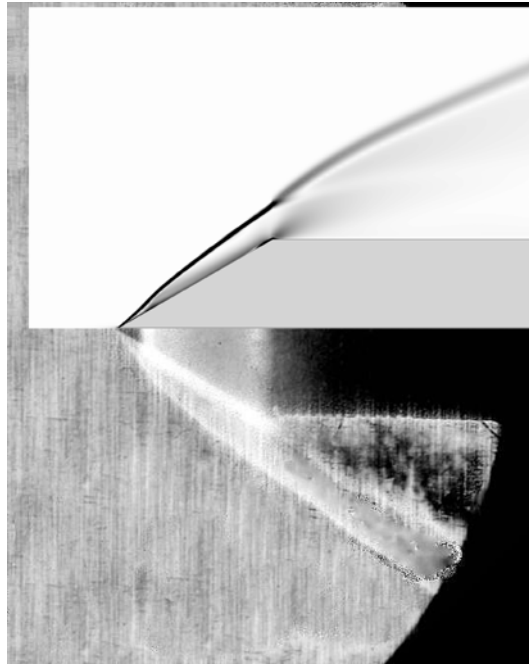


**Fig. 3.14.** Comparison of calculated (top) and experimental shadowgraphs of the flow under the external magnetic field with electric current through the electrodes (configuration 4).

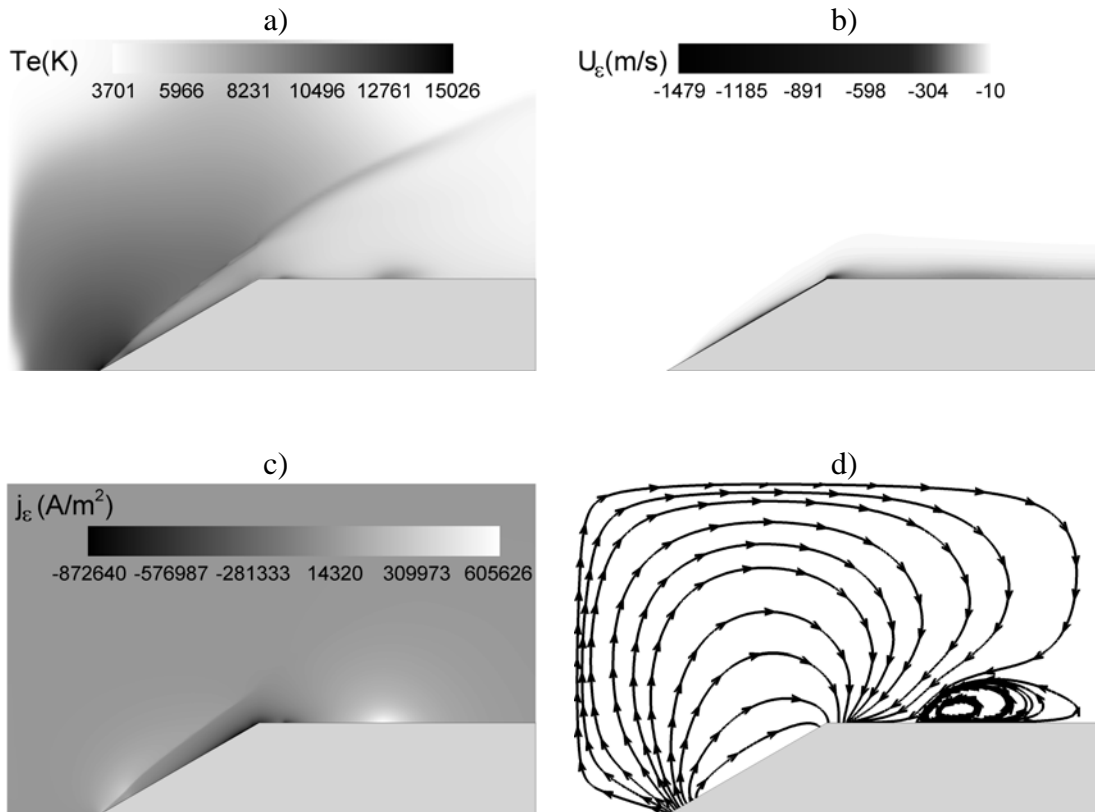


**Fig. 3.15** Distributions of the flow parameters in magnetic field with electric current through the electrodes. In the figure are shown: electron temperature  $T_e$  (a), azimuthal projection of the flow velocity  $U_\epsilon$  (b), azimuthal projection of the current  $j_\epsilon$  (c) and electric current streamlines (d).

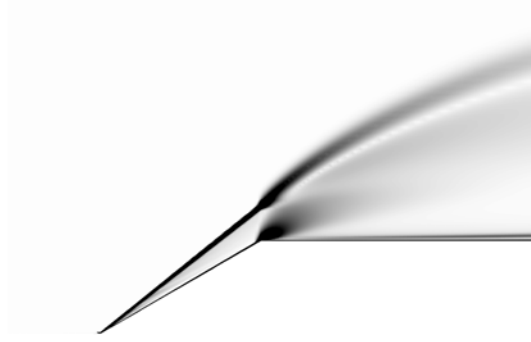


**Fig. 3.16.** The shadowgraph of the viscous flow in the magnetic field (configuration 1)



**Fig. 3.17.** The shadowgraph of the viscous flow in the magnetic field with electric current through the electrodes (configuration 4)

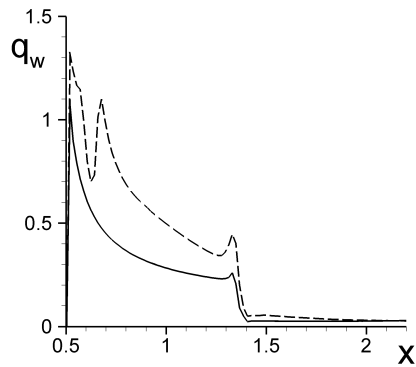


**Fig. 3.18.** Distribution of the body wall heat fluxes due to heavy particles. Solid line corresponds to the flow without MHD interaction; long dashed line corresponds to the flow in the magnetic field with electric current through the electrodes.

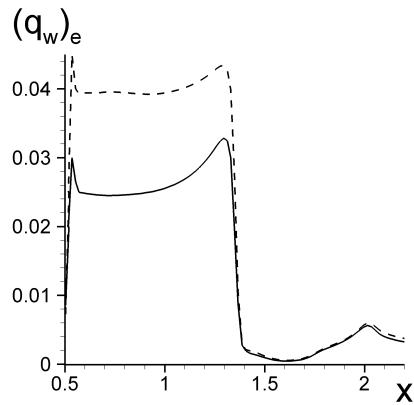


**Fig. 3.19.** Distribution of the body wall heat fluxes due to electrons. Solid line corresponds to the flow without MHD interaction; short dashed line corresponds to the flow in the magnetic field.

### 3.5. Analysis of factors influencing on supersonic flow about “cone-cylinder” body under MHD impact

Continuing investigations of flows about bodies under the MHD interaction (see Technical Report # 16 "Supersonic flow control by a magnetic field" (Section 3)) a study has been done of effect of Joule heat release on a supersonic weakly ionized plasma flow about axisymmetrical body "cone-cylinder" (see Fig. 3.2) under applied magnetic field.

In experimental investigations of such flows to enhance efficiency of the MHD interaction a surface electric discharge was arranged between an electrode installed on the model nose and a ring coaxial electrode installed at cone-cylinder conjugation. In the applied magnetic field the discharge rotates at angular velocity about  $3 \cdot 10^4 \text{ s}^{-1}$ . Nitrogen plasma was considered, the Mach number of the incoming flow was,  $M=4.0$ , the density was,  $\rho=0.039 \text{ kg/m}^3$ , the temperature was,  $T=440 \text{ K}$ , magnetic field and electric discharge parameters were indicated in the previous Section of the present Report.

Effect of the Joule heat release in the rotating discharge was analyzed using the Navier-Stokes equations and a given heat flux on the cone surface.

In this case the equations may be written as follows:

$$\begin{aligned}\frac{\partial \rho}{\partial t} + \text{div}(\rho \vec{V}) &= 0, \\ \rho \frac{d\vec{V}}{dt} &= \text{Div} \vec{P}, \\ \rho \frac{d\left(\varepsilon + \frac{V^2}{2}\right)}{dt} &= \text{div}(\vec{P} \vec{V}) + \text{div}(\lambda \text{grad} T),\end{aligned}$$

here  $\rho$  is the plasma density;  $\vec{V}$  is the plasma velocity;  $T$  is the plasma temperature;  $\mu$ ,  $\lambda$  are the plasma viscosity and the heat conductivity;  $\varepsilon = c_v T = \frac{1}{\gamma - 1} \frac{p}{\rho}$  is the specific internal energy of the

plasma;  $\vec{P} = 2\mu \dot{S} - \left(p + \frac{2}{3}\mu \text{div} \vec{V}\right) \vec{I}$  is the stress tensor;  $\dot{S}$  is the strain velocity tensor;  $E = \frac{3}{2}p + \frac{\rho V^2}{2}$  is the specific total plasma energy.

In the inflow boundary all plasma parameters are prescribed. On the body surface the non-slip conditions are imposed. Heat flux from the cone surface is given on the cone surface to simulate the Joule heat release in the electric discharge. In the outflow boundary the non-reflecting conditions are used.

A computational procedure which is used possesses the second-order accurate in respect to both spatial coordinates in the flow regions with smooth function behavior and the temporal coordinate.

Fig. 3.20 (a) presents a shadowgraph of the supersonic flow about the considered body without MHD interaction. White dots indicate location of the computed bow shock. Thus it is possible to conclude that the Navier-Stokes model provides rather good agreement with experimental data. Fig. 3.20 (b) presents a shadowgraph of the flow under MHD interaction. Estimation of the Joule heat release power at conditions of the experiments gives  $Q \approx 10^5 \text{ W}$ . In computations it was assumed that the heat flux from the cone surface was  $q_w = 6 \cdot 10^7 \text{ W/m}^2$ , which for the body of a given size corresponded to the experimental heat release. Red dots indicate location of the computed bow shock under the heat release on the cone surface.



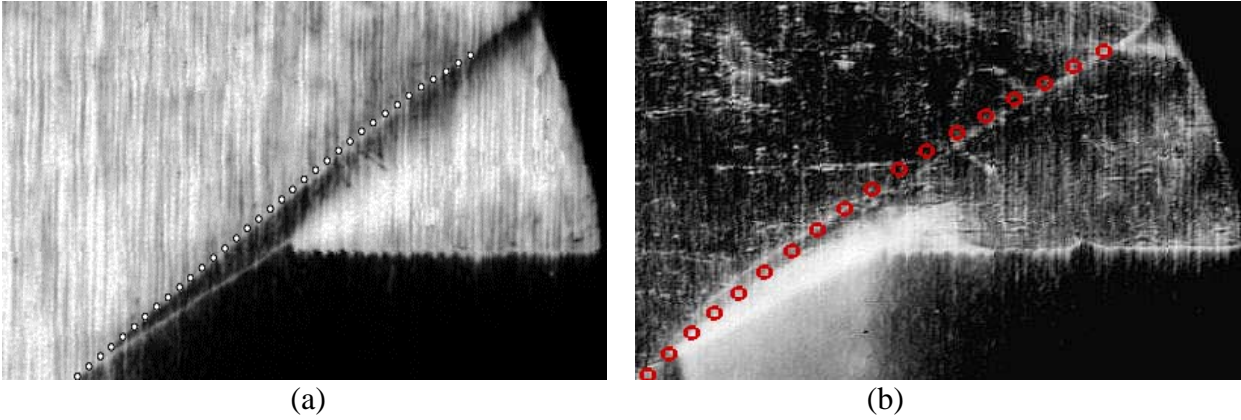


Fig. 3.20. Shadowgraphs of supersonic flows about "cone-cylinder" body: without MHD interaction (left); under MHD interaction (right).

Fig. 3.21 shows shock wave locations from experiments and from computations,  $q_0$  is the heat flux providing for the given body the experimental heat release (all distances are measured in meter). Discrepancy of experimental data and simulations on the cylindrical part of the body (see Fig. 3.20 (left)) may be explained by effect of a specific rarefaction wave on the bow shock since the experimental body has a kink at the cone-cylinder interface which was not considered in the computations. The kink influences on formation of the rarefaction wave which in turn interacting with the bow shock results in its more noticeable bending than in the simulations.

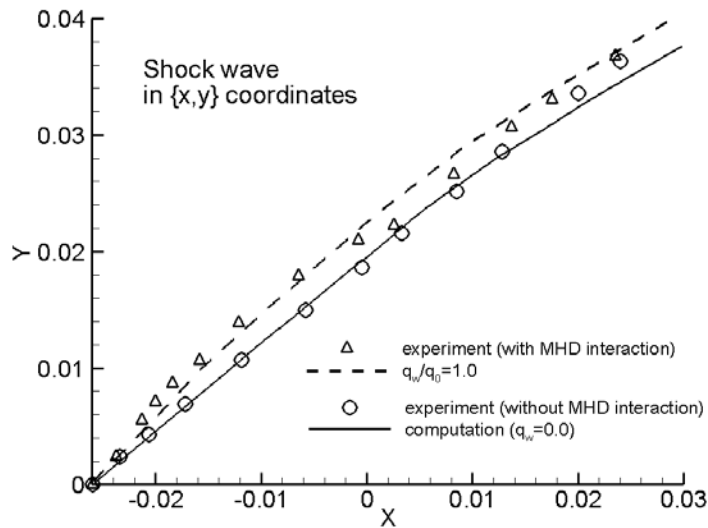


Fig. 3.21. The bow shock in the experiments and in the simulations.

Figs. 3.22 – 3.24 demonstrate distributions of the gas pressure (Fig. 3.22), of the Mach number (Fig. 3.23), and of the gas density (Fig. 3.24). The computations were carried out accounting for the heat flux on the cone surface providing the experimental heat release. It is seen that in the heat release domain rise of the temperature results in subsonic flow behind the attached conical bow shock. The angle of the shock increases (see Fig. 3.21). In the vicinity of the cylindrical part of the body the flow is the transonic one.

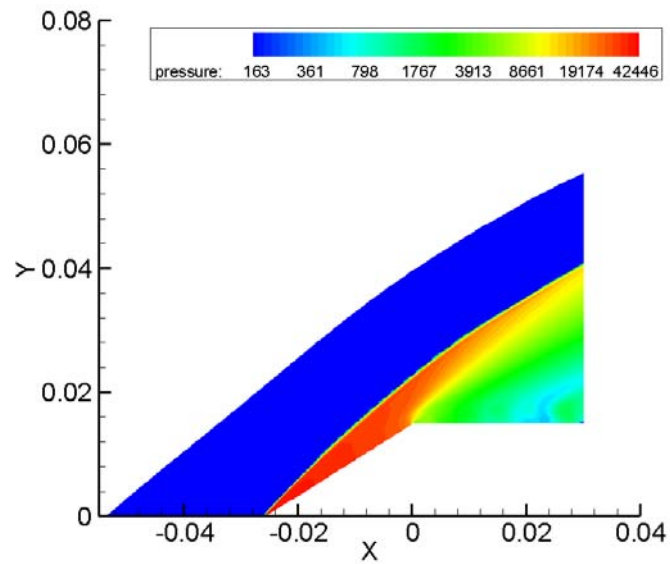


Fig. 3.22. Pressure distribution with the heat flux of the cone surface.

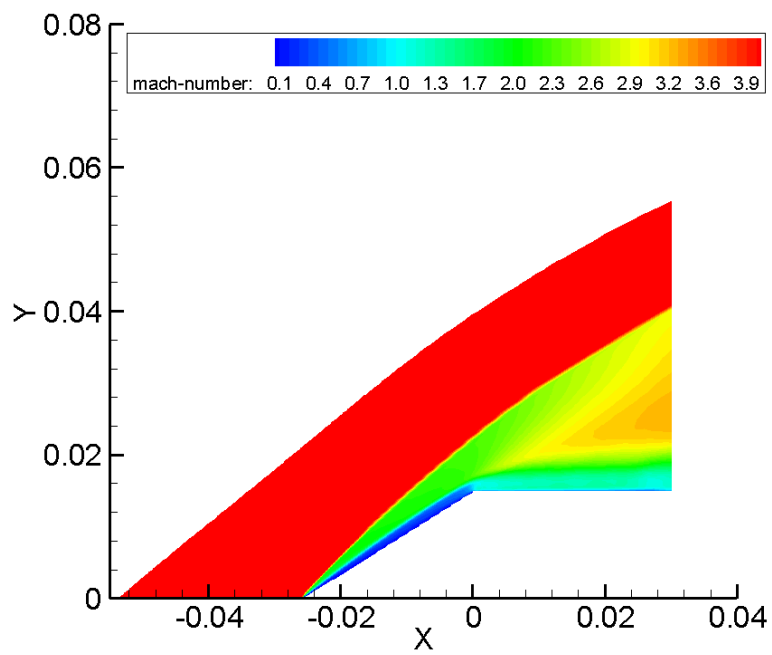


Fig. 3.23. Mach number distribution with the heat flux of the cone surface.

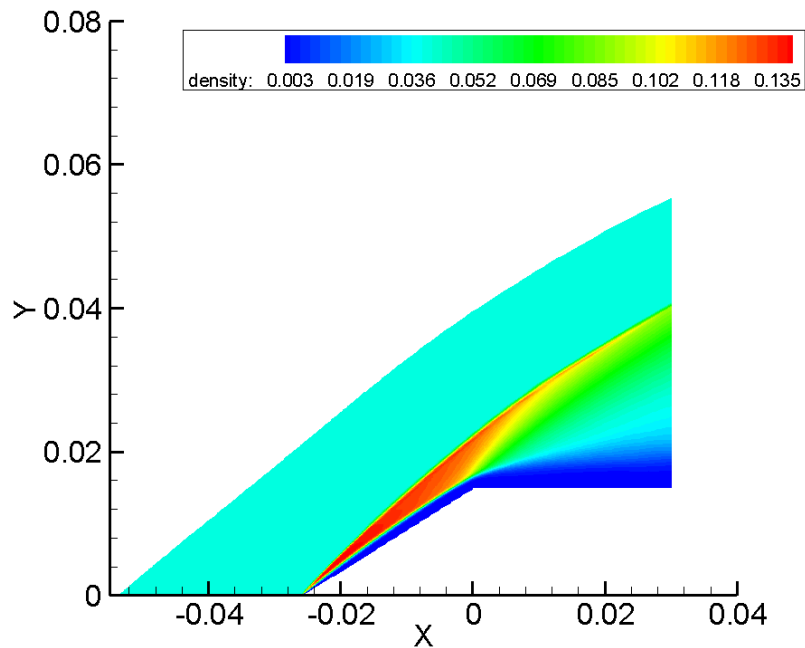


Fig. 3.24. Density distribution with the heat flux of the cone surface.

Increase of the temperature at the cone surface leads to significant decrease of the density and formation of a clearly seen contact surface (see Fig. 3.24).

Thus, on the basis of the obtained results one may conclude that at parameters under study the main factor influencing on the flow structure under MHD interaction is the Joule heat release. Nevertheless it is necessary to note that the accepted model of a perfect gas limits applicability of this approach.

### 3.6. Spatial structure of flow about body accounting for rotation of electric discharge on the body front surface.

To increase locally the electric conductivity of the plasma for the purpose of intensification of the MHD interaction an electric discharge was arranged in the experiments between electrode located in the stagnation point and annular electrode on the body surface in the bluntness-cylinder conjugation. In applied magnetic field generated by the coil in the body (see Fig. 3.6, configuration #1) the electric discharge rotates which results in spatial structure of the flow. As it was shown in Section 3.5 of this Report the main factor influencing on the flow under the considered parameters is the Joule heat release in the discharge. Therefore in simulations of the supersonic flow about the body with rotating electric discharge on the body bluntness the Navier-Stokes equations (see Section 3.5) are used. To take into account the effect of the Joule heat release in the electric discharge a rotating domain with heat flux directed into the flow is used as boundary condition on the body head. The domain has a form of sector on the bluntness with the apex in the stagnation point and the base on the conjugation circumference. The base of the sector is equal to 0.196 radian. The heat flux on the sector surface is equal to that of the electric discharge estimated in this case for parameters under study as  $1.4 \cdot 10^9 \text{ J/s} \cdot \text{m}^2$ .

A supersonic Ar flow about spherically blunted cylinder is considered, radius of bluntness is 0.01 m, incoming flow velocity is 968 m/s, temperature is 300K, pressure is 101350 Pa. The below results correspond to two rotational speeds of “the electric arc” 400 Hz and 2 Hz.

Fig. 3.25 shows the computational domain: the body and three plans in which gasdynamic function distributions will be presented. The first and the second planes are perpendicular to the body

axis and locate at distances 5 mm and 9mm, respectively. The third one passes through the cylinder axis and is chosen to correspond to maximum of the heat release at the given moment of time.

In Figs. 3.26 – 3.28 flow structures for the “arc” rotational speed equal to 400Hz are presented. The figures demonstrate that distributions are significantly asymmetrical and the flow is spatial. It is worth to be mentioned that pressure maximum on the body surface is shifted relatively heat release maximum which is due to finite rate of transport processes in gas. Temperature distribution is presented in Fig. 3.27 a spiral structure of the distribution on the body surface is seen. Origination of the flow vorticity resulted from the “arc” rotation is shown in Fig. 3.28. These figures correspond to time required for about ten full revolutions and the flow is established one.

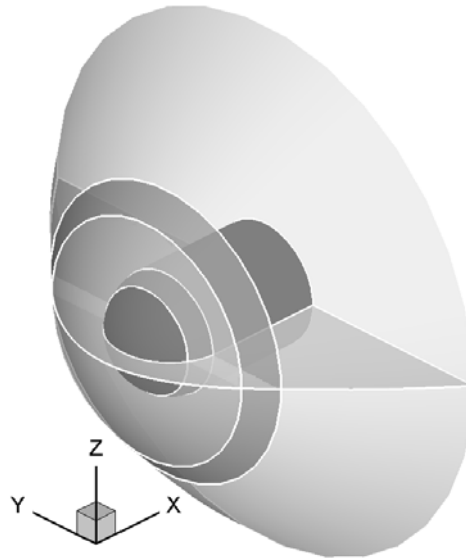


**Fig. 3.25.** Computational domain, the body and three plans in which gasdynamic function distributions will be presented.

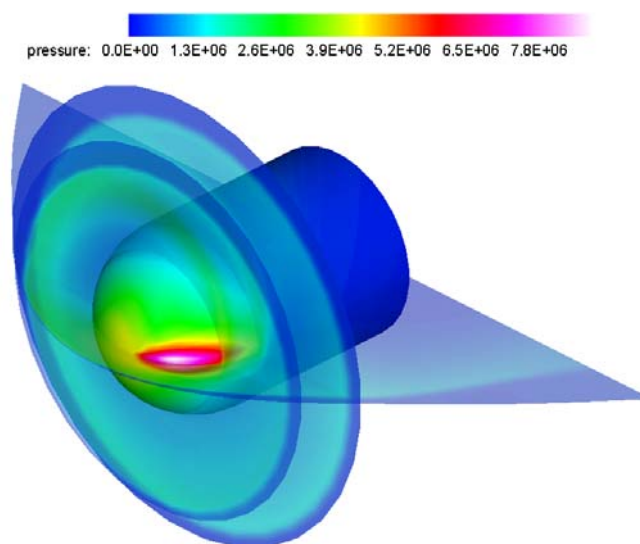


**Fig. 3.26.** Pressure distribution.  $M=3.0$ ;  $p_0=101350$  Pa,  $T=300$  K, Ar, speed of the “arc” rotation is 400 Hz, inflow heat flux is  $1.4 \cdot 10^9 \text{ J/s} \cdot \text{m}^2$

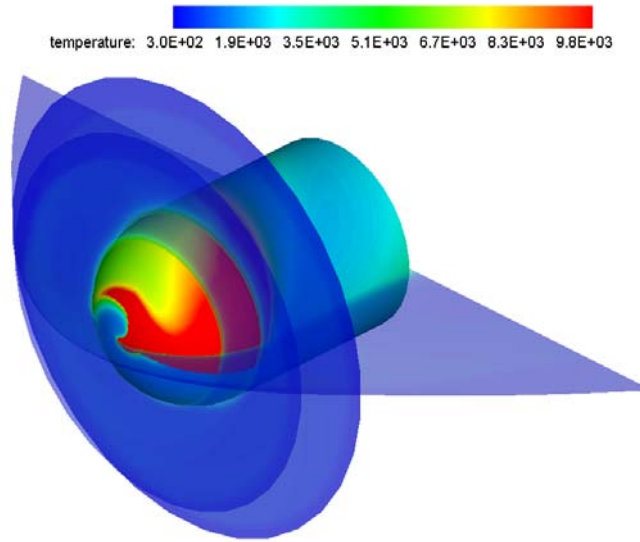


**Fig. 3.27.** Temperature distribution.  $M=3.0$ ;  $p_0=101350$  Pa,  $T=300$  K, Ar, speed of “arc” rotation is 400 Hz, inflow heat flux is  $1.4 \cdot 10^{10} \text{ J/s} \cdot \text{m}^2$

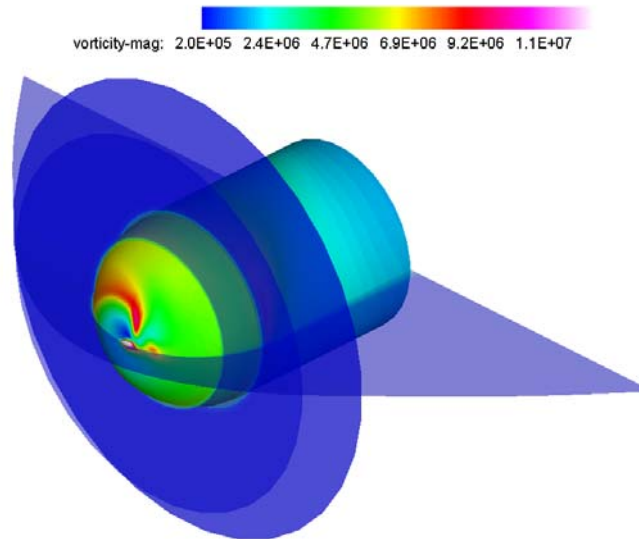


**Fig. 3.28.** Vorticity distribution.  $M=3.0$ ;  $p_0=101350$  Pa,  $T=300$  K, Ar, speed of the “arc” rotation is 400 Hz, inflow heat flux is  $1.4 \cdot 10^9 \text{ J/s} \cdot \text{m}^2$

The following figures present results concerning to the rotation speed 2 Hz. It is seen that due to relatively slow “arc” rotation domains affected by the inflow heat flux essentially larger then in case of 400 Hz. Fig. 3.29 demonstrates that pressure distribution in the horizontal plane is significantly asymmetrical. In Fig. 3.30 temperature distribution is shown which as in the case of higher rotation speed is characterized by steep leading front (the “arc” rotates clockwise) and more stretched back front. This may be explained by the fact that during one revolution even for high speed of rotation the gas heated up in the “arc” is completely replaced by the incoming “cold” gas (which is heated up only in the bow shock wave).

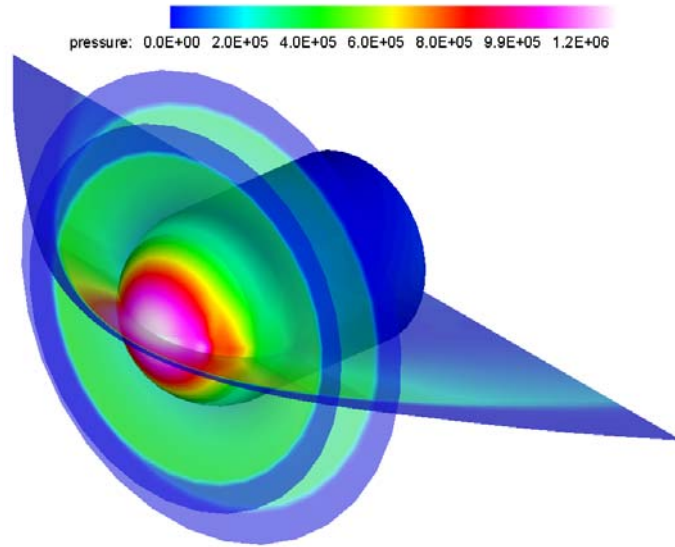


**Fig. 3.29.** Pressure distribution.  $M=3.0$ ;  $p_0=101350$  Pa,  $T=300$  K, Ar, speed of the “arc” rotation is 2 Hz, inflow heat flux is  $1.4 \cdot 10^9 \text{ J/s} \cdot \text{m}^2$

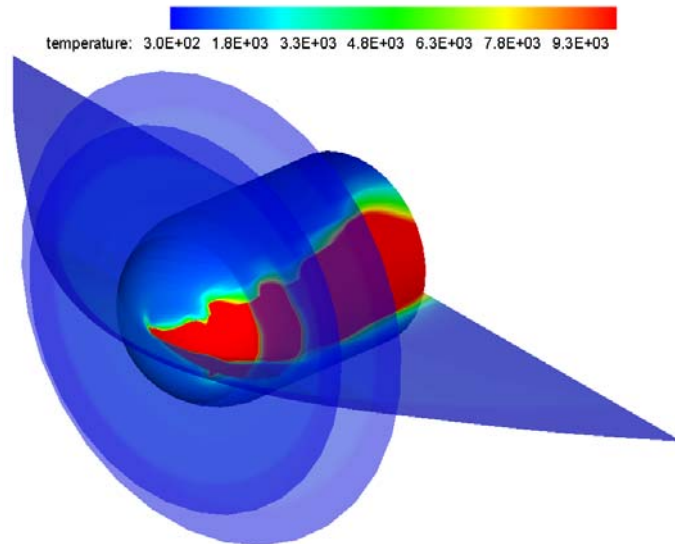


**Fig. 3.30.** Temperature distribution.  $M=3.0$ ;  $p_0=101350$  Pa,  $T=300$  K, Ar, speed of the “arc” rotation is 2 Hz, inflow heat flux is  $1.4 \cdot 10^9 \text{ J/s} \cdot \text{m}^2$

It is seen that in spite of at parameters under study the back front of the heated gas lags behind the moving "arc" the domain of the heated gas is localized.

Distribution of the vorticity in this case is presented in Fig. 3.31. Relatively slow rotation of the energy release domain results in more noticeable disturbances of the flow including vorticity generation.

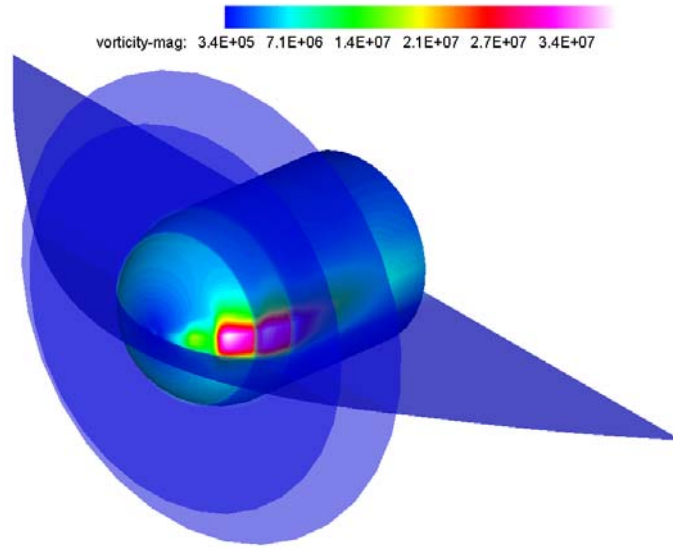


**Fig. 3.31.** Vorticity distribution.  $M=3.0$ ;  $p_0=101350$  Pa,  $T=300$  K, Ar, speed of the “arc” rotation is 2 Hz, inflow heat flux is  $1.4 \cdot 10^9 \text{ J/s} \cdot \text{m}^2$

Time variations of the temperature and pressure in three control points located on circumference on the cylinder surface are presented in Figs. 3.32 – 3.33. The circumference is situated at a distance 1.5 cm from bluntness-cylinder conjugation, the point are shifted from each other on 1.57 radian. Distinction of parameter impulses in these point can be associated with the effect of the “arc” rotation which results in global rearranging of the flow with variation of the bow shock wave shape and location. This in turn leads to variation of gas parameters just behind the shock wave. Since deformation of the shock wave and movement of the heat-release domain are shifted on a phase, parameters of the gas flowing into this domain periodically changes this influences on amplitudes of the temperature and pressure in the control points.

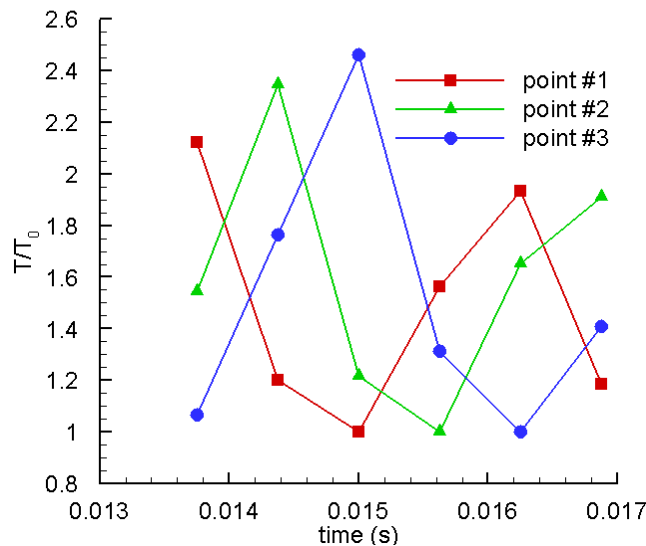


**Fig. 3.32.** Time variation of the temperature in the control points.  $M=3.0$ ;  $p_0=101350$  Pa,  $T=300$  K, Ar, speed of the “arc” rotation is 400 Hz, inflow heat flux is  $1.4 \cdot 10^9 \text{ J/s} \cdot \text{m}^2$

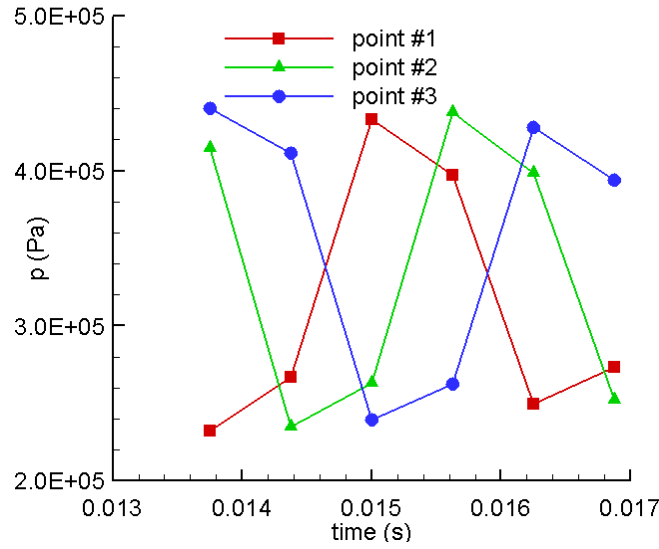


**Fig. 3.33.** Time variation of the pressure in the control points.  
 $M=3.0$ ;  $p_0=101350$  Pa,  $T=300$  K, Ar, speed of the “arc” rotation is 400 Hz,  
inflow heat flux is  $1.4 \cdot 10^9 \text{ J/s} \cdot \text{m}^2$

Deformation of the bow shock wave and its phase lag from the rotational heat-release domain is presented in Fig. 3.34. The figure demonstrates traces of the shock waves on a plane which is perpendicular to the body axis and is situated from the stagnation point on 0.5 cm. Significant shape variation of the wave in time is seen.

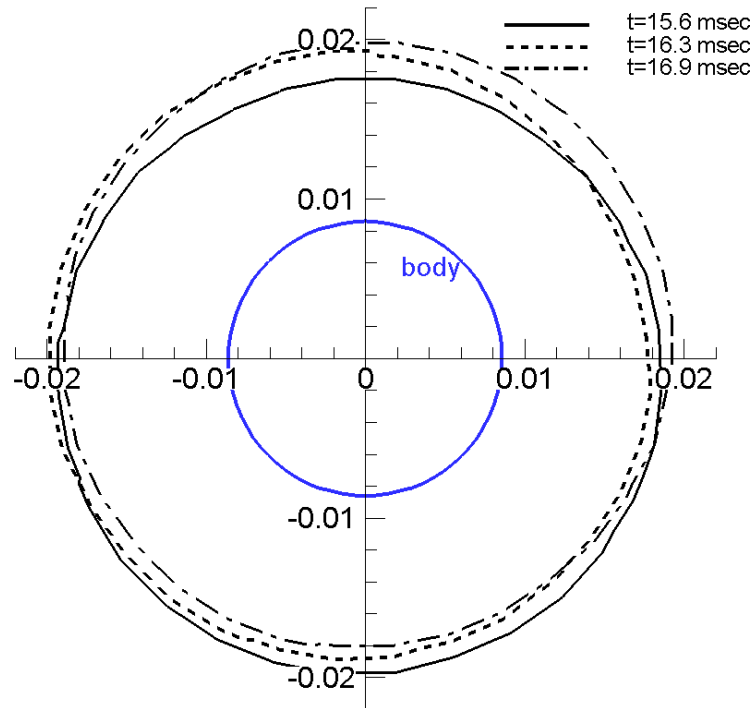


**Fig. 3.34.** Time variation of bow shock wave shape.  
 $M=3.0$ ;  $p_0=101350$  Pa,  $T=300$  K, Ar, speed of the “arc” rotation is 400 Hz,  
inflow heat flux is  $1.4 \cdot 10^9 \text{ J/s} \cdot \text{m}^2$



### 3.7 Conclusions

A set of mathematical models have been developed in course of the investigations in the framework of the Project. This set enables one to describe MHD impact on supersonic flows about bodies and to reveal main factors of this impact. The set includes a model of axisymmetrical MHD flows of non-equilibrium two-temperature three component plasma and a 3-D model of viscous heat-conducting gas. The latter is used for investigation of the effect of the Joule heat release on supersonic flow structure.

The investigations allow to analyze various MHD interaction configuration, effect of incoming flow parameters and plasma composition, and contribution of non-equilibrium processes. A way of local increase of the plasma electric conductivity due to electric discharge on the body head is considered.

It is shown that at parameters under study the Joule heat release is predominant factor influencing on the flow structure. Effect the Joule heat release in case of “arc” rotation on the body head is analyzed and spatial structure of the flow in this case is demonstrated.

### 3.8 References

- [1]. M.Mitchner, C.H.Kruger Jr. Partially Ionized Gases. Willey & Sons, 1973.
- [2]. L.M.Biberman, V.S.Vorobev, I.T.Yakubov // Kinetics of low temperature plasma. M.: Nauka. 1982.
- [3]. Investigations and perspectives of gas ow control by magnetic field. Base Contract Summary Report. January 2000. St.Petersburg, Russia.
- [4]. Yu.M.Volkov et al.// Thermophysics of high temperature, 1966. №. 4. p.136.
- [5]. Supersonic Flow Control by Magnetic Field, The Third Annual Report, ISTC project No.2009p, April 2004.
- [6]. V.A.Bityurin. Doct. thesis., M., 1994.
- [7]. A.V.Rodionov // JCM&MPh., 1989. v. 27, №. 12. p. 1853-1860.
- [8]. S.K.Godunov et al. Chislennoe reshenie mnogomernykh zadach gazovoi dinamiki. M., Nauka, 1976.
- [9]. S.R.Chakravarthy, K.Y.Szema. AIAA Paper 85-1703.
- [10]. Ya.B. Zeldovich, Yu.P.Raizer. Fizika udarnikh voln I vysokotemperaturnye gazodinamicheskie yavleniya. M.: Nauka, 1966.